PDR

EG&G Idaho, Inc.

Report No. IS-NSMD-83-009

Date April 1983

INTERNAL TECHNICAL REPORT

MATERIALS PROPERTIES DATA FOR FUSION REACTOR ANALYSIS

NUCLEAR SAFETY METHODS DIVISION

D. L. Hagrman

Checked By

Approved By

Courtesy release to the public on request. This document was prepared primarily for internal use. Citation or quotation of this document or its contents is inappropriate.

~~THIS DOCUMENT HAS NOT RECEIVED PATENT CLEARANCE AND IS NOT TO BE TRANSMITTED TO THE PUBLIC DOMAIN~~

IS-NSMD-83-009

MATERIALS PROPERTIES DATA FOR FUSION REACTOR ANALYSIS

D. L. Hagrman

Published March 1983

EG&G Idaho, Inc.
Idaho Falls, Idaho 83415

ABSTRACT

This report presents the materials properties that must be considered for fusion reactor safety and design analysis. It also surveys the literature for relevent data on 316 stainless steel, vanadium alloys, ferritic/martensitic steel alloys, graphites, silicon carbide, and G-10 insulation. The report proposes a material properties package design for fusion reactor analysis and provides an example of one section of the proposed materials properties package.

A significant conclusion of the report is that development of the materials properties package should be initiated now at a low level of effort to prevent needless duplication and confusion in fusion reactor analysis computer code development and application projects, some of which are already underway. Additionally, the proposed effort would provide useful information for development of new alloys since it would aid in the identification of those material properties which are most important for fusion reactor performance and safety.

SUMMARY

This report is the result of an Idaho National Engineering Laboratory technical development project[a] to define the materials properties that must be considered for fusion reactor safety and design analysis, and to survey the available literature in order to determine the applicability of existing data. Another major objective was to propose a materials properties package design which provides a site for collection of data and references and establishes a target for knowledgeable criticism of property models.

The project was proposed because experience with a similar project for Light Water Reactor materials properties demonstrated that a separate materials properties package can prevent needless duplication and confusion during development and application of computer codes. As the project was completed, it became obvious that development of a fusion reactors materials property package should already have begun because several computer programs which should be using such a package are under development.

A large number of materials and mary properties have been identified in Table 1 of Section 2. The number is large principally because there is not a complete consensus about the best materials for fusion reactor design. In the remainder of Section 2, the literature is surveyed for relevant data on 316 stainless steel, vanadium alloys, ferritic/martensitic steel alloys, graphites, silicon carbide, and G-10 insulation. These data are discussed and presented in a format that will allow easy use of the data and easy introduction of any additional new data to produce a materials properties package for fusion reactor analysis. The data are presented in both a tabular format for later use in constructing correlations and graphically to display trends for interim use and comprehension. The source of all data

---

a. Project number G3411204G, Fusion Materials Properties, principal investigator D. L. Hagrman, 1983.

is identified and data without original references are ignored unless no other source is available. Section 3 is a discussion of an appropriate design for a materials properties package using the data in Section 2. The proposed design is based on experience with designing and maintaining a similar package for Light Water Reactor Materials Properties. In Appendix A, an example of part of the proposed design is given.

The survey shows that the 316 stainless steel data are relatively complete with the possible exception of hydrogen sputtering yields for low incident ion energies and hydrogen atom recombination rates. The vanadium alloy data base is very limited, with no useable data for hydrogen diffusion, hydrogen ion reflection coefficients, hydrogen atom recombination rates, corrosion in lithium or oxidation in steam or air. Most of the ferritic/martensitic data are not from the most likely alloys, HT-9 and a steel with 9% chromium and 1% molybdenum, but are deduced from similar steels.

The graphite data base is extensive because of the use of this material in high temperature gas reactors. However, serious problems in modeling graphite properties are expected because many of the data that have been reported in the literature are not appropriate for fusion reactor analysis. For example, graphite is anisotropic and large sample-to-sample variations in thermal conductivity and thermal expansion have been attributed to texture variations. Yet pole figures are almost never reported along with the materials property data. Very few data for the effects of irradiation on graphite properties are available. Finally, no data for fracture toughness, hydrogen reflection coefficients, hydrogen atom recombination rates, hydrogen trapping coefficients, or the decay of activated graphite with typical impurities have been found.

The data for silicon carbide are scarce. There is much sample-to-sample scatter in measured thermal conductivities and reported mechanical properties data are nearly non-existent. No data have been found for hydrogen isotope reflection coefficients, trapping coefficients, or hydrogen recombination in silicon carbide.

No data have been found for G-10 insulation specific heat capacity, thermal expansion or emissivity. However, considerable data on G-10 thermal conductivity have been published. These data show that the classical expressions for granular texture variations can be applied to describe the anisotropic thermal conductivity due to differing conductivities of the fiberglass weave and the epoxy which bonds layers of fiberglass. Data from one irradiated sample show a factor of 0.7 reduction in G-10 thermal conductivity with irradiation. The limited data on cyclic failure are not sufficient for modeling cyclic fatigue of the insulation.

The design proposed for a fusion reactor materials properties package consists of a computer library of separate subroutines or functions and detailed model descriptions with a separate appendix for each material and a separate section in every appendix for each property. Both documentation and library subroutines can thus be changed property-by-property as the need arises. Each section would have a summary, a review of literature and data, a description of the model development and a subroutine listing with plots of the output generated from the subroutine.

It is strongly recommended that at least some long-term effort be directed at maintaining a site for the collection of data and a target for knowledgeable criticism of property models. The next logical step is expansion of this report to the several materials mentioned in Section 1 that have not been considered and to include new data from the Task Group on Alloy Development for Irradiation Performance. A parallel effort to produce some materials properties subcodes is likely to yield a significant return in the quality of analysis and in avoiding unnecessary duplication of literature searches by persons employing computer programs. This effort could also provide useful information for the development of new alloys since it would aid in the identification of those properties that are most important for fusion reactor performance and safety.

ACKNOWLEDGEMENTS

The author wishes to thank the Fusion Safety Program for publishing this report, and V. N. Shah for suggesting sources of data on G-10 insulation thermal activity.

CONTENTS

ABSTRACT ii

SUMMARY iii

ACKNOWLEDGEMENTS vi

1. INTRODUCTION 1

2. MATERIALS PROPERTIES DATA REVIEW 3

2.1 316 Stainless Steel 3

2.1.1 Thermal Properties 3
2.1.2 Mechanical Properties 22
2.1.3 Electromagnetic Properties 48
2.1.4 Physical/Chemical Properties 53

2.2 Vanadium Alloys 67

2.2.1 Thermal Properties 71
2.2.2 Mechanical Properties 78
2.2.3 Electromagnetic Properties 82
2.2.4 Physical/Chemical Properties 82

2.3 Ferritic/Martensitic Steel Alloys 85

2.3.1 Thermal Properties 88
2.3.2 Mechanical Properties 96
2.3.3 Electromagnetic Properties 110
2.3.4 Physical/Chemical Properties 110

2.4 Graphite, Pyrolytic Carbon, Vitreous Carbon, and Fibrous Graphite 113

2.4.1 Thermal Properties 116
2.4.2 Mechanical Properties 131
2.4.3 Electromagnetic Properties 141
2.4.4 Physical/Chemical Properties 141

2.5 Silicon Carbide 148

2.5.1 Thermal Properties 148
2.5.2 Mechanical Properties 156
2.5.3 Electromagnetic Properties 156
2.5.4 Physical/Chemical Properties 159

2.6 G-10 Insulation 160

    2.6.1 Thermal Properties 169
    2.6.2 Mechanical Properties 169
    2.6.3 Electromagnetic Properties 178

3. MATERIALS PROPERTIES PACKAGE DESIGN 179

4. REFERENCES 181

APPENDIX A--EXAMPLE MATERIAL PROPERTY COMPUTER SUBCODE. HYDROGEN ISOTOPES DIFFUSION COEFFICIENTS IN 316 STAINLESS STEEL (SDIF) 190

A.1 Summary 191

A.2 Literature and Data 192

A.3 Model Development 198

A.4 SDIF Subroutine Listing and Plots 201

A.5 References 204

FIGURES

1. Specific heat capacity of 316 stainless steel given by Peckner and Bernstein[1] and by Leibowitz et al.[7] 16

2. Thermal conductivity of 316 stainless steel given by Peckner and Bernstein[1] and by Leibowitz et al.[7] 18

3. Thermal expansion coefficient of 316 stainless steel given by Peckner and Bernstein[1] and by Leibowitz et al.[7] 20

4. Thermal strain of 316 stainless steel referenced to 89.9 K obtained by integrating thermal expansion coefficients given by Peckner and Bernstein[1] and by Leibowitz et al.[7] 21

5. Data and values recommended for 316 stainless steel yield strength 29

6. Data and values recommended for 316 stainless steel ultimate strength 30

7. Data for 316 stainless steel uniform elongation 31

8. 316 stainless steel creep rates and rupture times recommended by Peckner and Bernstein[1] 40

9. True failure stress as a function of neutron fluence, cold-work, and temperature reported by Bloom and Wiffen[11] 41

10. Comparison of 316 stainless steel crack growth rate data from Michel and Smith[22] with a one minute hold time to crack growth predictions from Reference 6 49

11. Reflection coefficients for hydrogen isotopes incident on stainless steel 58

12. Trapping coefficients for deuterium ions incident on stainless steel 60

13. Recombination rate coefficients for hydrogen isotopes on stainless steel 64

14. Radioactivity of 316 stainless steel after shutdown according to Crocker and Holland[55] 70

15. Specific heat values recommended for vanadium by Touloukian and Ho[56] 74

16. Values of thermal strain of vanadium recommended by Touloukian and Ho[56] 77

17. Values for crack growth rate in vanadium at room temperature recommended by Bloom[12] 83

18. Radioactivity of vanadium-titanium alloys according to Crocker and Holland[55] 87

19. Specific heat capacity of 410 stainless steel given by Peckner and Bernstein[1] 90

20. Thermal conductivity of 403 and 410 stainless steel according to Peckner and Bernstein[1] 92

21. Average thermal expansion coefficients for 403 and 410 stainless steel between 273.15 K and the indicated temperature according to Peckner and Bernstein[1] 95

22. Thermal strains of 403 and 410 stainless steel referenced to 273.15 K obtained from the average thermal expansion coefficients given by Peckner and Bernstein[1] 99

23. Young's modulus of 410 stainless steel according to Peckner and Bernstein[1] 101

24. Yield strength of HT-9 steel, annealed 410 stainless steel, and heat treated 410 stainless steel according to Rawls et al.[64] and Peckner and Bernstein[1] 105

25. Ultimate strength of HT-9 steel, annealed 410 stainless steel, and heat treated 410 stainless steel according to Rawls et al.[64] and Peckner and Bernstein[1] 106

26. Resistivity of 410 stainless steel reported by Peckner and Bernstein[1] 111

27. Radioactivity of HT-9 steel after shutdown according to Rawls et al.[64] 115

28. Thermal conductivity of several graphites as a function of temperature 123

29. Thermal strains for several graphites 132

30. Silicon carbide specific heat capacity values recommended by Goldsmith et al.[89] 149

31. Silicon carbide thermal strains with a reference temperature of 298 K 155

32. Resistivity of a silicon carbide sample according to Chiochetti and Henry[100] 158

33. Hydrogen diffusion coefficients in silicon carbide measured by Verghese et al.[101] 162

34. Hydrogen solubility in silicon carbide measured by Verghese Verghese et al.[101] 164

35. Radioactivity of silicon carbide after shutdown according to Crocker and Holland[55] 167

36. G-10 thermal conductivities measured by Hust[105] 172

37. Compressive strength of G-10 insulation 177

A-1. Hydrogen isotope diffusion coefficient data normalized to one atomic weight unit 199

A-2. Values of the hydrogen (top line), deuterium (middle line), and tritium (bottom line) diffusion coefficients in 316 stainless steel calculated by the SDIF subroutine as a function of reciprocal temperature 203

TABLES

1. Materials properties for Fusion reactor analysis 4

2. Specific heat capacities of 316 stainless steel from curves of Peckner and Bernstein[1] and Leibowitz et al.[7] 17

3. Thermal conductivities of 316 stainless steel from curves of Peckner and Bernstein[1] and Leibowitz et al.[7] 19

4. Thermal strains of 316 stainless steel calculated by integrating curves of Peckner and Bernstein[1] and Leibowitz et al.[7] 23

5. 316 stainless steel elastic moduli according to Peckner and Bernstein[1] 24

6. 316 stainless steel plastic deformation data from Grossbeck and Maziasz[15] 26

7. 316 stainless steel plastic deformation data from Jones et al.[14] 27

8. 316 stainless steel plastic deformation data from Fenici et al.[13] 27

9. 316 stainless steel plastic deformation data from Bloom and Wiffen[11] 28

10. 316 stainless steel creep data from Bloom and Wiffen[11] 36

11. 316 stainless steel creep data from Sikka and David[17] 37

12. 316 stainless steel creep data from Lovel and Barker[18] 38

13. 316 stainless steel true failure stress data from Bloom and Wiffen[11] 39

14. 316 stainless steel fatigue crack growth rates according to Michel and Smith[22] 46

15. Fracture toughness of 316 stainless steel welds according to Fickett et al.[29] 50

16. Slope and intercept for Stanley's[30] linear correlation between magnetization and applied field 52

17. Hydrogen-on-stainless steel reflection coefficients according to Eckstein et al.[41] 57

18. Hydrogen-on-stainless steel reflection coefficients according to Thomas[42] 57

19. Trapping coefficient for deuterium ions on a stainless steel surface from Freeman et al.[43] 59

20. Deuterium recombination rates on stainless steel according to Braun et al.[44] 62

21. Hydrogen isotope recombination rates reported by Wilson[39] 63

22. Mass loss of 316 stainless steel in flowing lithium according to Whitlow et al.[52] 66

23. Mass loss of 316 stainless steel in flowing lithium according to Tortorelli and DeVan[53] 66

24. Radioactivity of 316 stainless steel after shutdown according to Crocker and Holland[55] 68

25. Specific heat values recommended for vanadium by Touloukian and Ho[56] 72

26. Thermal conductivities recommended for vanadium by Touloukian and Ho[56] 75

27. VANSTAR 7 plastic deformation data from Korth and Schmunk[58] 80

28. V-20Ti plastic deformation data from Tanaka et al.[59] 81

29. Radioactivity of vanadium-titanium alloy after shutdown according to Crocker and Holland[55] 86

30. Specific heat capacities of 410 stainless steel from curve of Peckner and Bernstein[1] 89

31. Thermal conductivities of 403 and 410 stainless steel from curves of Peckner and Bernstein[1] 91

32. Average thermal expansion coefficients for 403 and 410 stainless steel from curves published by Peckner and Bernstein[1] 93

33. Thermal strains calculated from average thermal expansion coefficient curves of Peckner and Bernstein[1] 97

34. 410 stainless steel elastic modulus according to Peckner and Bernstein[1] 100

35. HT-9 plastic deformation data from Rawls et al.[64] 103

36. 410 Stainless steel plastic deformation properties from Peckner and Bernstein[1] 104

37. HT-9 steel creep data from Paxton et al.[65] 107

38. 403 and 410 stainless steel creep data from Peckner and Bernstein[1] 108

39. Electrical Resistivity of 410 stainless steel from curve of Peckner and Bernstein[1] 112

40. Radioactivity of HT-9 steel after shutdown according to Rawls et al.[64] 114

41. Specific Heat Capacity and Enthalpy at constant pressure recommended by Nightingale et al.[69] 117

42. Thermal conductivity of some graphites measured by Engle and Beavan[70] 118

43. Thermal conductivity of some graphites reported at the Bournemouth symposium[71] 119

44. Thermal conductivity of SM2-24 graphite according to Matsuo[72]..... 120

45. Thermal conductivity of graphite reported by Francl and Kingery[74] 121

46. Linear thermal expansion strains of graphite reported by Fulkerson[75] 124

47. Linear thermal expansion strains of graphites reported by Engle and Beavan[70] 129

48. Linear thermal expansion strains of graphites reported at the Bournemouth symposium[71] 130

49. Young's modulus of graphite reported at the Bournemouth symposium[71] 134

50. Young's modulus of graphites measured by Engle and Beavan[70] 135

51. Electrical resistivity of several graphites 142

52. Permeabilities of several graphites according to Jackson[69] 146

53. Graphite sputtering yield measurements 147

54. Specific heat curve for SiC recommended by Goldsmith et al.[89]..... 150

55. Silicon carbide thermal conductivity measurements 152

56. Silicon carbide thermal expansion measurements 154

57. Silicon carbide resistivity measured by Chiochetti and Henry[100] 157

58. Diffusion coefficients for hydrogen in silicon carbide according to Verghese et al.[101] 161

59. Solubility of hydrogen in silicon carbide according to Verghese et al.[101] 163

60. Sputtering yields from silicon carbide surfaces 165

61. Radioactivity of silicon carbide after shutdown according to Crocker and Holland[55] 168

62. Thermal conductivity of G-10 insulation samples according to Hust[105] 170

63. Elastic moduli of G-10 insulation samples according to Schramm and Kasen[106] 173

64. Elastic moduli of G-10 insulation samples according to Ledbetter[107] 174

65. G-10 plastic deformation data from Schramm and Kasen[106] 176

A-1. Deuterium diffusion coefficients measured in 304 stainless steel by Braun et al.[A-7] 197

A-2. Listing of the SDIF subroutine 202

MATERIALS PROPERTIES DATA FOR FUSION REACTOR ANALYSIS

1. INTRODUCTION

One of the longer lead-time items required for the design and safety analysis of fusion reactors is a complete and assessed collection of materials properties data and models. Not only do the nominal property values have to be known, but the uncertainty must be assessed in order to determine which nominal values need improvement.

This report is the result of an Idaho National Engineering Laboratory technical development project[a] to define the materials properties that must be considered for fusion reactor safety and design analysis, and to survey the available literature in order to determine the applicability of existing data. The report was published with Fusion Safety Research funds.

In order to show how data would eventually be presented for use, a materials properties package design is proposed. The design is consistent with the longer-range objectives of providing a site for collection of referenced data and of establishing a target for knowledgeable criticism of property models. The package is also structured to aid both quick calculations and the detailed computer analysis that will follow.

Many of the data which have been collected and reviewed will not be applicable to the materials that are finally used in fusion reactor structures because the current materials are very likely to be modified before they are used in fusion reactors. The data are still useful because they represent the best current estimate of the materials properties and can help guide the development of new materials by the Office of Fusion Energy Materials Program if they are used systematically in analysis of fusion

---

[a] Project number G3411204G, Fusion Materials Properties, principal investigator D. L. Hagrman, 1983.

reactor behavior. If they are not used systematically, it is very likely the development of new alloys will receive a confused response from analysis programs because of the varying materials descriptions used in different analyses.

The list of materials and properties identified for study in Table 1 of Section 2 turned out to be so long that there were not sufficient funds to complete a survey for all the materials. Only six materials from the list are reviewed in the rest of the section. Expansion of the survey to the remaining materials is recommended for a later project. Section 3 is a disucssion of an appropriate design for a materials package using the data in Section 2. An example is given in Appendix A.

2. MATERIALS PROPERTIES DATA REVIEW

Table 1 is a list of the materials and properties identified as appropriate for fusion reactor behavior analysis. 316 stainless steel, titanium alloys, vanadium alloys, and ferritic/martensitic steels are included because they are under consideration for first wall materials. Graphite and silicon carbide are candidate materials for limiters and armor. Copper alloys, Nb_3Sn, NbTi, G-10 insulation, and helium are magnet components, while the remaining materials are candidate blanket materials. The table was constructed from several private discussions and communications and includes as many entries as the author could identify as useful. A few of the entries are actually not materials properties but are included to prevent them from being ignored.

Budget limitations prevented a complete survey of all the properties of Table 1 so the materials most likely to be studied in early analysis were selected for review--316 stainless steel, vanadium alloys, ferritic/martensitic steels, graphite, silicon carbide, and G-10 insulation. Addition of the remaining materials properties will be proposed for later projects.

2.1 316 Stainless Steel

Several handbooks and summaries of stainless steel properties have been published.[1-9] The principal limitation of these general collections of data is that they usually do not include the effects of high energy neutron irradiation from the plasma. Since this irradiation causes helium production from nickel and other alloy atoms in the steel, many of the mechanical properties significantly during irradiation. Reference 8 discusses some of these effects. An additional limitation is that some alloy modification is likely to occur during the design of full-scale fusion reactors.

2.1.1. Thermal Properties

The thermal properties of electronic conductors like 316 stainless steel above room temperatuare are not likely to be seriously affected by

TABLE 1. MATERIALS PROPERTIES FOR FUSION REACTOR BEHAVIOR ANALYSIS

TYPE 316 STAINLESS STEEL

- Thermal Properties
  - Specific Heat Capacity, Enthalpy
  - Thermal Conductivity
  - Thermal Expansion
  - Emissivity
  - Heats of Fusion, Vaporization
- Mechanical Properties
  - Elastic Moduli
  - Plastic Moduli and Creep
  - Failure Stresses
  - Cyclic Fatigue Description (Crack Growth Rates)
  - Irradiation-Induced Growth and Swelling
  - Fracture Toughness
- Electro-Magnetic Properties
  - Magnetic Permeability
  - Electrical Resistivity
- Physical/Chemical Properties
  - Density
  - Melting Temperatures
  - Hydrogen Isotopes Permeability
  - Hydrogen Isotopes Diffusion Rates
  - Hydrogen Isotopes Solubility
  - Hydrogen Isotopes Reflection Coefficients
  - Hydrogen Isotopes Trapping Coefficients
  - Hydrogen Isotopes Molecular Recombination Rates
  - Hydrogen Isotopes Sputtering Yields
  - Corrosion Rate by Lithium and Lithium-Lead Compounds
  - Corrosion Rate by Water
  - Activation Products Decay Times

TITANIUM ALLOYS

- Thermal Properties
  - Specific heat Capacity, Enthalpy
  - Thermal Conductivity
  - Thermal Expansion
  - Emissivity
  - Heats of Fusion, Vaporization

TABLE 1. (continued)

TITANIUM ALLOYS (continued)

- Mechanical Properties
  - Elastic Moduli
  - Plastic Moduli and Creep
  - Failure Stresses
  - Cyclic Fatigue Description (Crack Growth Rates)
  - Irradiation-Induced Growth and Swelling
  - Fracture Toughness
- Electro-Magnetic Properties
  - Magnetic Permeability
  - Electrical Resistivity
- Physical/Chemical Properties
  - Density
  - Melting Temperatures
  - Phase Transition Temperatures
  - Hydrogen Isotopes Permeability
  - Hydrogen Isotopes Diffusion Rates
  - Hydrogen Isotopes Solubility
  - Hydrogen Isotopes Reflection Coefficients
  - Hydrogen Isotopes Trapping Coefficients
  - Hydrogen Isotopes Molecular Recombination Rates
  - Hydrogen Isotopes Sputtering Yields
  - Corrosion Rate by Lithium
  - Corrosion Rate by Water
  - Activation Products Decay Times

VANADIUM ALLOYS

- Thermal Properties
  - Specific Capacity, Enthalpy
  - Thermal Conductivity
  - Thermal Expansion
  - Emissivity
  - Heats of Fusion, Vaporization
- Mechanical Properties
  - Elastic Moduli
  - Plastic Moduli and Creep
  - Failure Stresses

TABLE 1. (continued)

VANADIUM ALLOYS (continued)

- Mechanical Properties (continued)
    - Cyclic Fatigue Description (Crack Growth Rates)
    - Irradiation-Induced Growth and Swelling
    - Fracture Toughness
- Electro-Magnetic Properties
    - Magnetic Permeability
    - Electrical Resistivity
- Physical/Chemical Properties
    - Density
    - Melting Temperatures
    - Hydrogen Isotopes Permeability
    - Hydrogen Isotopes Diffusion Rates
    - Hydrogen Isotopes Solubility
    - Hydrogen Isotopes Reflection Coefficients
    - Hydrogen Isotopes Trapping Coefficients
    - Hydrogen Isotopes Molecular Recombination Rates
    - Hydrogen Isotopes Sputtering Yields
    - Corrosion Rate by Lithium
    - Corrosion Rate by Water
    - Activation Products Decay Times

FERRITIC/MARTENSITIC STEELS

- Thermal Properties
    - Specific Heat Capacity, Enthalpy
    - Thermal Conductivity
    - Thermal Expansion
    - Emissivity
    - Heats of Fusion, Vaporization
- Mechanical Properties
    - Elastic Moduli
    - Plastic Moduli and Creep
    - Failure Stresses
    - Cyclic Fatigue Description Crack Growth Rates)
    - Irradiation-Induced Growth and Swelling
    - Fracture Toughness

TABLE 1. (continued)

FERRITIC/MARTENSITIC STEELS (continued)

- Electro-Magnetic Properties
  - Magnetic Permeability
  - Electrical Resistivity
- Physical/Chemical Properties
  - Density
  - Melting Temperatures
  - Hydrogen Isotopes Permeability
  - Hydrogen Isotopes Diffusion Rates
  - Hydrogen isotopes Solubility
  - Hydrogen Isotopes Reflection Coefficients
  - Hydrogen Isotopes Trapping Coefficients
  - Hydrogen Isotopes Molecular Recombination Rates
  - Hydrogen Isotopes Sputtering Yields
  - Corrosion Rate by Lithium
  - Corrosion Rate by Water
  - Activation Products Decay Times

GRAPHITE

- Thermal Properties
  - Specific Heat Capacity, Enthalpy
  - Thermal Conductivity
  - Thermal Expansion
  - Emissivity
  - Heat of Sublimation
- Mechanical Properties
  - Elastic Moduli
  - Plastic Moduli and Creep
  - Failure Stresses
  - Cyclic Fatigue Description (Crack Growth Rates)
  - Irradiation-Induced Growth and Swelling
  - Fracture Toughness
- Electro-Magnetic Properties
  - Magnetic Permeability
  - Electrical Resistivity

TABLE 1. (continued)

GRAPHITE (continued)

- Physical/Chemical Properties
  - Density
  - Hydrogen Isotopes Permeability
  - Hydrogen Isotopes Diffusion Rates
  - Hydrogen Isotopes Solubility
  - Hydrogen Isotopes Reflection Coefficients
  - Hydrogen Isotopes Trapping Coefficients
  - Hydrogen Isotopes Sputtering Yields
  - Oxidation Rates
  - Activation Products Decay Times

SILICON CARBIDE

- Thermal Properties
  - Specific Heat Capacity, Enthalpy
  - Thermal Conductivity
  - Thermal Expansion
  - Emissivity
- Mechanical Properties
  - Elastic Moduli
  - Plastic Moduli and Creep
  - Failure Stresses
  - Cyclic Fatigue Description (Crack Growth Rates)
  - Irradiation-Induced Growth and Swelling
  - Fracture Toughness
- Electro-Magnetic Properties
  - Magnetic Permeability
  - Electrical Resistivity
- Physical/Chemical Properties
  - Decomposition Temperature
  - Density
  - Hydrogen Isotopes Permeability
  - Hydrogen Isotopes Diffusion Rates
  - Hydrogen Isotopes Solubility
  - Hydrogen Isotopes Reflection Coefficients
  - Hydrogen Isotopes Sputtering Yields
  - Activation Products Decay Times

TABLE 1. (continued)

COPPER AND COPPER ALLOYS

- Thermal Properties
  - Specific Heat Capacity, Enthalpy
  - Thermal Conductivity
  - Thermal Expansion
  - Emissivity
  - Heats of Fusion, Vaporization
- Mechanical Properties
  - Elastic Moduli
  - Plastic Moduli and Creep
  - Failure Stresses
  - Cyclic Fatigue Description (Crack Growth Rates)
  - Irradiation-Induced Growth and Swelling
- Electro-Magnetic Properties
  - Magnetic Permeability
  - Electrical Resistivity
- Physical/Chemical Properties
  - Melting Temperature
  - Activation Products Decay Times

Nb_3Sn

- Thermal Properties
  - Specific Heat Capacity, Enthalpy
  - Thermal Conductivity
  - Thermal Expansion
  - Emissivity
  - Heats of Fusion, Vaporization
- Mechanical Properties
  - Elastic Moduli
  - Plastic Moduli and Creep
  - Failure Stress
  - Cycle Fatigue Description (Crack Growth Rates)
  - Irradiation-Induced Growth and Swelling

TABLE 1. (continued)

Nb_3Sn (continued)

- Electro-Magnetic Properties
  - Magnetic Permeability
  - Electrical Resistivity
  - Critical Field/Critical Current/Critical Temperature
- Physical/Chemical Properties
  - Melting Temperature
  - Activation Products Decay Times

NbTi

- Thermal Properties
  - Specific Heat Capacity, Enthalpy
  - Thermal Conductivity
  - Thermal Expansion
  - Emissivity
  - Heats of Fusion, Vaporization
- Mechanical Properties
  - Elastic Moduli
  - Plastic Moduli and Creep
  - Failure Stress
  - Cycle Fatigue Description (Crack Growth Rates)
  - Irradiation-Induced Growth and Swelling
- Electro-Magnetic Properties
  - Magnetic Permeability
  - Electrical Resistivity
  - Critical Field/Critical Current/Critical Temperature
- Physical/Chemical Properties
  - Melting Temperature
  - Activation Products Decay Times

G-10 INSULATION

- Thermal Properties
  - Specific Heat Capacity, Enthalpy
  - Thermal Conductivity
  - Thermal Expansion
  - Emissivity
  - Heats of Fusion, Vaporization

TABLE 1. (continued)

G-10 INSULATION (continued)

- Mechanical Properties
  - Elastic Moduli
  - Plastic Moduli and Creep
  - Failure Stresses
  - Cyclic Fatigue Description (Crack Growth Rates)
  - Irradiation-Induced Growth and Swelling
- Electro-Magnetic Properties
  - Magnetic Permeability
  - Electrical Resistivity
  - Electric Breakdown Field
- Physical/Chemical Properties
  - Melting Temperature
  - Activation Products Decay Times

LITHIUM

- Thermal Properties
  - Specific Heat Capacity, Enthalpy
  - Thermal Conductivity
  - Thermal Expansion
  - Emissivity
  - Heats of Fusion, Vaporization
- Mechanical Properties
  - Bulk Modulus
  - Viscosity
- Electro-Magnetic Properties
  - Magnetic Permeability
  - Electrical Resistivity
- Physical/Chemical Properties
  - Melting Temperature
  - Hydrogen Isotope Solubility
  - Reaction Rate With Water, Energy Release
  - Reaction Rate With Concrete, Energy Release
  - Activation Products Decay Times

TABLE 1. (continued)

- $LiAlO_2$
  - Thermal Properties
    - Specific Heat Capacity, Enthalpy
    - Thermal Conductivity
    - Thermal Expansion
    - Emissivity
    - Heats of Fusion, Vaporization
  - Mechanical Properties
    - Elastic Moduli
    - Plastic Moduli and Creep
    - Failure Stresses
    - Irradiation-Induced Growth and Swelling
  - Electro-Magnetic Properties
    - Magnetic Permeability
    - Electrical Resistivity
  - Physical/Chemical Properties
    - Melting Temperature
    - Hydrogen Isotope Diffusion Rates
    - Activation Products Decay Times
    - Reaction Rate with Water, Energy Release
- LITHIUM-LEAD COMPOUNDS
  - Thermal Properties
    - Specific Heat Capacity, Enthalpy
    - Thermal Conductivity
    - Thermal Expansion
    - Emissivity
    - Heats of Fusion, Vaporization
  - Mechanical Properties
    - Bulk Modulus
    - Viscosity
  - Electro-Magnetic Properties
    - Magnetic Permeability
    - Electrical Resistivity

TABLE 1. (continued)

LITHIUM-LEAD COMPOUNDS (continued)

- Physical/Chemical Properties
  - Melting Temperature
  - Hydrogen Isotope Solubility
  - Reaction Rate With Water, Energy Release
  - Reaction Rate With Concrete, Energy Release
  - Activation Products Decay Times

HELIUM

- Thermal Properties
  - Specific Heat Capacity, Enthalpy
  - Thermal Conductivity
  - Thermal Expansion
  - Emissivity
  - Heat of Vaporization
- Mechanical Properties
  - Bulk Modulus
  - Viscosity
- Electro-Magnetic Properties
  - Magnetic Permeabilities
  - Electrical Resistivities
  - Dielectric Constant
- Physical/Chemical Properties
  - Density
  - Vapor Pressure Versus Temperature
  - Phase Transition Temperature

HYDROGEN ISOTOPES

- Thermal Properties
  - Specific Heat Capacity, Enthalpy
  - Thermal Conductivity
  - Thermal Expansion
  - Emissivity
  - Heat of Vaporization
- Mechanical Properties
  - Bulk Modulus
  - Viscosity

TABLE 1. (continued)

HYDROGEN ISOTOPES (continued)

Electro-Magnetic Properties

- Magnetic Permeabilities
- Electrical Resistivities
- Dielectric Constant

Physical/Chemical Properties

- Density
- Vapor Pressure Versus Temperature
- Ortha/para conversion rate for hydrogen

---

neutron irradiation. It is therefore likely that the data summaries of Reference 1 which are the most complete of the several references will be adequate for fusion analysis for the next several years.

Figure 1 is a reproduction of the specific heat capacities of 316 stainless steel given by Peckner and Bernstein[1] and by Leibowitz et al.[7,a] The only differences in the specific heats reported by these sources occur at the temperature extremes and even there the differences are less than 10%. Values of specific heat taken from the curves presented by these references are displayed in Table 2.

Thermal conductivities reported by Peckner and Bernstein and by Leibowitz et al. are reproduced in Figure 2. Although both sources show a linear dependence on temperature, the slope and values of the line from Leibowitz et al. is about 10% higher than the slope and values from Peckner and Bernstein. Table 3 shows values taken from the curves presented by these two references. The amount of cold-work of these samples is not known.

Peckner and Bernstein and Leibowitz et al. are also the sources for the thermal expansion coefficient plots shown in Figure 3. The difference between the values reported by these references is significant, more than 10%. Unfortunately, Reference 1 does not discuss the measurements on which it's curve is based (other than to list references which were not available to this author). Reference 7 indicates that its curve is based on density measurements. It is possible that the difference in the data is due to some unspecified parameter like cold work or grain size.

In order to convert the thermal expansion coefficient data into a form more useful for analysis, the values shown in Figure 3 were integrated and the resultant thermal strains plotted with a reference temperature of 89.9 K (the lowest datum of Reference 1) in Figure 4. The integration of the data of Reference 1 was performed by digitizing the curve given in this reference

---

[a] 5.63375×10^{-2} kg/gm-mole was used to convert the Leibowitz data from J/cal K to J/kg K.

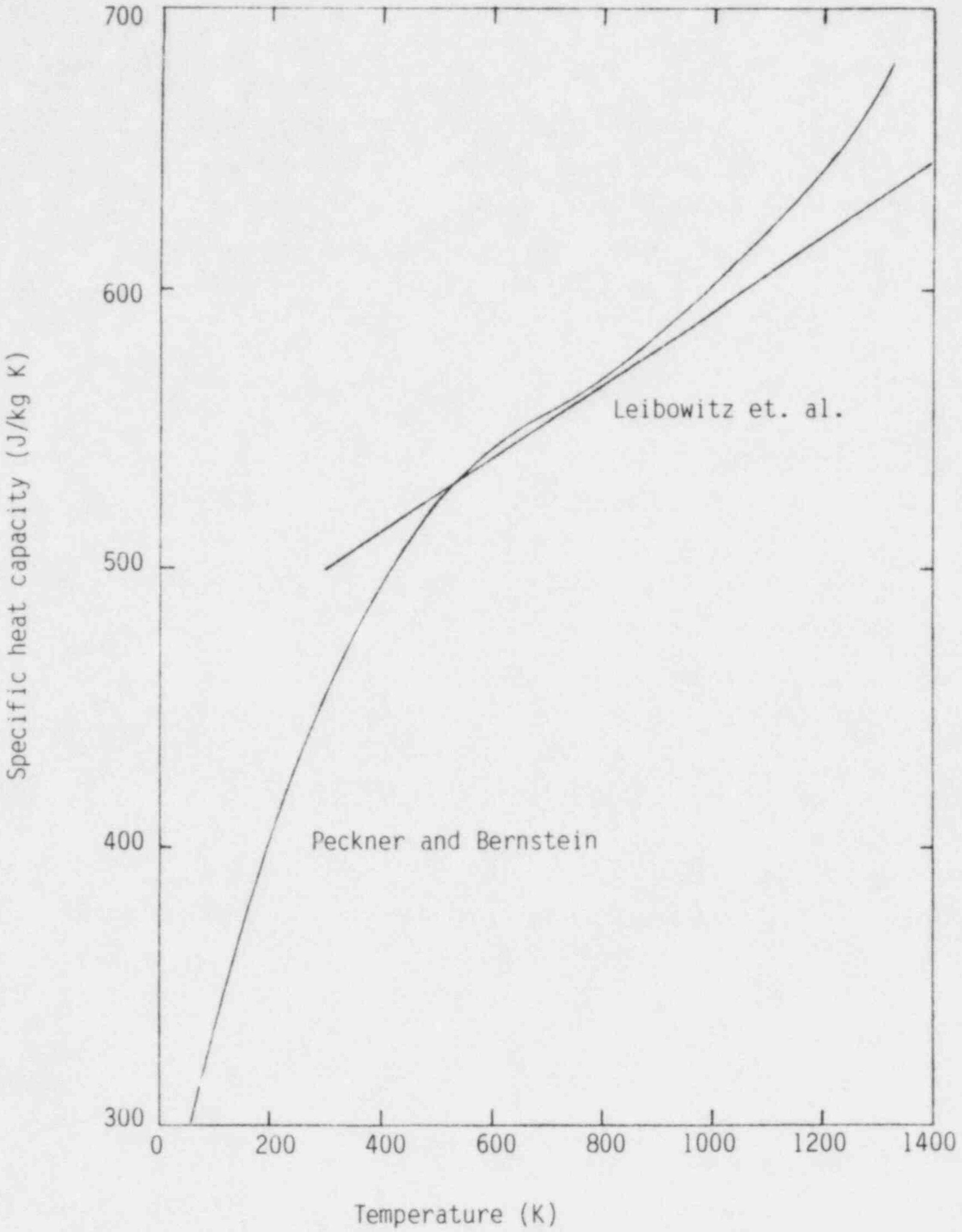

Figure 1. Specific heat capacity of 316 stainless steel given by Peckner and Bernstein[1] and by Leibowitz et al.[7]

TABLE 2. SPECIFIC HEAT CAPACITIES OF 316 STAINLESS STEEL FROM CURVES OF PECKNER AND BERNSTEIN[1] AND LEIBOWITZ ET AL.[7]

Temperature (K)	Specific Heat Capacity (J/kgK)	Reference
54	301	Peckner and Bernstein
121	352	Peckner and Bernstein
187	395	Peckner and Bernstein
255	431	Peckner and Bernstein
300	454	Peckner and Bernstein
346	473	Peckner and Bernstein
393	489	Peckner and Bernstein
445	507	Peckner and Bernstein
499	522	Peckner and Bernstein
544	531	Peckner and Bernstein
584	540	Peckner and Bernstein
622	545	Peckner and Bernstein
657	549	Peckner and Bernstein
693	554	Peckner and Bernstein
750	560	Peckner and Bernstein
809	569	Peckner and Bernstein
870	578	Peckner and Bernstein
922	588	Peckner and Bernstein
984	599	Peckner and Bernstein
1030	609	Peckner and Bernstein
1098	621	Peckner and Bernstein
1161	634	Peckner and Bernstein
1220	648	Peckner and Bernstein
1329	672	Peckner and Bernstein
300	499	Leibowitz et al.
400	513	Leibowitz et al.
500	526	Leibowitz et al.
600	539	Leibowitz et al.
700	552	Leibowitz et al.
800	566	Leibowitz et al.
900	579	Leibowitz et al.
1000	592	Leibowitz et al.
1100	606	Leibowitz et al.
1200	619	Leibowitz et al.
1300	632	Leibowitz et al.
1400	645	Leibowitz et al.

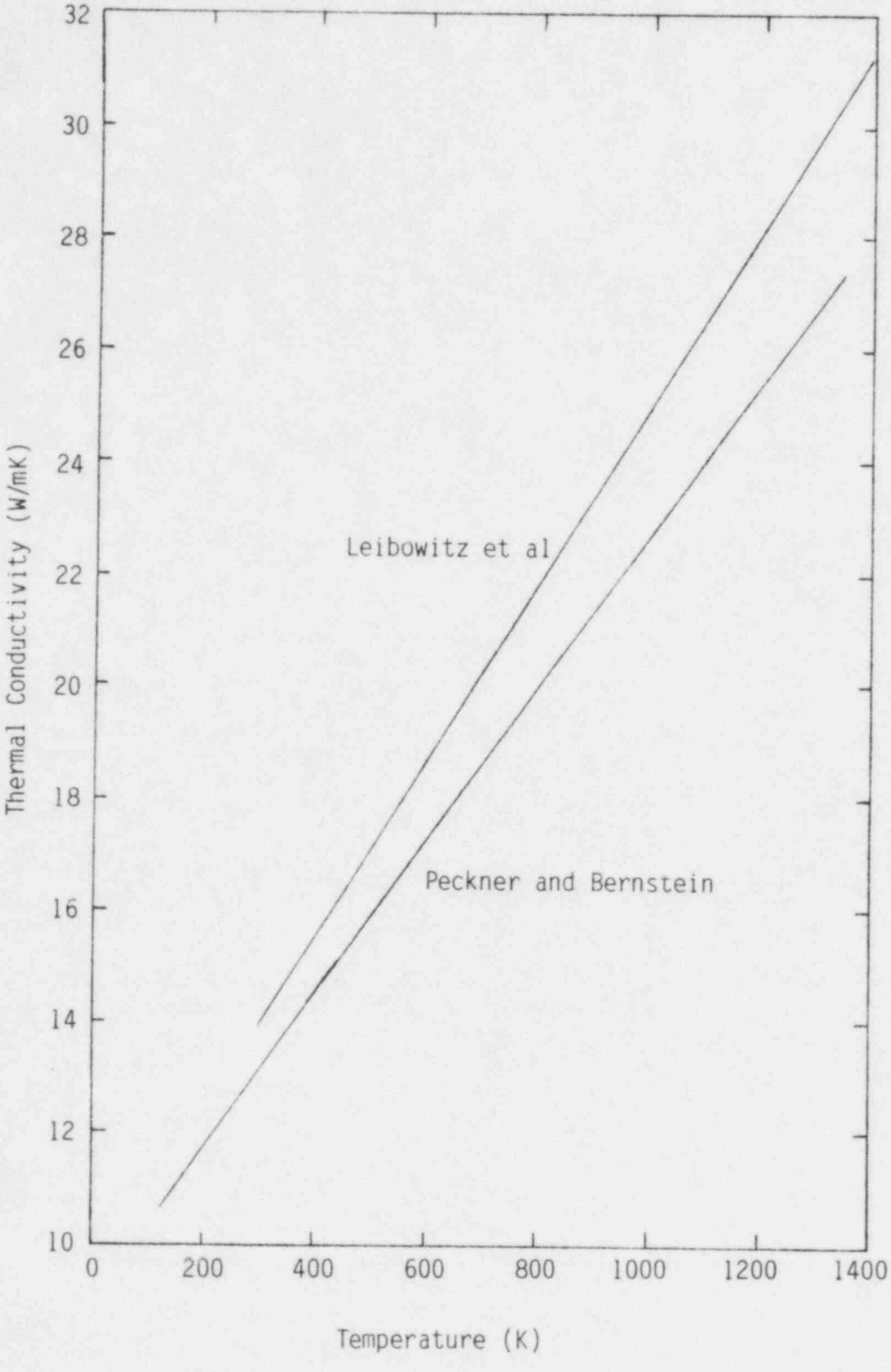

Figure 2. Thermal conductivity of 316 stainless steel given by Peckner and Bernstein[1] and by Leibowitz et al.[7]

TABLE 3. THERMAL CONDUCTIVITIES OF 316 STAINLESS STEEL FROM CURVES OF PECKNER AND BERNSTEIN[1] AND LEIBOWITZ ET AL.[7]

Temperature (K)	Thermal Conductivity (w/mK)	Reference
121	10.7	Peckner and Bernstein
434	15.0	Peckner and Bernstein
668	18.1	Peckner and Bernstein
970	22.3	Peckner and Bernstein
1342	27.4	Peckner and Bernstein
300	14.0	Leibowitz
600	18.7	Leibowitz
1000	25.0	Leibowitz
1400	31.3	Leibowitz

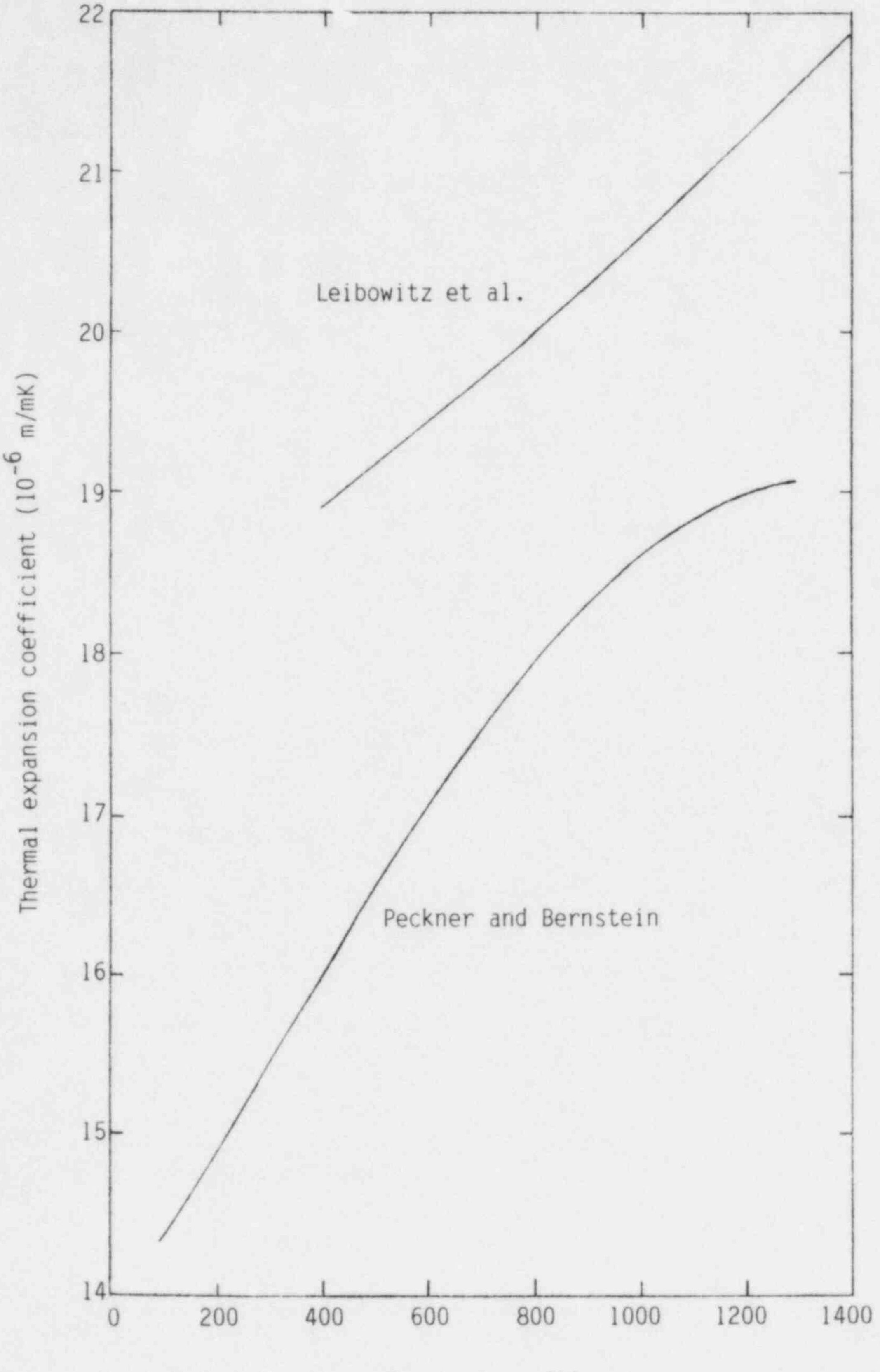

Figure 3. Thermal expansion coefficient of 316 stainless steel given by Peckner and Bernstein[1] and by Leibowitz et al.[7]

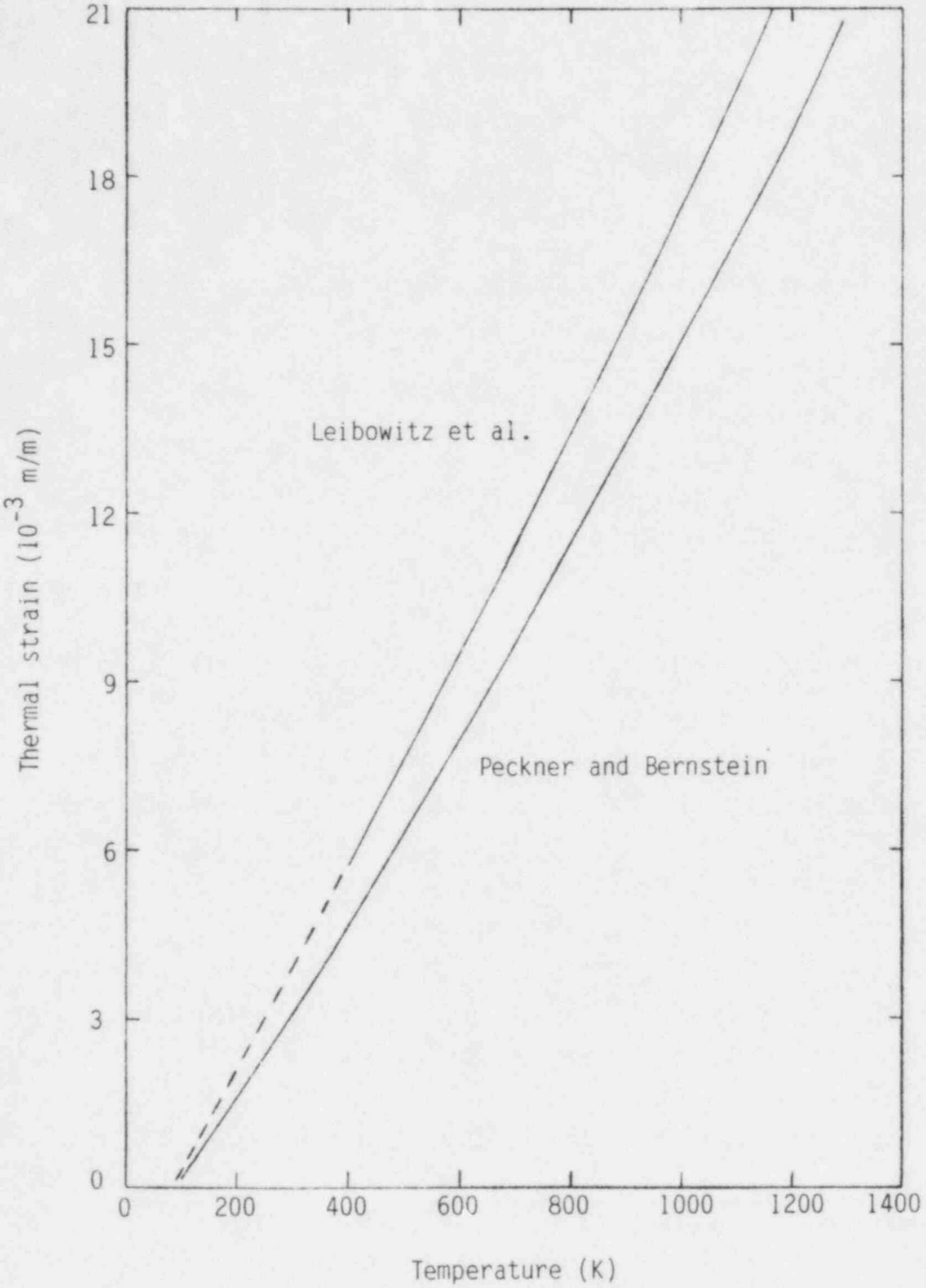

Figure 4. Thermal strain of 316 stainless steel referenced to 89.9 K obtained by integrating thermal expansion coefficients given by Peckner and Bernstein[1] and by Leibowitz et al[7].

and using a parabolic approximation for the area (Simpsons rule generalized to allow arbitrary abcissa intervals). The data of Reference 7 were integrated using the analytical expression given in this reference. The digitized thermal strains used to produce Figure 4 are listed in Table 4.

No data have been found for the emissivity of 316 stainless steel. Estimated values of this parameter range from 0.1 for a clean surface to 0.8 for an oxidized surface.

The heats of fusion and vaporization for 316 stainless steel have been reported to be 3610 cal/mol (2.68×10^5 J/kg) and 99720 cal/mol (7.41×10^6 J/kg) by Lebowitz.

2.1.2 Mechanical Properties

The mechanical properties of 316 stainless steel are difficult to obtain for many situations because they are strongly dependent on cold-work, irradiation, and impurity content. The existing data for elastic moduli, plastic moduli or creep, failure stress, cyclic fatigue, irradiation growth or swelling, and fracture toughness will be discussed.

Peckner and Bernstein[1] present both the shear modulus and Youngs modulus in tension. Their results (from Table 5 page 21-6) are reproduced in Table 5. The classical, slow reduction of both moduli with increasing temperature is apparent in the table. Although no data are available, it is reasonable to assume a slight reduction with radiation (about 10%) due to destruction of the solid lattice. The cubic structure of the steel also allows assumption of isotropy and the isotropic expression for Poisson's ratio

$$\nu = \frac{E}{2G} - 1 \qquad (1)$$

TABLE 4. THERMAL STRAINS OF 316 STAINLESS STEEL CALCULATED BY INTEGRATING CURVES OF PECKNER AND BERNSTEIN[1] AND LEIBOWITZ ET AL.[7]

Temperature (K)	Thermal Strain (10^{-3} m/m)	Source of Curve
89.9	0	Peckner and Bernstein
131.1	0.59	Peckner and Bernstein
172.2	1.19	Peckner and Bernstein
215.0	1.83	Peckner and Bernstein
255.5	2.44	Peckner and Bernstein
302.0	3.15	Peckner and Bernstein
343.3	3.79	Peckner and Bernstein
395.2	4.61	Peckner and Bernstein
424.8	5.08	Peckner and Bernstein
474.5	5.89	Peckner and Bernstein
519.6	6.64	Peckner and Bernstein
562.3	7.35	Peckner and Bernstein
607.4	8.12	Peckner and Bernstein
654.0	8.92	Peckner and Bernstein
702.1	9.75	Peckner and Bernstein
752.7	10.64	Peckner and Bernstein
807.0	11.61	Peckner and Bernstein
859.9	12.57	Peckner and Bernstein
911.2	13.50	Peckner and Bernstein
971.8	14.62	Peckner and Bernstein
1033.9	15.77	Peckner and Bernstein
1096.1	16.94	Peckner and Bernstein
1159.8	18.14	Peckner and Bernstein
1227.4	19.42	Peckner and Bernstein
1298.9	20.78	Peckner and Bernstein
89.9	0.00	Leibowitz
200	2.01	Leibowitz
300	3.86	Leibowitz
400	5.74	Leibowitz
500	7.64	Leibowitz
600	9.57	Leibowitz
700	11.53	Leibowitz
800	13.52	Leibowitz
900	15.53	Leibowitz
1000	17.58	Leibowitz
1100	19.66	Leibowitz
1200	21.77	Leibowitz
1300	23.91	Leibowitz
1400	26.08	Leibowitz

TABLE 5. 316 STAINLESS STEEL ELASTIC MODULI ACCORDING TO PECKNER AND BERNSTEIN[1]

Temperature (K)	Youngs Modulus ($10^9 N/m^2$)	Shear Modulus ($10^9 N/m^2$)
366	193.7	75.8
422	189.6	73.1
477	185.5	71.0
533	181.3	69.0
589	176.5	66.9
644	171.7	64.8
700	166.9	62.7
755	162.0	60.7
811	157.2	58.6
866	153.1	57.2
922	148.2	55.8
977	143.4	54.5
1033	137.9	53.1
1089	131.7	51.7

where

ν = Poisson's ratio (dimensionless ratio)

E = Young's modulus (N/m^2)

G = Shear modulus (N/m^2).

The only other values of elastic moduli found in the literature are values of 65.5×10^9 and 62.1×10^9 N/m^2 at 703 and 783 K, respectively, which are proposed by Barton and Higgins.[10]

Plastic deformation data have been reported by several authors.[11-15] The data, which are reproduced in Tables 6-9, display the usual decrease in yield and ultimate strength with increasing temperature. In addition, a pronounced increase in yield strength with either cold-work or neutron fluence is present. A smaller increase in ultimate strength with either cold-work or neutron fluence is also indicated by the tables.

The data for unirradiated samples are displayed along with curves of recommended values of yield and ultimate strength versus temperature in Figures 5 to 7. The recommended values are from a table published by Peckner and Bernstein.[1] Inspection of these figures shows that the curve of Peckner and Bernstein corresponds only to the data for annealed material. Material with 0.2 area reduction cold-work has yield strengths that are more than twice the yield strengths of the annealed material. The figures also show that considerable scatter, about ±0.15, must be expected for the strength of 316 stainless steel.

The existence of significant cold work (and carbide precipation[11]) effects suggests the need for models of annealing rates if temperatures above 600 K are attained. No data for these models were found.

TABLE 6. 316 STAINLESS STEEL PLASTIC DEFORMATION DATA FROM GROSSBECK AND MAZIASZ[15]

Temperature (K)	Cold Work (m^2/m^2)	Neutron Fluence (10^{26} n/m^2)	Yield Strength (10^6Pa)	Ultimate Strength (10^6Pa)	Uniform Elongation (m/m)
623	0.0	0.0	176	558	0.32
623	0.2	0.0	527	633	0.12
623	0.2	0.0	585	676	0.078
623	0.0	1.7	786	869	0.046
623	0.2	0.63	780	848	0.045
623	0.2	1.0	855	917	0.042
623	0.2	1.1	611	752	0.033
623	0.2	1.7	594	731	0.033
623	0.2	1.7	688	800	0.046
723	0.0	0.0	156	565	0.32
723	0.2	0.0	496	641	0.12
723	0.2	0.0	572	663	0.083
723	0.2	0.0	542	645	0.10
723	0.0	1.4	399	591	0.084
723	0.0	2.1	345	586	0.120
723	0.2	0.9	481	641	0.11
723	0.2	1.3	405	584	0.083
723	0.2	1.4	459	619	0.10
723	0.2	2.1	395	613	0.11
823	0.2	1.9	310	490	0.044
848	0.0	1.2	248	468	0.064
848	0.0	1.9	236	467	0.061
848	0.2	0.0	480	576	0.10
848	0.2	0.0	638	758	0.082
848	0.2	0.0	512	589	0.082
848	0.2	0.9	296	503	0.110
848	0.2	1.2	332	510	0.044
848	0.2	1.4	341	538	0.095
848	0.2	2.1	290	448	0.048

TABLE 7. 316 STAINLESS STEEL PLASTIC DEFORMATION DATA FROM JONES ET AL.[14]

Temperature (K)	Cold Work (m^2/m^2)	Neutron Fluence (10^{26} n/m^2)	Yield Strength (10^6 Pa)	Ultimate Strength (10^6 Pa)	Uniform Elongation (m/m)
293	0.0	0.0	307	525	--
293	0.0	3×10^{-5}	341	570	--
293	0.0	1×10^{-4}	357	503	--

TABLE 8. 316 STAINLESS STEEL PLASTIC DEFORMATION DATA FROM FENICI ET AL.[13]

Temperature (K)	Cold Work (m^2/m^2)	Yield Strength (10^6 Pa)	Ultimate Strength (10^6 Pa)	Uniform Elongation (m/m)	Comment
Room Temperature	0.0	379.5	588.4	0.5	Solution annealed
Room Temperature	0.0	315.7	607.5	0.586	Aged in vacuum, 873 K
873	0.0	203.3	383.6	0.314	Solution annealed
873	0.0	128.1	352.3	0.361	Aged in vacuum, 873 K

TABLE 9. 316 STAINLESS STEEL PLASTIC DEFORMATION DATA FROM BLOOM AND WIFFEN[11]

Temperature (K)	Cold Work (m^2/m^2)	Neutron Fluence ($10^{26} n/m^2$)	Yield Strength (10^6 Pa)	Ultimate Strength (10^6 Pa)	Uniform Elongation (m/m)
623	0.2	0.0	904.1	942.8	0.006
623	0.2	4.1	1010.	1039.	0.008
623	0.2	7.1	757.4	798.6	0.033
848	0.2	0.22	526.	588.	0.025
848	0.2	0.40	510.	540.	0.005
848	0.2	0.50	416.	435.	0.005
848	0.2	4.1	209.	283.	0.015
848	0.2	8.7	323.	323.	0.020
623	0.0	7.1	741.4	755.2	Not Reported
723	0.0	5.6	386.	418.	Not Reported
773	0.0	8.3	220.	305.	Not Reported
848	0.0	8.7	211.	254.	Not Reported
923	0.0	8.7	Not reported	57.	Not Reported
923	0.0	6.6	179.	179.	Not Reported
1023	0.0	6.9	Not reported	70.	Not Reported
698	0.2	7.7	499.	601.	Not Reported
773	0.2	8.3	438.	480.	Not Reported
953	0.2	8.7	Not reported	87.6	Not Reported

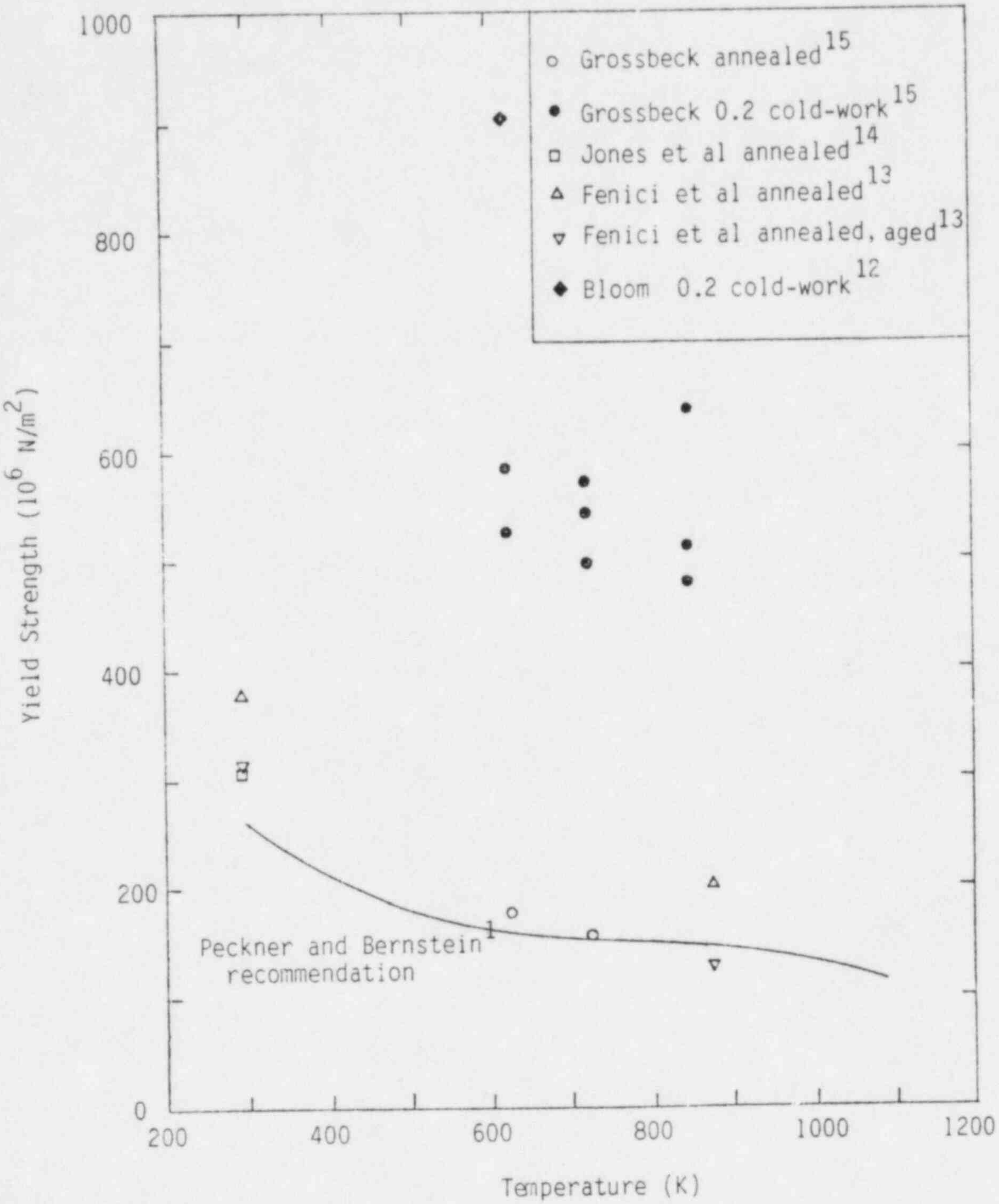

Figure 5. Data and values recommended for 316 stainless steel yield strength.

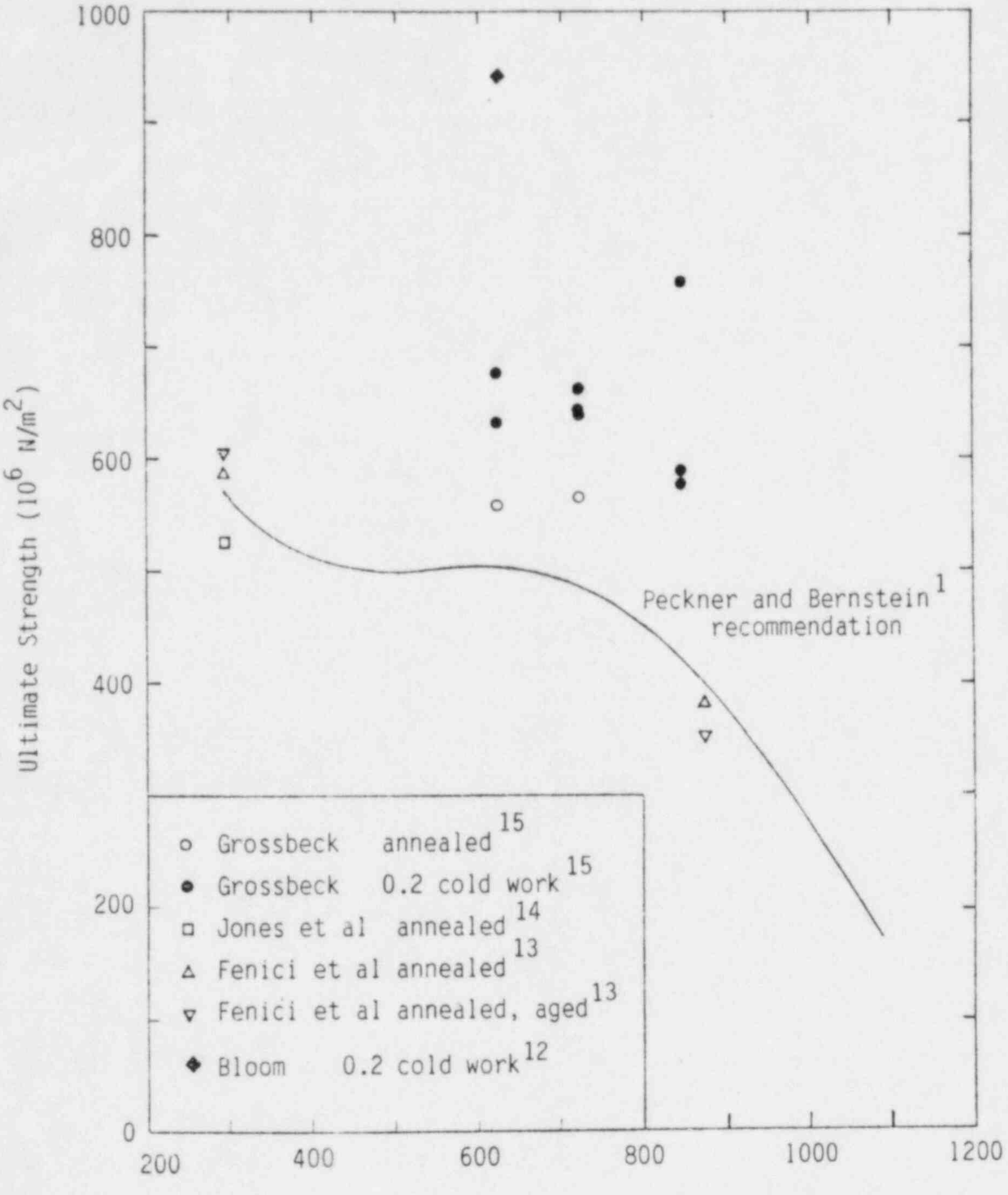

Figure 6. Data and values recommended for 316 stainless steel ultimate strength.

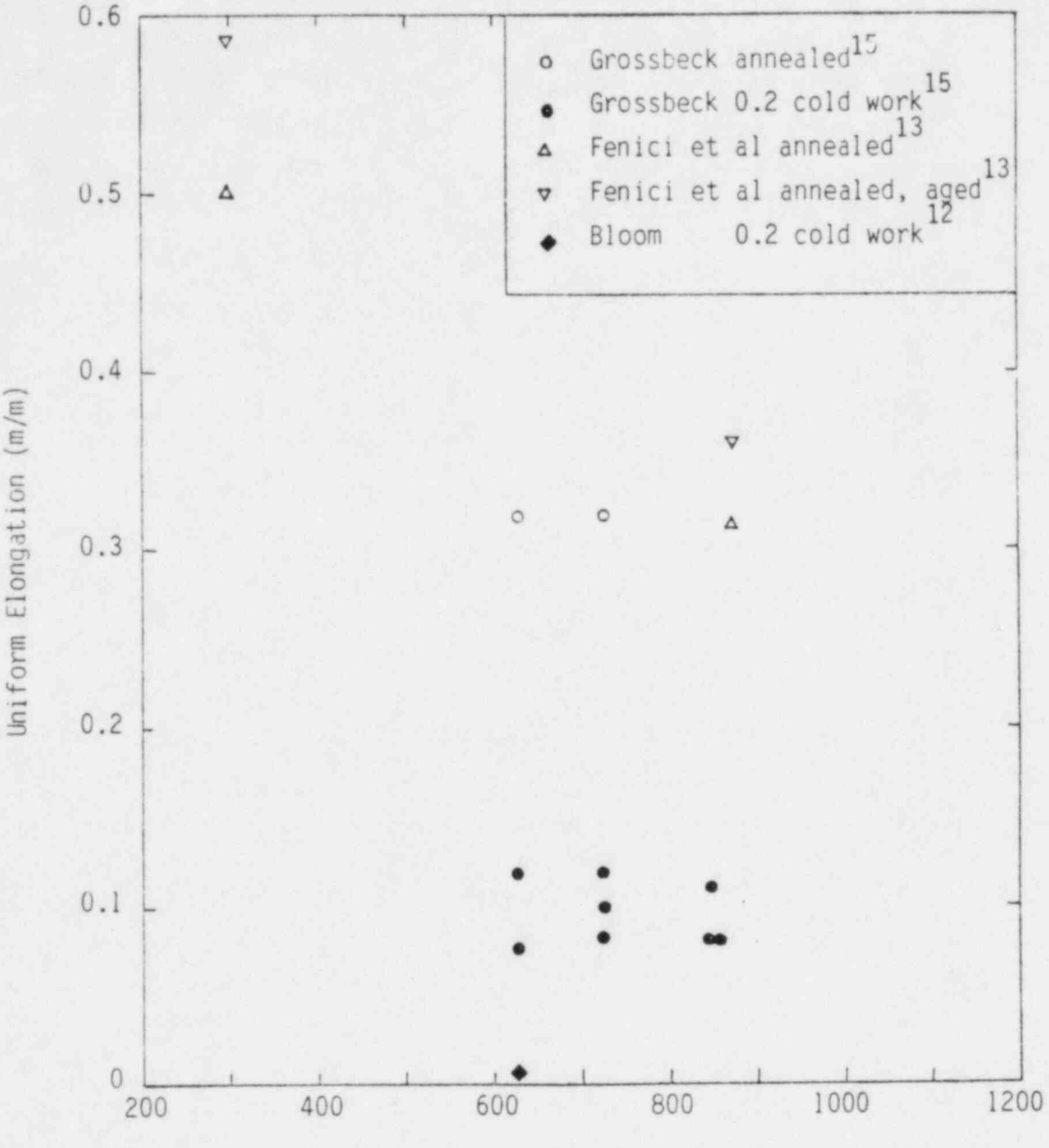

Figure 7. Data for 316 stainless steel uniform elongation.

Unfortunately, the data summarized in Figures 5 to 7 are not in the form that will be needed for analysis. Analysis of 316 stainless steel deformation will require some means of relating stress to deformation.[16] Since very few complete graphs of stress versus strain are published, the best one can do at present is to assume one of the classical equations of state for material deformation and fit the constants in this equation to force reproduction of the yield and ultimate strengths. The equation of state preferred by this author is a modified form of the Holloman relation

$$\sigma = K \, \epsilon^{n} \left[\frac{\dot{\epsilon}}{10^{-3}} \right]^{m} \tag{2}$$

where

σ = true stress[a] (Pa)

ϵ = true plastic strain[b] (m/m)

$\dot{\epsilon}$ = true plastic strain rate (s^{-1})

K = strength coefficient (Pa)

n = strain hardening exponent (dimensionless)

m = strain rate sensitivity exponent (dimensionless).

Evaluation of the three material constants, K, m, and n, requires not only the yield and ultimate strengths along with their corresponding strains but also measurement of the stresses required to produce two different strain rates at a given strain.

---

[a] True stress equals the force per unit cross-sectional area determined at the instant of measurement of the force.

[b] True strain equals the change in length divided by the length at the instant of change integrated from the original to the final length.

The strain rate sensitivity exponent is found from the ratios of the stresses and strain rates at constant strain

$$m = \frac{\ln\left(\frac{\sigma_1}{\sigma_2}\right)}{\ln\left(\frac{\dot{\varepsilon}_1}{\dot{\varepsilon}_2}\right)} \tag{3}$$

where

$\dot{\varepsilon}_1$ = strain rate imposed on a sample of 316 stainless steel (s^{-1})

σ_1 = stress required to produce $\dot{\varepsilon}$ (Pa)

$\dot{\varepsilon}_2$ = strain rate imposed on a sample of 316 stainless steel with the same strain as the sample used to measure $\dot{\varepsilon}_1$ (S^{-1})

σ_2 = stress required to produce $\dot{\varepsilon}_2$ (Pa).

These data are not available for 316 stainless steel. However, the strain rate sensitivity exponent is typically a very small number for temperatures less than half the melting point of the material (less than 850 K). This fact and the fact that most material tests are near a strain rate of 10^{-3}[a] allow approximation of the strain rate factor in Equation (2) by

$$\left[\frac{\dot{\varepsilon}}{10^{-3}}\right]^m \approx 1 \quad . \tag{4}$$

---

[a] Grossbeck and Maziasz[15] tested at an engineering strain rate = 4.6 x 10^{-5}/s Fenici et al.[13] tested at an engineering strain rate = 7.57 x 10^{-4}/s and Bloom and Wiffen[11] tested at an engineering strain rate = 4.67 x 10^{-5}/s.

The strength coefficient and strain hardening coefficient can be evaluated by requiring Equation (2) to reproduce the yield strength at a plastic strain of 0.002 and the ultimate strength at the uniform strain. In order to carry out the evaluation, the engineering stresses and strains given in Tables 2-5 are converted to true stresses and strains with the relations

$$\varepsilon = \ln(e + 1) \tag{5}$$

$$\sigma = S \exp(\varepsilon) \tag{6}$$

where

e = engineering strain[a] (m/m)

S = engineering stress[b] (Pa).

The yield strength, which is the stress at 0.002 plastic strain provides one equation in the two unknowns, K and n,

$$\sigma_{yield} = K[\ln(1.002)]^n \ . \tag{7}$$

The ultimate strength and corresponding uniform strain provide the necessary second equation,

$$\sigma_{ultimate} = K[\ln(1 + e_{uniform}])^n \tag{8}$$

---

[a] Engineering strain equals the change in length divided by the initial length.

[b] Engineering stress equals the force per unit initial cross-sectional area.

where

σ_{yield} = true stress at yield (Pa)

$\sigma_{ultimate}$ = true stress when engineering stress is at maximum (Pa)

$e_{uniform}$ = engineering strain when engineering stress is at maximum (m/m).

Equations of the form of Equation (2) cease to be accurate when strain rates decrease below 10^{-6}/s because an entirely different mechanism of deformation is operating. The available data for this kind of deformation are presented as either a minimum or an average creep rate as a function of temperature, stress, irradiation and/or cold work. Unfortunately, these average or minimum creep rates deal only with secondary or steady-state creep. A primary, transient stage of creep is not measured in any of the references found to date.[1,11,17,18] Another problem with the available data is that the irradiated material was all tested after irradiation when the flux was zero. The creep rates in flux may be quite different. It is interesting to note that even these zero-flux test results reproduced in Tables 10 to 12 show enhanced creep rates after irradiation. Additional problems are caused by non-standardized reporting. Some authors report just a stress (presumably an engineering stress) while others report true initial stress. Sometimes only creep elongation at failure is reported and other times the total elongation (presumably an initial strain upon loading plus the strain added during the creep test) is reported. If creep strains in 316 stainless steel turn out to be an important consideration, more carefully documented experiments will be required. At the present time, the most useful information is the recommended creep rates and rupture times contained in Figure 2 of Chapter 21 of Peckner and Bernstein.[1] This information is reproduced in Figure 8 of this report.

The only source of true failure stresses for 316 stainless steel that has been located is Bloom and Wiffen.[11] Their data are shown in Table 13 and Figure 9. The data show a clear trend for the true failure stress to

TABLE 10. 316 STAINLESS STEEL CREEP DATA FROM BLOOM AND WIFFEN[11]

Temperature (K)	Cold Work ($\Delta m^2/m^2$)	Neutron Fluence ($10^{26} n/m^2$)	Stress (10^6 Pa)	Creep Rate (m/ms)	Time to Rupture (s)	Creep Elongation (m/m)
823	0.0	0	310	3.9×10^{-9}	8.3×10^{6}	0.17
823	0.0	3.8	310	2.8×10^{-7}	1.6×10^{3}	0.001
823	0.2	0.5	310	1.7×10^{-8}	2.3×10^{5}	0.007
823	0.2	6.2	310	1.9×10^{-7}	2.0×10^{2}	0.011

TABLE 11. 316 STANLESS STEEL CREEP DATA FROM SIKKA AND DAVID[17]

Temperature (K)	Cold Work ($\Delta m^2/m^2$)	Neutron Fluence ($10^{26} n/m^2$)	Stress (10^6 Pa)	Minimum Creep Rate (m/ms)	Time to Rupture (s)	Creep Elongation (m/m)
811	0.0[a]	0.0	241	1.14×10^{-8}	8.65×10^{5}	0.103
866	0.0[a]	0.0	276	6.7×10^{-7}	6.23×10^{4}	0.179
866	0.0[a]	0.0	241	1.42×10^{-7}	1.70×10^{5}	0.149
866	0.0[a]	0.0	241	3.89×10^{-7}	1.01×10^{5}	0.145
866	0.0[a]	0.0	241	5.56×10^{-7}	1.52×10^{5}	0.144
866	0.0[a]	0.0	241	3.61×10^{-7}	5.18×10^{4}	0.146
866	0.0[a]	0.0	241	4.17×10^{-6}	5.4×10^{3}	0.151
866	0.0[a]	0.0	241	1.86×10^{-7}	2.47×10^{5}	0.143
866	0.0[a]	0.0	241	3.06×10^{-7}	6.88×10^{4}	0.089
866	0.0[b]	0.0	241	4.17×10^{-7}	2.16×10^{4}	0.072
866	0.0[b]	0.0	241	2.78×10^{-7}	1.50×10^{5}	0.167
866	0.0[b]	0.0	241	7.22×10^{-7}	6.55×10^{4}	0.137
866	0.0[b]	0.0	241	3.33×10^{-7}	1.01×10^{5}	0.106
866	0.0[b]	0.0	241	1.19×10^{-7}	2.29×10^{5}	0.114
866	0.0[b]	0.0	241	1.11×10^{-6}	2.40×10^{5}	0.078
866	0.0[a]	0.0	172	8.9×10^{-9}	9.61×10^{5}	0.072
866	0.0[a]	0.0	138	5.56×10^{-10}	3.56×10^{7}	0.058
922	0.0[a]	0.0	110	1.36×10^{-8}	4.96×10^{6}	0.304

[a] As-cast condition.

[b] Cast-and-annealed condition.

TABLE 12. 316 STANLESS STEEL CREEP DATA FROM LOVEL AND BARKER[18]

Temperature (K)	Cold Work ($\Delta m^2/m^2$)	Neutron Fluence ($10^{26} n/m^2$)	Stress ($10^6 Pa$)	Minimum Creep Rate (m/ms)	Time to Rupture (s)	Creep Elongation (m/m)
811	0.0	0.0	443	2.6×10^{-8}	9.47×10^5	0.389
811	0.0	1.2	415	2.97×10^{-7}	9.61×10^4	0.176
811	0.0	0.0	390	9.2×10^{-9}	1.55×10^6	0.182
811	0.0	1.2	366	8.86×10^{-8}	3.07×10^5	0.123
811	0.0	0.0	297	$2. \times 10^{-9}$	1.01×10^7	0.14
811	0.0	1.2	283	1.8×10^{-8}	5.39×10^5	--
866	0.0	0.0	345	6.94×10^{-7}	8.28×10^4	--
866	0.0	1.2	323	1.36×10^{-6}	4.14×10^4	0.141
922	0.0	0.0	214	5.89×10^{-7}	3.42×10^5	--
922	0.0	0.0	199	2.62×10^{-7}	6.05×10^5	0.51
922	0.0	0.0	176	1.77×10^{-7}	1.35×10^6	0.66
922	0.0	0.0	153	4.42×10^{-8}	4.66×10^6	0.35
922	0.0	1.2	152	2.81×10^{-8}	--	--
1033	0.0	0.0	118	2.43×10^{-6}	1.01×10^5	0.72
1033	0.0	1.2	117	2.63×10^{-6}	3.35×10^4	--
1033	0.0	0.0	83	2.51×10^{-7}	8.86×10^5	0.64
1033	0.0	1.2	83	1.83×10^{-7}	1.98×10^5	--
1033	0.0	0.0	69	7.92×10^{-8}	3.78×10^6	0.59
1033	0.0	1.2	69	6.44×10^{-8}	5.27×10^5	0.53

TABLE 13. 316 STAINLESS STEEL TRUE FAILURE STRESS DATA FROM BLOOM AND WIFFEN[11]

Temperature (K)	Cold-Work ($\Delta m^2/m^2$)	Neutron Fluence (10^{26} n/m^2)	True Failure Stress (10^6Pa)
623	0.2	0.0	1349
623	0.2	4.1	1074
623	0.2	7.1	934
848	0.2	0.22	600
848	0.2	0.40	541
848	0.2	0.50	438
848	0.2	4.1	286
848	0.2	8.7	324
623	0.0	7.1	763
723	0.0	5.6	421
773	0.0	8.3	313
848	0.0	8.7	256
923	0.0	8.7	57
923	0.0	6.6	178
1023	0.0	6.9	70
698	0.2	7.7	618
773	0.2	8.3	515
953	0.2	8.7	88

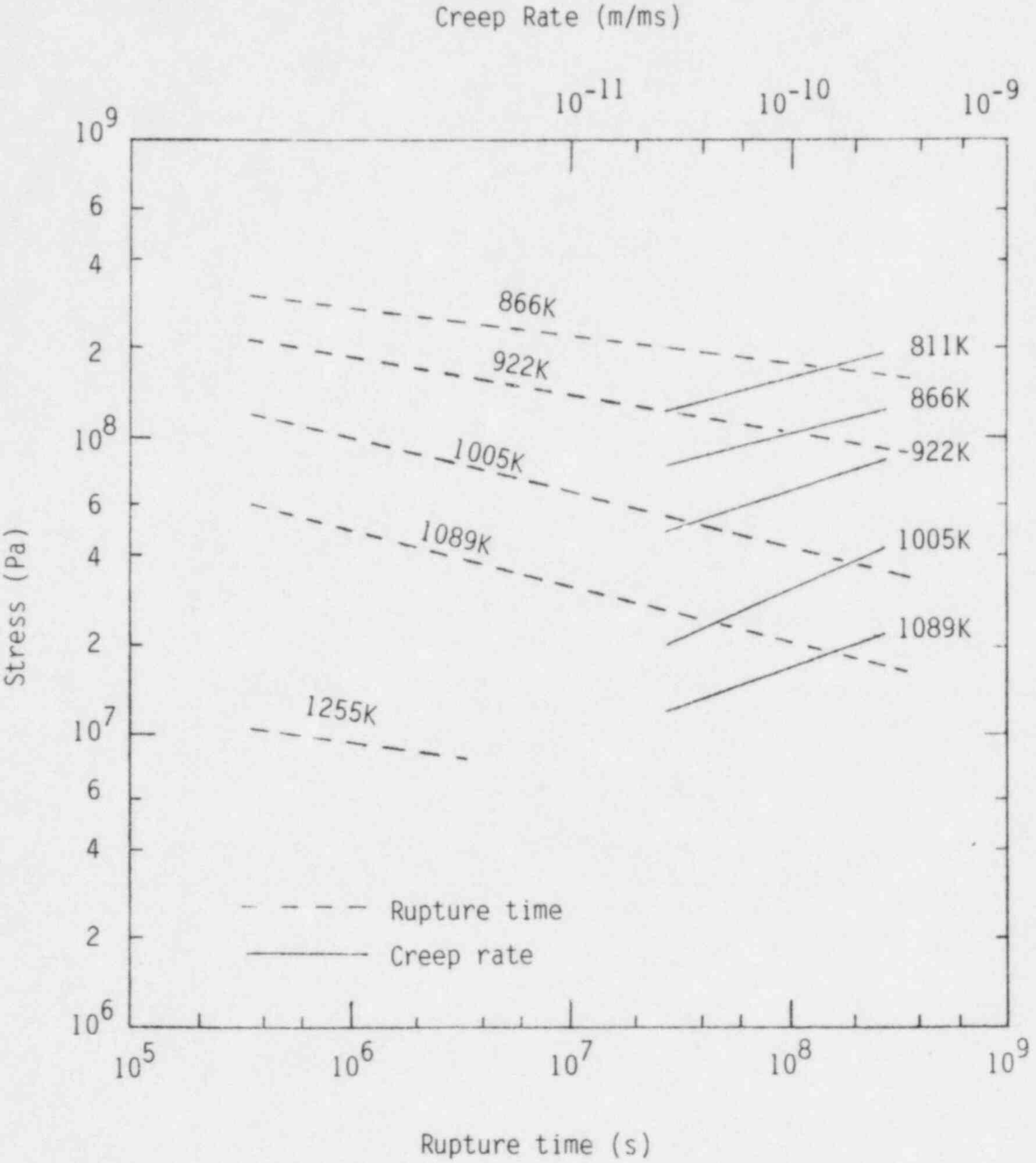

Figure 8. 316 stainless steel creep rates and rupture times recommended by Peckner and Bernstein.[1]

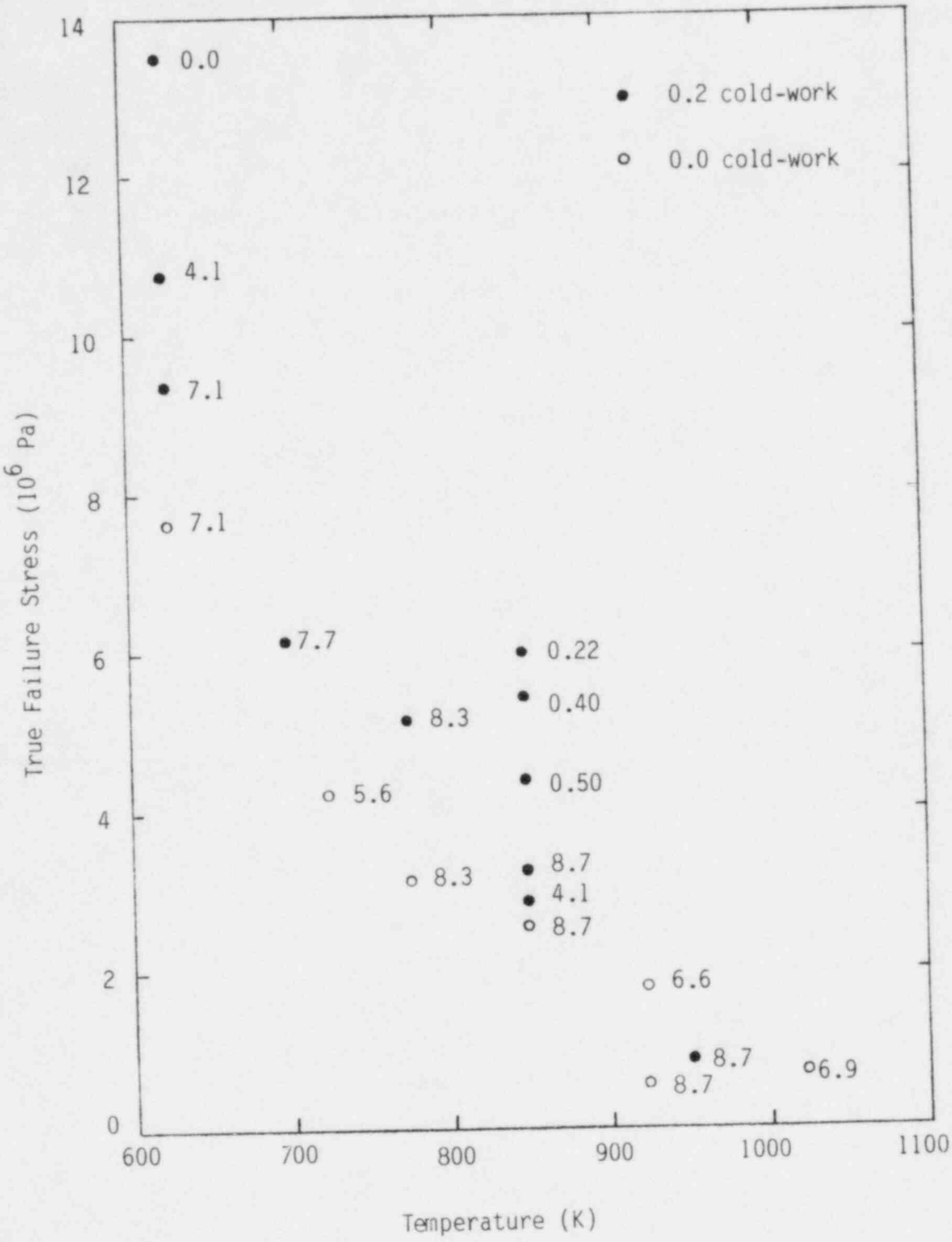

Figure 9. True failure stress as a function of neutron fluence, cold-work and temperature reported by Bloom and Wiffen.[11]

decrease with increasing temperature and neutron flux. Increasing the cold-work from 0.0 to 0.2 causes an increase in the true failure stress, however.

The literature that has been reviewed on cyclic fatigue of 316 stainless steel[6,12,19-24] is remarkable for the large number of discussions which have been published without their supporting data. Cyclic fatigue is often classified as "high cycle" or "low cycle," where the dividing line is 5,000 to 10,000 cycles to failure.[20] It is assumed that plastic strain is dominant for low cycle fatigue while elastic strain is dominant for high cycle fatigue and it is observed that low cycle fatigue life is reduced by irradiation while high cycle fatigue life is increased by irradiation. Important parameters in addition to the strain (stress) variation are neutron fluence, irradiation temperature, test temperature, hold time between cycles and the thermo-mechanical history of the sample. Cold-work and the type of environment have measurable effects too.[20]

Bloom[12] suggests that the cyclic fatigue data should be divided into intergranular crack propagation (at temperatures less than about half melting, 850 K) and intragranular crack propagation at higher temperatures. He also points out that two stages are required to produce cyclic failure--crack initiation and crack propagation. The obvious result of this observation is that the usual crack propagation description,

$$\frac{da}{dN} = B(\Delta K)^m \tag{9}$$

where

$\frac{da}{dN}$ = the change in crack length per cycle (m/cycle)

ΔK = the stress intensity range ($N/m^{1.5}$)

B,m = material parameters,

must be supplemented by some sort of an expression for initial crack size.

The only attempt to reduce data to an analytical form like Equation (9) that has been found is the effort by Davis et al.[6] This reference proposes the use of one of the following three expressions for 20% cold-worked 316 stainless steel in an air environment for temperatures in the range 297 to 866 K:

$$(\frac{da}{dN})_1 = \exp[7.26 \times 10^{-3}(T)-43.1]\ \Delta K^{18} \tag{10}$$

$$(\frac{da}{dN})_2 = \exp[0.008(T)-16.9]\ \Delta K^{1.5} \tag{11}$$

$$(\frac{da}{dN})_3 = \exp[4.54 \times 10^{-6}(T)^2-18.7]\ \Delta K^3 \tag{12}$$

where

$\frac{da}{dN}$ = fatigue crack growth rate (mm/cycle)

T = temperature (°C)

ΔK = stress intensity factor range (MPa m).

To determine which of the three equations to use for a particular T and ΔK, Davis offers the following set of rules:

1. Calculate

$$(\frac{da}{dN})_1,\ (\frac{da}{dN})_2 \text{ and } (\frac{da}{dN})_3 \quad .$$

2. Use Equation (10) if

$$(\frac{da}{dN})_1 < (\frac{da}{dN})_2 \quad ,$$

or if

$$(\frac{da}{dN})_1 < (\frac{da}{dN})_3 \quad .$$

3. Otherwise,

Use Equation (11) if

$$(\frac{da}{dN})_2 > (\frac{da}{dN})_3 \quad .$$

Use Equation (12) if

$$(\frac{da}{dN})_2 < (\frac{da}{dN})_3 \quad .$$

Equations (10) to (12) are said to be supported by data but neither the data nor references are published.

A second set of correlations is offered in Reference 6 which are apparently intended as an alternate means to predict cyclic failure when irradiation is present. In this case the expressions proposed are

$$\Delta \epsilon_T = 0.8 \, N_f^{-0.12} + 100 \, N_f^{-0.5} \tag{13}$$

and

$$\Delta \epsilon_T = 0.75 \, N_f^{-0.12} + 45 \, N_f^{-0.5} \tag{14}$$

where

$\Delta \epsilon_T$ = total strain range (%)

N_f = number of cycles to failure.

The first correlation is for $N_f < 3 \times 10^5$ cycles, a test temperature of 703 K, and a vacuum environment. The second correlation is for $N_f < 1 \times 10^5$ cycles, a test temperature of 703 K, an irradiation temperature of 703 K and a vacuum environment.

Again, no data or even references are presented in Reference 6 in support of these correlations and their relation to Equations (10) to (12) is not discussed.

Data have been published in References 21 through 23. Beeston and Brinkmann[21] report stress and strain range versus cycles to failure for samples with various combinations of cold-work and fast neutron fluence tested at 673, 873, or 973 K. The data are not reported here because crack propagation rate versus stress intensity data are required to obtain materials properties that are true materials properties and not a function of sample size and geometry.

The preferred form of the data is used by Michel and Smith.[22] These investigators provide data for zero-to-tension loading at 0.17 Hz in air. Annealed and 20% cold-worked 316 stainless steel is included and temperatures of 866 and 922 K were employed. Fast neutron fluences of 0, 1.2, 1.4, and 1.7×10^{26} neutrons were used and all tests were run with a hold time of one minute to observe the interaction of cyclic fatigue and creep. The data are reproduced in Table 14. When these data are plotted on log-log paper, the annealed material shows a distinct change in the slope as the temperature is increased from 866 to 922 K. Michel and Smith believe this change is associated with a change from transgranular fracture to a mixed trans- and intra-granular mode. The cold-worked material shows a sudden change in the slope of a plot of log (crack growth rate) versus log (stress intensity factor range) as the stress intensity is increased.

TABLE 14. 316 STAINLESS STEEL FATIGUE CRACK GROWTH RATES ACCORDING TO MICHEL AND SMITH[22]

Temperature (K)	Cold Work $(\Delta m^2/m^2)$	Fluence $(10^{26} n/m^2)$	Stress Intensity Factor Range $(10^6 Pa\sqrt{m})$	Crack Growth Rate $(10^{-6} m/cycle)$
922	0.0	1.2	36.1	30.5
			38.7	33.6
			41.4	50.2
			44.3	68.6
			48.1	178.
			52.2	415.
			56.2	629.
			61.6	1260.
			65.7	1266.
922	0.0	0.0	22.7	0.508
			24.3	0.708
			26.5	0.805
			28.6	1.32
			31.4	1.60
			35.1	3.16
			38.2	5.55
866	0.0	0.0	19.5	0.606
			21.7	0.731
			24.2	0.978
			26.5	1.35
			29.4	1.71
			32.8	2.85
			37.0	3.60
			41.4	6.32
			47.4	8.46
			54.5	9.95
			64.0	16.7
866	0.0	1.4	21.9	2.07
			23.9	1.85
			26.9	2.87
			29.8	4.07
			33.3	5.85
			37.0	8.19
			42.0	12.1
			47.2	16.4
			55.0	23.2
			64.2	50.3

TABLE 14. (continued)

Temperature (K)	Cold Work ($\Delta m^2/m^2$)	Fluence ($10^{26} n/m^2$)	Stress Intensity Factor Range ($10^6 Pa\sqrt{m}$)	Crack Growth Rate ($10^{-6} m/cycle$)
922	0.2	1.4	20.4	411.
			21.8	398.
			23.2	427
			24.5	483.0
			26.1	519.
			27.9	626.
			30.2	726.
			32.2	929.
922	0.2	0.0	28.1	0.779
			29.9	0.847
			31.6	0.971
			33.7	1.16
			35.7	1.44
			39.0	1.95
			43.1	2.39
			46.5	3.28
			49.5	3.26
			53.3	5.19
			57.5	8.61
			62.2	8.66
			66.8	26.2
			72.6	26.2
866	0.2	0.0	22.8	9.79
			25.2	10.05
			27.7	10.5
			31.0	10.6
			35.1	11.1
			39.6	11.2
			45.0	17.5
			51.7	26.2
			59.7	46.3
			69.8	84.1
866	0.2	1.7	20.4	101.
			22.4	131.
			24.8	160.
			27.5	180.
			30.7	208.
			34.3	253.
			38.9	293.
			44.2	447.
			51.3	579.
			58.9	750.

Figure 10 is a comparison of those data of Table 14 which are taken at 866 K using material with a cold-work of 0.2 to the predictions of Equations (10), (11), and (12). Since Reference 6 reports these Equations are within a factor of two of their data, the figure demonstrates that hold time and irradiation effects are both important considerations in determining crack growth rate that are not considered by the authors of Reference 6.

Crack growth data and correlations have been published by Nagata et al.[23] but the data are not reproduced here because they relate plastic strain range to number of cycles required for failure. Such data are a function of sample size and shape and thus not a material property.

The irradiation growth and swelling of 316 stainless steel are typically not considered to be materials properties and therefore will not be discussed in detail. Swelling models and data for 316 stainless steel are available in References 25 through 28.

Unfortunately, few fracture toughness data have been found for 316 stainless steel. General trends are discussed by Peckner and Bernstein[2] and in Fickett et al.[29] Table 15 reproduces the low temperature fracture toughness data for 316 stainless steel welds shown in Figure 3 of Reference 29.

2.1.3 Electromagnetic Properties

The electrical resistivity of 316 stainless steel at room temperature is given by Peckner and Bernstein[1] as 7.3×10^{-7} ohm-m. These authors report the room temperature magnetic permeability is 1.008.

Davis[6] offers correlations for the electrical resistivity for temperatures between 0 and 1000 K. The expression Davis proposes for unirradiated material is

$$\rho = 54.4 \times 10^{-8} + 3.70 \times 10^{-10} T + 3.60 \times 10^{-7} \exp(-344.8/T) \qquad (15)$$

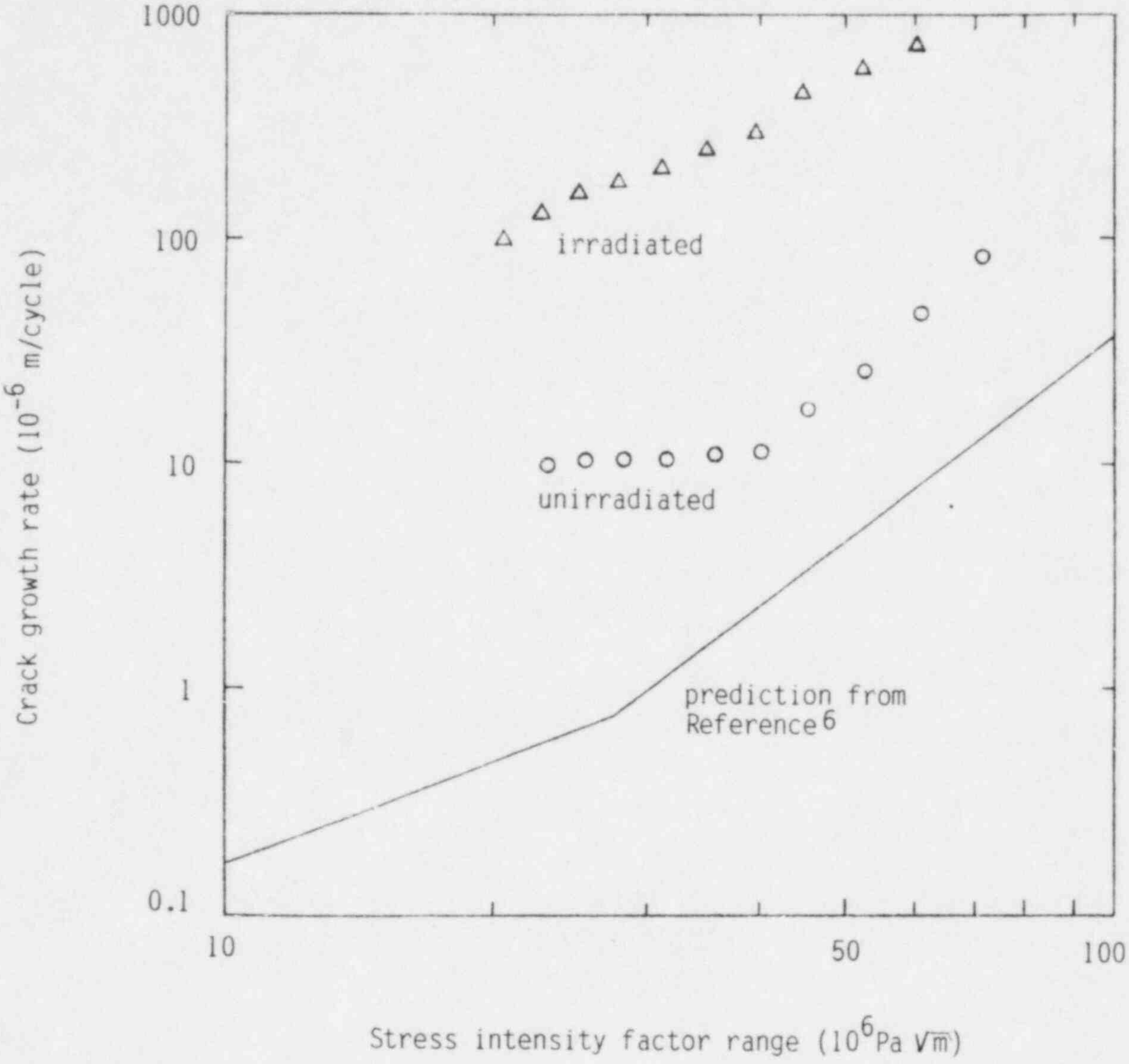

Figure 10. Comparison of 316 stainless steel crack growth rate data from Michel and Smith[22] with a one minute hold time to crack growth predictions from Reference 6.

TABLE 15. FRACTURE TOUGHNESS OF 316 STAINLESS STEEL WELDS ACCORDING TO FICKETT ET AL.[29]

Temperature (K)	Ferrite in Weldment (percent)	Fracture Toughness (10^6 Pa $\sqrt{m}$)
4	1.0	154
76	1.0	158

where

T = temperature (K)

ρ = electrical resistivity of unirradiated material (ohm-m).

He sugests correcting irradiated material for the effects of voids by using the following expression

$$\rho_{irr} = \left(\frac{100 + 0.5 \frac{\Delta V}{V}}{100 - \frac{\Delta V}{V}} \right) \rho \tag{16}$$

where

ρ_{irr} = irradiated resistivity (ohm-m)

$\frac{\Delta V}{V}$ = bulk swelling in %.

Equation (15) predicts 7.69×10^{-7} ohm-m at 300 K in reasonable agreement with the 7.3×10^{-7} ohm-m recommended by Peckner and Bernstein.[1]

Stanley[30] has measured the magnetization of commercial 316 stainless steel as a function of temperature, neutron fluence (>0.1 MeV), and applied field. He reports mixed results, with the Langevin function giving a reasonable fit to his data for specimens irradiated to a high neutron fluence but a simple straight line giving a better result for low fluences and high fields. The slope and intercept for Stanley's linear correlation between magnetization and applied field is given in Table 16. The sample which was used to produce the correlation was irradiated to a fluence of 1.8×10^{26} n/m^2 at 698 K.

TABLE 16. SLOPE AND INTERCEPT FOR STANLEY'S[30] LINEAR CORRELATION BETWEEN MAGNETIZATION AND APPLIED FIELD

Temperature (K)	Interrept (10^{-3} Tesla)	Slope (10^{-3} Tesla/Tesla)
317	9.35	4.60
264	12.1	4.89
204	21.1	5.18
165	27.5	5.34
153	30.3	5.79
82	43.4	7.58

2.1.4 Physical/Chemical Properties

The physical/chemical properties that will be required for fusion reactor modeling are a function of the mechanistic detail that is considered in the models. Since many of these models are only in the initial stage of development, the number of properties considered can be expected to change as modeling needs become better defined. At the present time the 316 stainless steel properties that are expected to be needed are density, melting temperatures, hydrogen isotopes permeability, hydrogen isotopes diffusion rates, hydrogen isotopes solubility, hydrogen isotopes reflection coefficients, hydrogen isotopes trapping coefficients, hydrogen isotopes molecular recombination rates, hydrogen isotopes sputtering yields, corrosion rates in lithium, corrosion rates in water, and activation products decay times.

Peckner and Bernstein[1] report a density of 8000 kg/m^3 at 300 K and a melting range of 1644-1672 K for 316 stainless steel. The melting range is some 25 K lower than most other stainless steels but the density is typical. Densities at temperatures other than 300 K can be calculated using the thermal strain data of Section 2.1.1.

Hydrogen isotope permeability, diffusion rates, and solubility in 316 stainless steel are discussed in several recent publications. Although no published solubility data have been found, Figure 1 of Maroni and Van Deventer[31] provides an expression (Sievert's law) to calculate it,

$$S = 6.3 \exp(-3155/T) \sqrt{P} \qquad (17)$$

where

S = amount of hydrogen dissolved (atomic parts per million)

P = pressure (Pa)

T = temperature (K).

Permeability data from several sources are also presented and discussed by Maroni and Van Deventer. The permeation rate (flux) of hydrogen through 316 stainless steel when the surfaces of the steel are clean and the driving force is a concentration gradient[a] is reported in Figure 3 of Reference 31 to be

$$\phi = 0.217 \exp(-7823/T) \frac{\Delta(\sqrt{P})}{X} \tag{18}$$

where

ϕ = flux of hydrogen through a 316 stainless steel plate (cm^3 of hydrogen at STP/m^2 s)

X = plate thickness (m)

$\Delta(\sqrt{P})$ = difference of the square root of pressure across the plate ($\sqrt{10^3 \text{ Pa}}$).

Maroni and Van Deventer point out that the permeability is the direct product of the hydrogen concentration gradient and the bulk diffusion coefficient (Fick's law) when bulk diffusion due to a concentration gradient is the rate controlling process

$$J = -D \frac{dc}{dx} \quad -D \frac{\left(S'_{\text{one face}} - S'_{\text{other face}}\right)}{X} \tag{19}$$

where

J = flux of hydrogen through a 316 stainless steel plate (kg hydrogen/m^2 s)

---

[a] The concentration gradient is caused by a solubility difference at the two surfaces which is in turn caused by a difference in the hydrogen partial pressures at the two surfaces.

D = hydrogen bulk diffusion coefficient (m^2/s)

$\frac{dc}{dx}$ = concentration gradient (kg hydrogen/m^4).

When Equations (17) to (19) are combined one obtains a bulk diffusion coefficient of

$$D = 6.8 \times 10^{-7} \exp(-4668/T) \qquad (20)$$

for hydrogen when proper account is taken of the different units of Equations (15) and (16).[a] This coefficient predicts a somewhat more rapid diffusion than the tritium bulk diffusion found by Austin and Elleman[32] over the temperature range 298-500 K,

$$D_T = 1.8 \times 10^{-6} \exp(-7079/T) \qquad (21)$$

where

D_T = tritium bulk diffusion coefficient (m^2/s).

The Austin and Elleman coefficient is fairly consistent with the result obtained by Wilson and Baskes[33] for deuterium in 316 stainless steel when one considers the effect of the differing isotope masses,

$$D_D = 1.2 \times 10^{-5} \exp(-7096/T) \qquad (22)$$

where

D_D = deuterium bulk diffusion coefficient (m^2/s).

---

[a] In order to obtain Equation (20) the following units conversions were used: 1 m^3 of hydrogen at STP = 8.88×10^{-2} kg hydrogen. 1 atomic ppm in 316 stainless steel = 1.43×10^{-4} kg hydrogen/m^3 steel.

The difference between Equation (20) and the others may be due to surface oxide effects which slow the permeation[36] or to grain boundary diffusion which is much more rapid than bulk diffusion in 316 stainless steel.[34]

Calculations of hydrogen retention and release in the first walls of fusion reactors require consideration of the fact that the hydrogen diffusion across the wall is not driven by pressure differences.[37-40] Hydrogen isotope reflection coefficients, trapping coefficients and molecular recombination data are needed to describe the interchange of hydrogen isotopes between a plasma and the first wall.

Reflection coefficients as a function of incident particle energy have been published by Eckstein et al.[41] and by Thomas.[42] These results are reproduced in Tables 17 and 18 and are illustrated in Figure 11. The data show that the isotope (mass) of the incident particle is not as important as the particle's incident energy in determining the probability of reflection from a stainless steel surface. Hydrogen with an incident energy above 5×10^{-16} J/nucleon is likely to remain in or on the stainless steel. Additional reflection coefficient data are discussed in Reference 37.

Deuterium trapping coefficients for stainless steel surfaces as a function of dose for several temperatures have been published by Freeman et al.[43] These coefficients are reproduced in Table 19 and Figure 12. The trapping coefficients decrease from nearly one at small doses when the traps are empty to zero at doses of sufficient magnitude that all the surface traps in the steel are full. At temperatures above 390 K the traps are not occupied to any significant amount because the trap binding energies are less than the thermal energies of the implanted deuterons.

When temperatures are high enough to free trapped implanted hydrogen isotopes, the release of these isotopes from the steel surface is controlled by the rate of isotope recombination to form molecules.[39] The parameter used to describe this rate is the recombination rate constant, defined by the relation

TABLE 17. HYDROGEN-ON-STAINLESS STEEL REFLECTION COEFFICIENTS ACCORDING TO ECKSTEIN ET AL.[41]

Particle	Primary Energy (10^{-16} Joules/Nucleon)	Reflection Coefficient
D_2	3.95	0.228
D_2	7.81	0.126
D_2	12.01	0.103
H_3	8.09	0.126
H_2	3.95	0.186
H_2	7.97	0.119
H_2	12.04	0.091
H	12.01	0.083
H	16.01	0.069
H	20.03	0.057
H	24.05	0.047

TABLE 18. HYDROGEN-ON-STAINLESS STEEL REFLECTION COEFFICIENTS ACCORDING TO THOMAS[42]

Particle	Primary Energy (10^{-16} Joules/Nucleon)	Reflection Coefficient
D^+	0.214	0.500
D^+	0.441	0.419
D^+	0.870	0.404
D^+	1.32	0.356
D^+	1.80	0.311

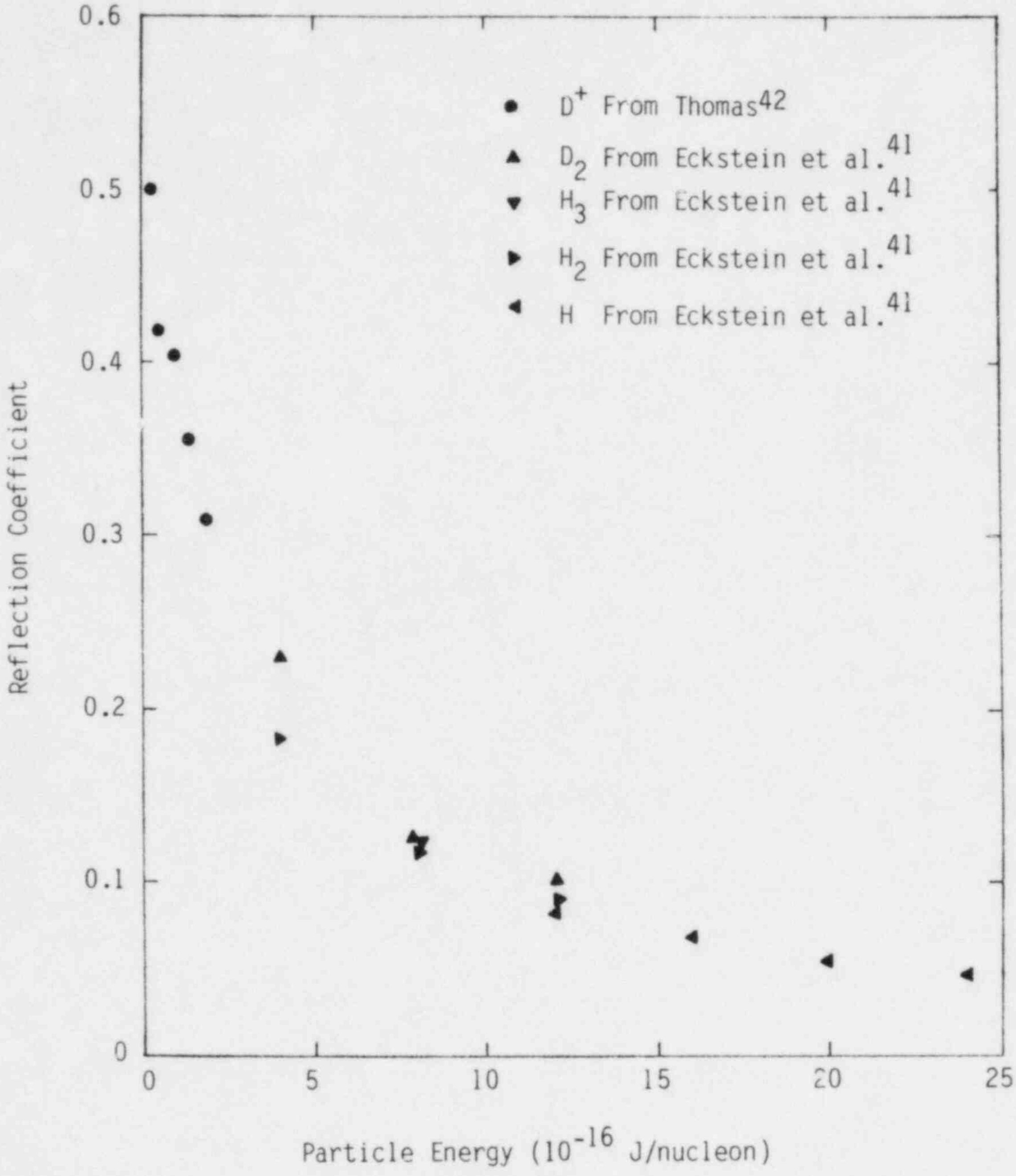

Figure 11. Reflection coefficients for hydrogen isotopes incident on stainless steel.

TABLE 19. TRAPPING COEFFICIENT FOR DEUTERIUM IONS ON A STAINLESS STEEL SURFACE FROM FREEMAN ET AL.[43]

Temperature (K)	Dose (10^{20} atoms/m^2)	Trapping Coefficient
173	149.	0.75
173	161.	0.54
173	165.	0.44
173	181.	0.33
173	191.	0.25
173	214.	0.18
173	245.	0.12
173	304.	0.04
173	380.	0.01
300	11.3	0.60
300	15.3	0.50
300	19.5	0.39
300	22.3	0.30
300	30.6	0.19
300	41.6	0.15
300	53.0	0.03
300	62.5	0.01
390	2.87	0.86
390	4.17	0.71
390	5.78	0.58
390	7.25	0.34
390	8.80	0.17
390	11.8	0.07
390	14.7	0.04
390	17.9	0.02

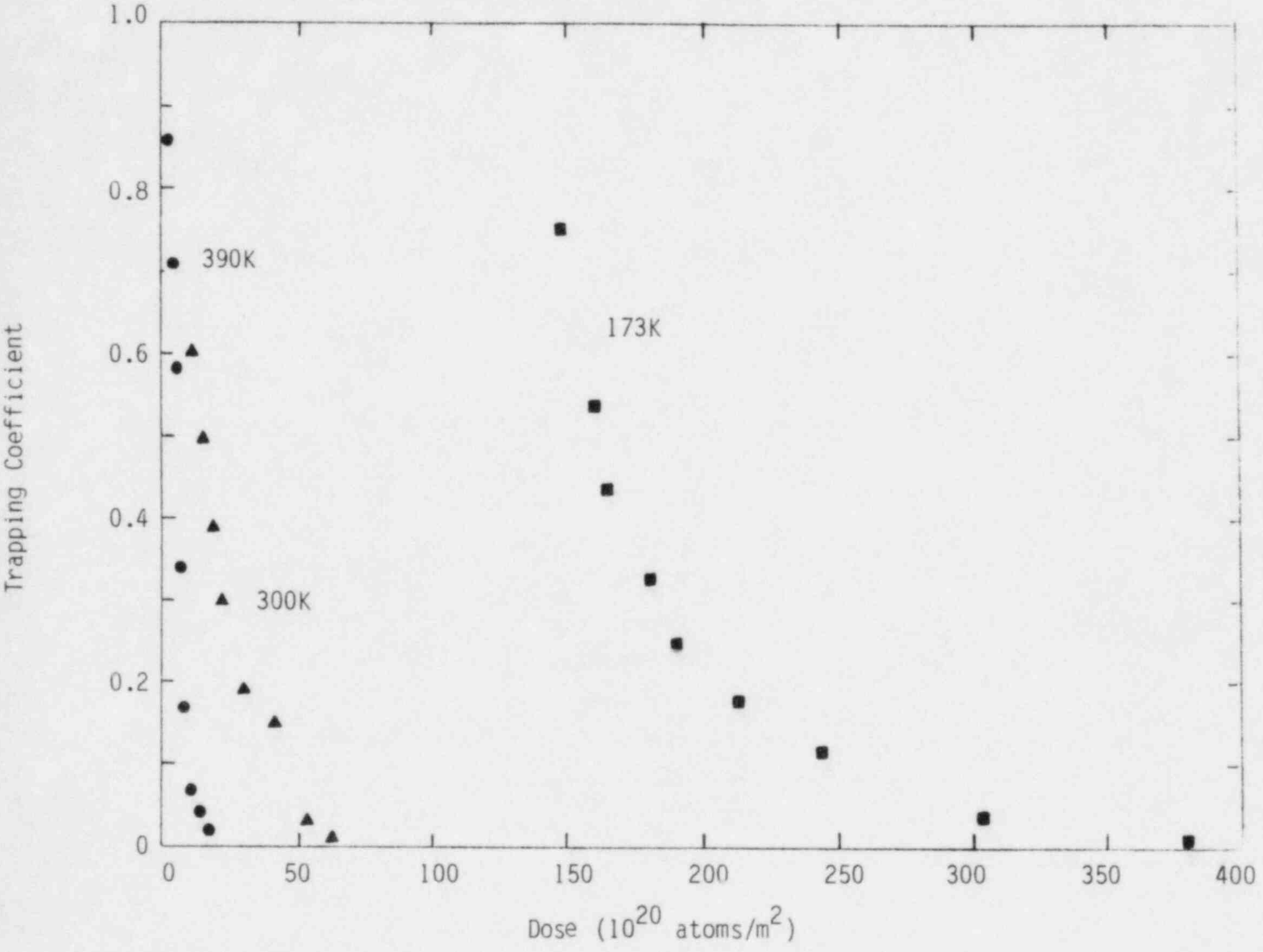

Figure 12. Trapping coefficients for deuterium ions incident on stainless steel.

$$J = k_r c^2 \qquad (23)$$

where

J = flux of hydrogen isotope released from the surface to the gas phase (molecules isotope/m^2s)

k_r = recombination rate coefficient (molecules isotope m^4/atoms isotope^2 s)

c = surface concentration of isotope atoms (atoms isotope/m^3).

Braun et al.[44] have published recombination rate coefficient data for deuterium on stainless steel. Their data are reproduced in Table 20. In addition Wilson has published a summary of recombination rate coefficient data attributed to several sources. Many of the references credited by Wilson do not report recombination rate coefficients[45,46] but do provide information and data which Wilson apparently used to calculate the coefficients. The rates reported by Wilson which this author has not been able to find elsewhere are reproduced as Table 21.

Figure 13 shows all of the recombination rate coefficients from Tables 20 and 21 and one datum from Wienhold et al.,[47] 4.4×10^{-33} m^4/s at 323 K. The figure illustrates the orders-of-magnitude scatter in the data as they are presently characterized and suggests that important surface effects are not being measured when the data are viewed as a function of temperature alone.

Surface sputtering yield data have been measured and studied extensively but no completely satisfactory modeling approach is available. Extensive data (from other sources that were not completely identified) have been surveyed by Anderson and Bay[48] who found (their Figure 2) yields within an order of magnitude of 10^{-2} atoms sputtered/incident ion for

TABLE 20. DEUTERIUM RECOMBINATION RATES ON STAINLESS STEEL ACCORDING TO BRAUN ET AL.[44]

Temperature (K)	Recombination Rate Coefficient (molecules D_2 m^4/(atoms steel)^2 s)
866	3.82×10^{-29}
789	8.99×10^{-30}
741	1.31×10^{-30}
704	2.63×10^{-31}
665	4.03×10^{-32}
661	1.03×10^{-32}
653	4.76×10^{-33}
629	3.91×10^{-32}
591	2.85×10^{-33}
563	6.59×10^{-33}
554	1.91×10^{-33}
545	4.76×10^{-33}
453	2.46×10^{-34}
419	3.86×10^{-35}

TABLE 21. HYDROGEN ISOTOPE RECOMBINATION RATES REPORTED BY WILSON[39]

Temperature (K)	Recombination Rate Coefficient (molecules Isotope $m^4/(\text{atoms steel})^2$ s)	Comment
668	1.49×10^{-29}	Attributed to Reference 45
580	1.97×10^{-30}	Attributed to Reference 45
480	8.39×10^{-32}	Attributed to Reference 45
426	7.24×10^{-33}	Attributed to Reference 45
379	7.90×10^{-34}	Attributed to Reference 45
358	1.54×10^{-34}	Attributed to Reference 45
303	6.42×10^{-36}	Attributed to Reference 45
297	3.31×10^{-33}	Attributed to Reference 46
370	1.66×10^{-31}	Measured by Wilson and Baskes[39]

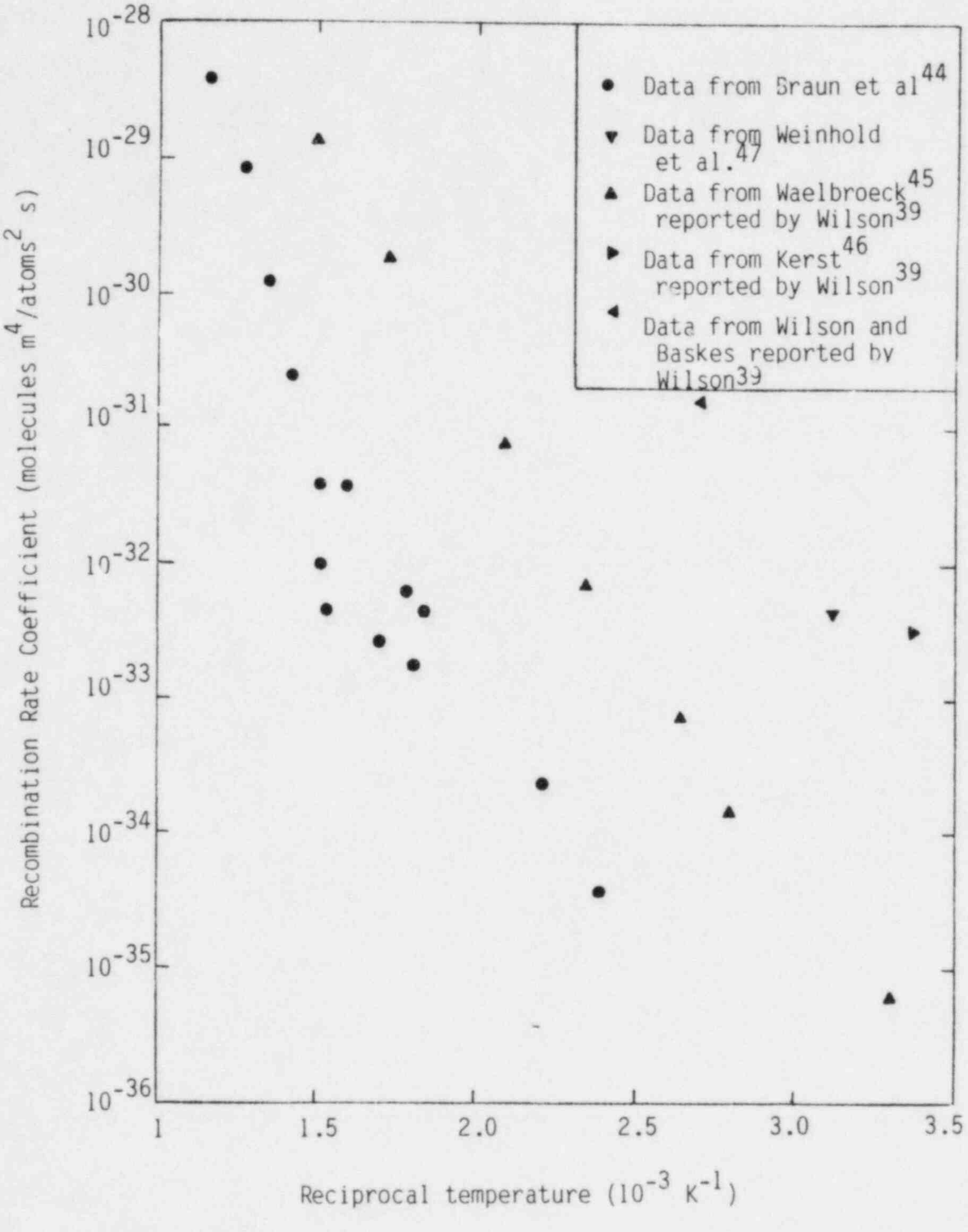

Figure 13. Recombination rate coefficients for hydrogen isotopes on stainless steel.

hydrogen isotopes on stainless steel with incident energies in the range 0.2 to 10 KeV. Behrisch et al.[49] report similar data. An excellent summary of the older data is provided in Reference 37 which concludes that there is a sparcity of data below 8 x 10^{-17} joules ion energy.

A more mechanistic approach has been taken by Bohdansky[50] who uses the theory of Sigmund[51] to deduce an analytic expression for sputtering yields as a function of the surface binding energy (sublimation energy according to Figure 16 of Reference 51), the ion incident energy, the charges and the masses of the target and incident ions. The problem with using this mechanistic approach is that it merely replaces the correlations to somewhat scattered data for sputtering yields with an uncertain number for the surface binding energy of the target and a library of target and incident ion masses and atomic charges. For most purposes, correlations based on the extensive data published by Anderson and Bay[48] would suffice if the references to their sources were available.

Only limited data for the corrosion of 316 stainless steel are available. Whitlow et al.[52] have published three measurements of the mass loss of 316 stainless steel in flowing lithium at 811 K. Their data are reproduced in Table 22. The mass loss of the 316 stainless steel at this temperature was linear in time and slightly less than the mass loss of 304 stainless steel. Tortorelli and Devan[53] have also published 316 stainless steel mass loss data in flowing lithium. Their data are reproduced in Table 23.

Torterelli and Devan state that the linear corrosion rates suggest that the rate controlling process is outside the stainless steel and that a significant flow velocity effect may be expected for the lithium-316 stainless steel system. They also find significant deposits from the lithium in the cooler regions of their coolant loop.

TABLE 22. MASS LOSS OF 316 STAINLESS STEEL IN FLOWING LITHIUM ACCORDING TO WHITLOW ET AL.[52]

Temperature (K)	Time (s)	Mass Loss (kg/m^2)
811	7.3×10^5	1.09×10^{-2}
811	13.5×10^6	1.36×10^{-2}
811	34.1×10^6	1.60×10^{-2}

TABLE 23. MASS LOSS OF 316 STAINLESS STEEL IN FLOWING LITHIUM ACCORDING TO TORTORELLI AND DEVAN[53]

Temperature (K)	Mass Loss Rate (10^{-10} kg/m^2 s)
873	33.
873	56.
873	36.

No data for the oxidation weight gain of 316 stainless steel in steam have been found. However, an estimate is available from oxidation weight gain data for 304 stainless steel.[3] These data show that for temperatures above 1275 K the mass gain as a function of time can be expressed as

$$m_f = \left(m_i + 2.4 \times 10^6 \exp\left(\frac{-42,428}{T}\right) \Delta t\right)^{1/2} \qquad (24)$$

where

m_f = mass gain at the end of a time span (kg/m^2 surface)

m_i = mass gain at the start of the time span (kg/m^2 surface)

T = temperature during the time span

Δt = time span (s).

Since 316 stainless steel is a modification of the basic 300-series stainless steel to reduce corrosion,[54] Equation (22) should be an upper bound for the oxidation mass gain of 316 stainless steel.

Radioactivity from activation products is a concern for reactor safety and for maintenance. Crocker and Holland[55] have published a graph showing the radioactivity of 316 stainless steel versus time after shutdown. Information taken from this graph is reproduced in Table 24 and Figure 14.

2.2 Vanadium Alloys

The vanadium alloys currently under most active consideration for fusion reactor first wall materials are V-15 Cr-5T; and VANSTAR (V-9 Cr-3.3 Fe-1.3 Zr-0.054 C).[6,24] Since these alloys are still under development, data are frequently not available. This section will review what data are available and provide estimates where related data are available. Data

TABLE 24. RADIOACTIVITY OF 316 STAINLESS STEEL AFTER SHUTDOWN ACCORDING TO CROCKER AND HOLLAND[55]

Time After Shutdown (s)	Radioactivity (Ci/kW(th))
1.00×10^{1}	1.04×10^{3}
5.04×10^{1}	9.49×10^{2}
3.29×10^{2}	8.90×10^{2}
3.37×10^{3}	7.62×10^{2}
3.24×10^{4}	6.27×10^{2}
1.63×10^{5}	5.30×10^{2}
5.07×10^{5}	4.60×10^{2}
3.20×10^{6}	3.37×10^{2}
1.09×10^{7}	2.37×10^{2}
2.30×10^{7}	1.88×10^{2}
3.99×10^{7}	1.47×10^{2}
6.92×10^{7}	1.04×10^{2}
1.41×10^{8}	5.28×10^{1}
1.77×10^{8}	3.53×10^{1}
2.52×10^{8}	1.85×10^{1}
3.84×10^{8}	8.06
5.85×10^{8}	3.25
9.50×10^{8}	1.36
1.19×10^{9}	6.27×10^{-1}
1.65×10^{9}	2.92×10^{-1}
2.06×10^{9}	1.13×10^{-1}
2.95×10^{9}	6.24×10^{-2}
4.63×10^{9}	4.23×10^{-2}
1.07×10^{10}	2.69×10^{-2}
3.02×10^{10}	1.71×10^{-2}
7.01×10^{10}	1.03×10^{-2}
1.38×10^{11}	5.39×10^{-3}
1.62×10^{11}	2.97×10^{-3}
1.73×10^{11}	1.89×10^{-3}
1.85×10^{11}	1.04×10^{-3}
2.24×10^{11}	6.27×10^{-4}
2.47×10^{11}	3.78×10^{-4}
3.65×10^{11}	2.53×10^{-4}
5.92×10^{11}	1.90×10^{-4}
1.25×10^{12}	1.63×10^{-4}

TABLE 24. (continued)

Time After Shutdown (s)	Radioactivity (Ci/kW(th))
3.29×10^{12}	1.34×10^{-4}
7.62×10^{12}	1.02×10^{-4}
1.66×10^{13}	6.49×10^{-5}
2.29×10^{13}	4.29×10^{-5}
3.37×10^{13}	1.52×10^{-5}

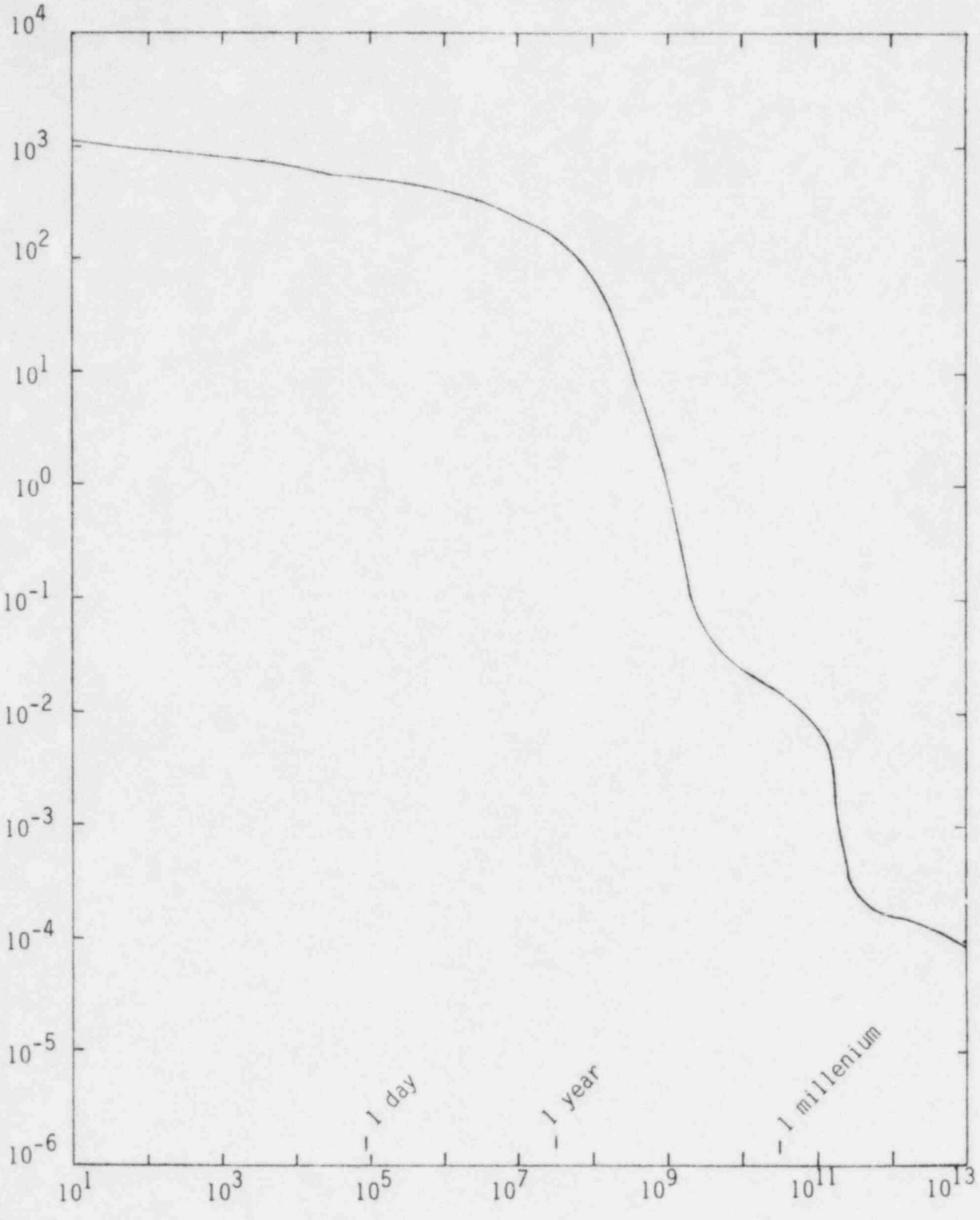

Figure 14. Radioactivity of 316 stainless steel after shutdown according to Crocker and Holland.[55]

required for tritium inventory calculations are particularily scarce and are proposed as a high priority item for measurements.

2.2.1 Thermal Properties

Virtually no thermal property data have been found for the V-15 Cr-5T; or VANSTAR 7 alloys. Therefore the specific heat capacity enthalpy, thermal conductivity, thermal expansion, emissivity and heat of fusion of these alloys will have to be estimated from related data.

Touloukian and Ho[56] have published recommended specific heats for Vanadium which are proposed as interim estimates for alloy specific heats. Their recommended values are reproduced in Table 25 and Figure 15. The values are not greatly different than those of 316 stainless steel and they can be improved if necessary by using a mass-weighted average of the specific heats of the alloy components.

Bloom[12] has published a value of thermal conductivity for V-20 Ti at 773 K, 26.0 W/mK. The best estimate aside from this number that has been found are the Vanadium thermal conductivities recommended by Touloukian and Ho[56] which are in part reproduced in Table 26. Since Touloukian and Ho state that the conductivity of vanadium is strongly affected by impurities, especially at low temperatures, the best estimate for the alloy conductivity in the temperature range 300 to 2000 K is probably obtained by using the small rate of dependence on temperature from the Vanadium conductivity with the single alloy value at 773 K:

$$K \approx 26 + (T - 773)\ 7 \times 10^{-3} \qquad (25)$$

where

K = thermal conductivity of V-15 Cr-5Ti or VANSTAR 7 (W/m•k)

T = temperature (K).

TABLE 25. SPECIFIC HEAT VALUES RECOMMENDED FOR VANADIUM BY TOULOUKIAN AND HO[56]

Temperature (K)	Specific Heat Capacity at Constant Pressure (J/kg•K)	
1	0.002 (Superconducting)	0.191 (Normal)
3	0.705 (Superconducting)	0.585 (Normal)
5	2.29 (Superconducting)	1.02 (Normal)
5.4	1.11 (Superconducting)	1.11 (Normal)
7		1.53
10		2.39
15		4.21
20		6.80
25		10.6
30		18.4
40		39.5
50		67.6
60		106
70		148
80		192
90		232
100		265
150		377
200		436
250		470
273		481
293		489
300		491
350		504
400		514
450		523
500		530
600		541
700		551
800		561
900		573
1000		590
1100		604
1200		621
1300		640

TABLE 25. (continued)

Temperature (K)	Specific Heat Capacity at Constant Pressure (J/kg•K)			
1400			661	
1500			685	
1600			711	
1700			740	
1800			772	
1900			804	
2000			844	
2100			884	
2200			926	
2202	927	(Solid)	910	(Liquid)
2400			910	
2500			910	

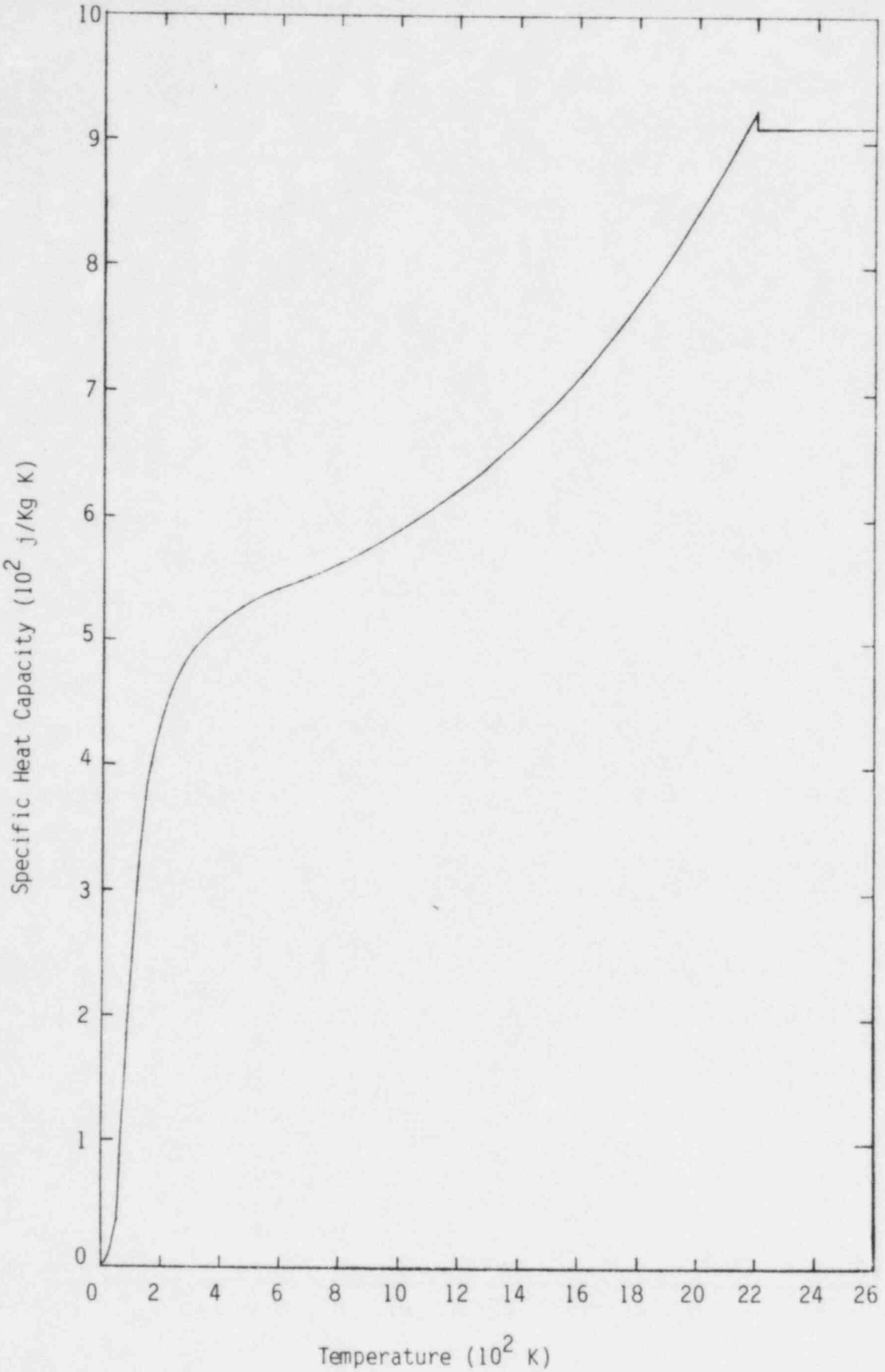

Figure 15. Specific heat values recommended for vanadium by Touloukian and Ho.[56]

TABLE 26. THERMAL CONDUCTIVITIES RECOMMENDED FOR VANADIUM BY TOULOUKIAN AND HO[56]

Temperature (K)	Thermal Conductivity (W/m•K)
300	35.1
400	35.7
500	36.3
600	37.0
700	37.7
800	38.3
900	39.0
1000	39.7
1100	40.5
1200	41.1
1300	41.8
1400	42.6
1500	43.3
1600	44.0
1700	44.7
1800	45.4
1900	46.1
2000	46.7

The thermal conductivity calculated by Equation (25) is 30% higher than that of 316 stainless steel at 773 K and about equal to that of 316 stainless steel at 1400 K.

The best available linear thermal expansion data are those for vanadium which are reviewed by Touloukian and Ho.[56] This reference uses 40 data sets to produce the following correlation for the temperature range 293 to 2000 K:

$$\rho_{th} = -0.269 + 8.971 \times 10^{-4}\ T + 5.822 \times 10^{-8}\ T^2 + 5.036 \times 10^{-11}\ T^3 \qquad (26)$$

where

ρ_{th} = thermal strain (100 m/m)

T = temperature (K).

The correlation-calculated values of strain as a function of temperature are illustrated in Figure 16. The thermal strains estimated with Equation (26) are about half those of 316 stainless steel at corresponding temperatures and the derivative of Equation (26) predicts a linear expansion rate equal to the rate given by Bloom[13] for V-20 Ti alloys at 733 K. As long as phase changes are not introduced by alloying, it is likely that Equation (26) will be satisfactory for both V-15 Cr-5 Ti and VANSTAR alloys.

The emissivity of metal surface is difficult to predict because it is a strong function of the oxidation and roughness of the surface. For polished vanadium Touloukian and Ho[56] recommend a normal total emittance which increases linearly from 0.1 near 800 K to 0.2 near 2000 K. No data have been found for oxidized vanadium alloys.

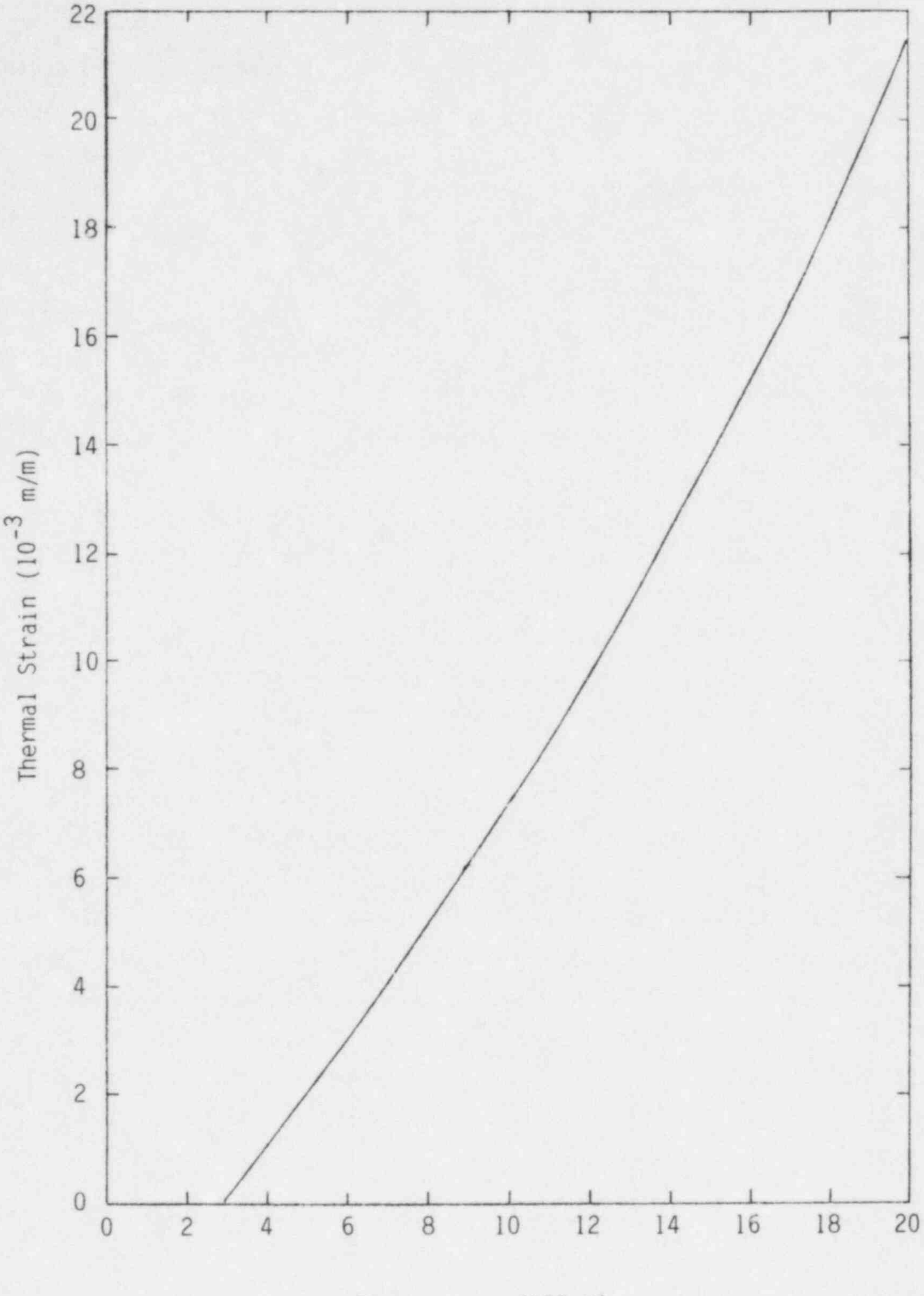

Figure 16. Values of thermal strain of vanadium recommended by Touloukian and Ho.[56]

A value of $(410 \pm 50) \times 10^3$ J/kg has been recommended by Touloukian and Ho[56] for the heat of fusion of vanadium and is suggested as an approximate value for V-15 Cr-5 Ti and VANSTAR 7 alloys. This estimate can be improved if necessary by using a mass-weighted average of the heats of fusions of the alloy components.

2.2.2 Mechanical Properties

The mechanical properties of V-15 Cr-5 Ti and VANSTAR 7 are difficult to estimate because few useful alloy data have been found and because mechanical properties are significantly affected by alloy composition and irradiation. Modeling the effects of cold work is not a problem because the preferred microstructural condition of these alloys for service above 673-773 K is in the annealed condition.[24] The existing data for elastic moduli plastic moduli or creep, failure stress, cyclic fatigue, irradiation growth or swelling and fracture toughness will be discussed. Where possible recommendations will be made for these properties.

Only two data for elastic constants have been located. The first is a result quoted by Bloom[12] for the Youngs modulus of V-20 Ti at 773 K, 1.12×10^{11} N/m^2. No reference or discussion of the measurement is given. The second set of values was obtained from ultrasonic pulse technique measurements on Vanadium by Reynolds.[57] It is presumed that Reynold's values of the Youngs modulus, shear modulus and Poisson's ratio, 1.27×10^{11} N/m^2, 4.66×10^{10} N/m^2, and 0.36, were at room temperature. Since no other data have been found, a constant value of 0.36 for the Poisson's ratio is recommended along with a linear fit to the two measurements of Youngs modulus:

$$E = 1.37 \times 10^{11} - 3.2 \times 10^7 \, T \qquad (27)$$

where

E = Youngs modulus for Vanadium alloys (N/m^2)

T = temperature (K).

The shear modulus at any temperature can be obtained from the Poisson's ratio, Equation (27) and Equation (1).

Plastic deformation data for VANSTAR 7 have been reported by Korth and Schmunk.[58] Unfortunately, these authors include only the 0.2% offset yield data at 673 shown in Table 27. The approach devised for 316 stainless steel to convert Yield and Ultimate strength data to usable stress-strain-strain rate correlations can not be used. The data of Tanaka, Bloom and Horak[59] for the V-20 Ti alloy are therefore recommended as an approximation. These data are reproduced in Table 28 and do include all of the needed parameters. Some caution is required with this approach because mechanical properties can be significantly affected by alloy composition. For instance, the ultimate strength of pure vanadium is much less than that of V-20 Ti.[60]

No data for very slow strain rates (creep) have been found for vanadium alloys or the element. Thus, it is not possible to recommend models for this property.

No data have been found for failure stresses either, but it is possible to recommend an interim approach to the problem because Tanaka et al.[59] and Gold and Harrod[61] have published total elongations at failure. Use of a stress-strain-strain rate law with these elongations (0.19 for unirradiated alloy and irradiated alloy at 973 but 0.066 for alloy at 673 K) will provide failure stresses.

TABLE 27. VANSTAR 7 PLASTIC DEFORMATION DATA FROM KORTH AND SCHMUNK[58]

Temperature (K)	Neutron Fluence (10^{26} n/m^2)	Yield Strength (10^6 Pa)
673	0.022	619
673	0	213
673	0	207
673	0	199
673	0	219

TABLE 28. V-20 Ti PLASTIC DEFORMATION DATA FROM TANAKA ET AL.[59]

Temperature (K)	Neutron Fluence (10^{26} n/m^2)	Yield Strength (10^6 Pa)	Ultimate Strength (10^6 Pa)	Uniform Elongation (m/m)
298	0	546	661	0.120
673	0	387	588	0.114
673	3	677	817	0.048
798	0	400	668	0.130
848	0	407	681	0.141
848	3[a]	376	603	0.106
898	0	384	619	0.123
973	0	345	499	0.134
973	3	385	468	0.141

---

[a] This sample was irradiated in a sodium environment.

Data or recommended values for cyclic fatigue of Vanadium or its alloys have been published in three references.[12,58,62] However, two of these references published only measurements of strain or stress range versus cycles to failure and will therefore not be used because of concern that such data measure sample size as well as a property of the material. Bloom[12] has published recommended values of crack growth rates in annealed vanadium at 300 K. His recommendation is reproduced in Figure 17. The end points of the line are (6.00×10^6 Pa•m$^{1/2}$, 1.16×10^{-9} m/cycle) and (1.45×10^7 Pa•m$^{1/2}$, 3.68×10^{-8} m/cycle).

No data have been found for the irradiation growth, swelling or fracture toughness of vanadium or its alloys.

2.2.3 Electromagnetic Properties

No data have been found for the electrical resistivity or magnetic permeability of vanadium or its alloys.

2.2.4 Physical/Chemical Properties

The properties that will be discussed in this section are density, melting temperature, hydrogen isotope solubility, hydrogen isotope permeability, hydrogen isotope diffusion rates, hydrogen isotope reflection coefficients, hydrogen isotope trapping coefficient data, hydrogen isotope molecular recombination rates, hydrogen isotope sputtering yields, corrosion by lithium, corrosion by water, and activation product deay times. In most cases no data have been located and no better estimate than the corresponding properties for stainless steel are available.

No measurements of the density and melting temperaures of V-15 Cr-5 Ti or VANSTAR 7 are available but these properties can be estimated from the corresponding properties for pure vanadium,[61] 6100 kg/m^3 and 2160 K. The density is 20% less than that of 316 stainless steel and the melting

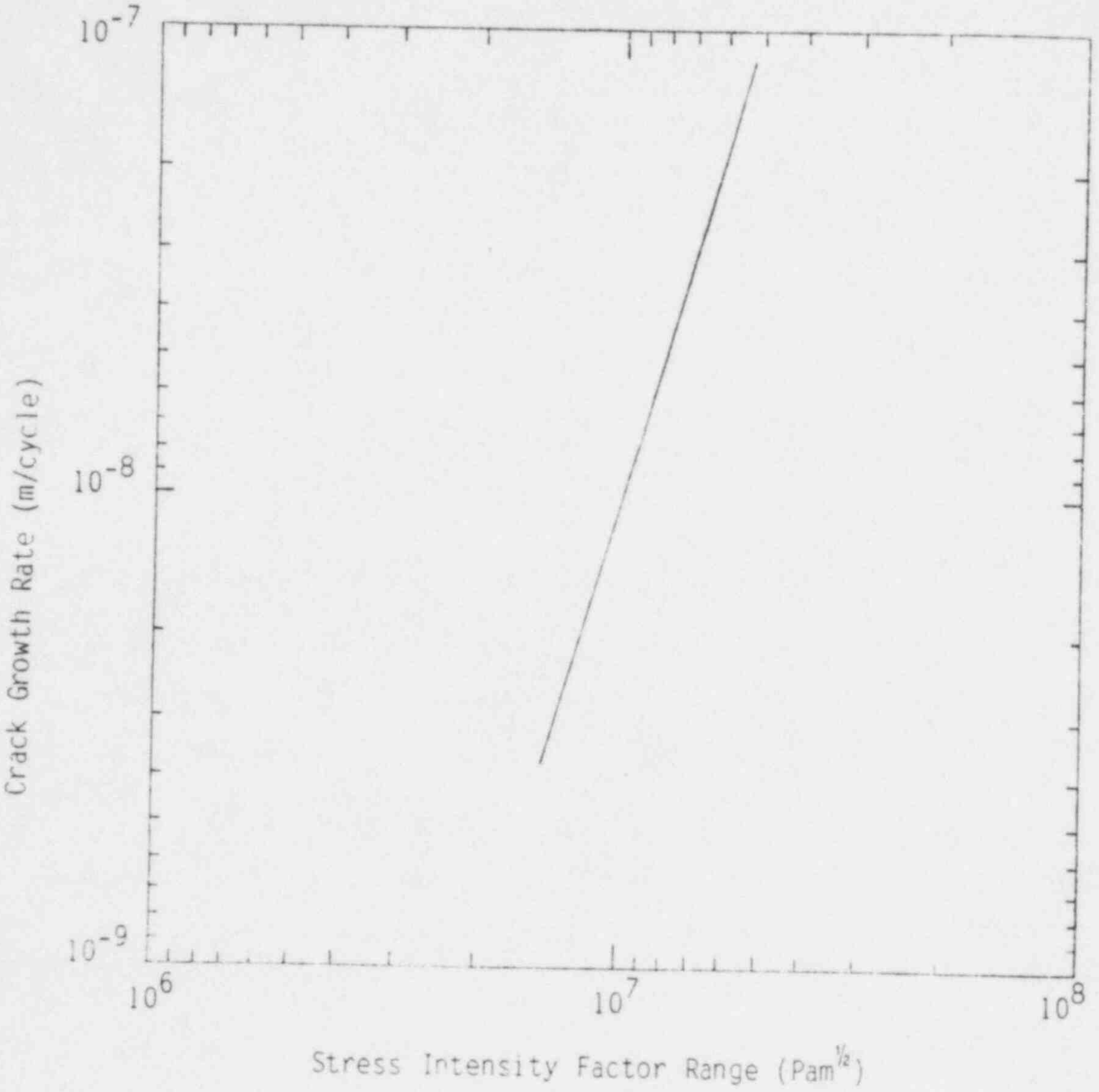

Figure 17. Values for crack growth rate in vanadium at room temperature recommended by Bloom[12].

temperature is 500 K higher than that of stainless steel. It should be noted that the melting temperature of the vanadium alloys is likely to be lower than that of the pure element.

Although no alloy data are available, there is some available information about hydrogen isotope permeability, diffusion rates and solubility in pure vanadium. Figure 1 of Maroni and Van Deventer[31] provides an expression for the solubility

$$S = 2.6 \exp\left(\frac{3640}{T}\right)\sqrt{P} \tag{28}$$

where

S = amount of hydrogen dissolved (atomic parts per million)

P = pressure (Pa)

T = temperature (K).

The solubility in pure vanadium is about three orders of magnitude larger than that in 316 stainless steel and increases with decreasing temperature because the vanadium forms hydrides.

Both Maroni and Van Deventer[31] and Namba et al.[63] discuss the permeation of hydrogen through vanadium. Maroni and Van Deventer (Figure 2 in Reference 31) suggests a permeability determined by

$$\phi = 131 \exp\left(\frac{-7120}{T}\right)\frac{\Delta(\sqrt{P})}{X} \tag{29}$$

where

ϕ = flux of hydrogen through a vanadium plate (cm^3 of hydrogen at STP/m^2 s)

X = plate thickness (m)

$\Delta(\sqrt{P})$ = difference of the square root of pressure across the plate ($\sqrt{10^3}$ Pa).

Namba et al. report data which suggest that Equation (29) is not valid for low pressures (less than about 20 Pa). They also report that a vanadium oxide surface layer acted as a barrier to hydrogen permeation.

Unfortunately no data have been found for hydrogen isotope diffusion rates, hydrogen isotope reflection coefficients, hydrogen isotope trapping coefficients, hydrogen isotope molecular recombination rates, hydrogen isotope sputtering yields, or vanadium alloy corrosion by water.

A curve estimating the radioactivity of vanadium-titanium alloys as a function of time after shutdown has been published by Crocker and Holland.[55] This information is reproduced in Table 29 and Figure 18. Comparison with the analogous figure for 316 stainless steel, Figure 14, shows that with the exception of the first 50 seconds after shutdown vanadium-titanium alloys are far less radioactive than 316 stainless steel.

2.3 Ferritic/Martensitic Steel Alloys

A number of ferritic/martensitic steel alloys are being considered for first wall applications in fusion reactors because these alloys have demonstrated very little swelling under fast neutron bombardment[24,63,64] and may be resistent to neutron radiation effects for several properties. The possible gains from the minimal swelling and other favorable properties may increase the first wall lifetime enough to outwiegh the disadvantages of using a ferro-magnetic alloy. The ferritic/martensitic alloys under most active consideration are a modified 9 Cr-1 Mo[a] steel developed for LMFBR

---

[a] The 9 and 1 designate 9% chromium and 1% molybdenum, respectively.

TABLE 29. RADIOACTIVITY OF VANADIUM-TITANIUM ALLOY AFTER SHUTDOWN ACCORDING TO CROCKER AND HOLLAND[55]

Time After Shutdown (s)	Radioactivity (Ci/kW(th))
1.00×10^1	1.31×10^3
1.91×10^1	1.15×10^3
5.04×10^1	9.49×10^2
9.02×10^1	7.59×10^2
1.84×10^2	5.37×10^2
4.12×10^2	3.50×10^2
9.25×10^2	1.69×10^2
1.46×10^3	1.06×10^2
2.87×10^3	7.30×10^1
8.08×10^3	5.63×10^1
2.13×10^4	5.56×10^1
5.27×10^4	5.14×10^1
1.18×10^5	4.23×10^1
5.59×10^5	1.95×10^1
3.20×10^6	7.08
2.71×10^7	2.20
1.05×10^8	8.67×10^{-1}
2.01×10^8	4.25×10^{-1}
2.78×10^8	1.90×10^{-1}
3.06×10^8	4.82×10^{-2}
3.97×10^8	1.72×10^{-3}
5.31×10^8	1.82×10^{-5}
6.24×10^8	1.40×10^{-6}

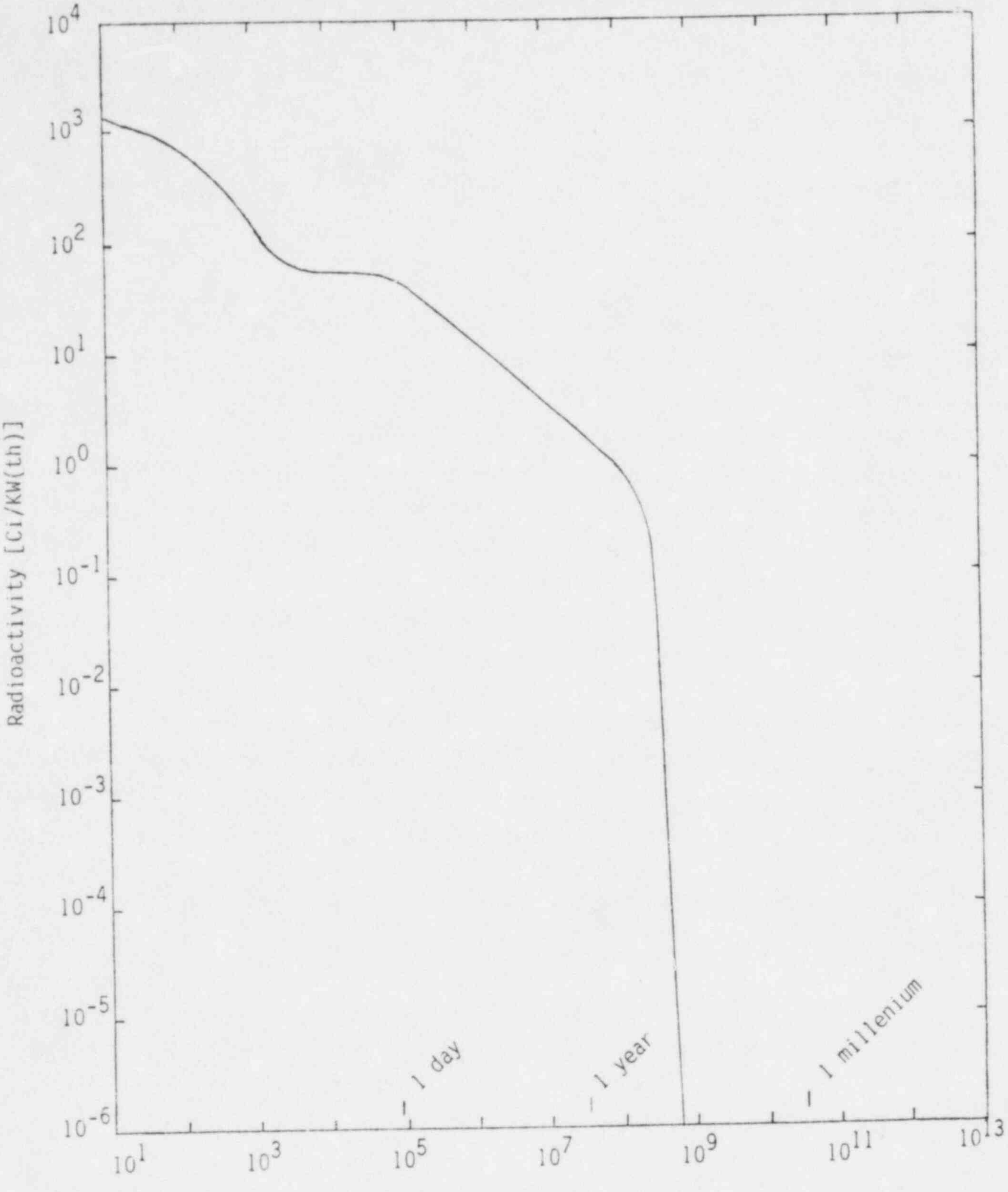

Figure 18. Radioactivity of vanadium-titanium alloys according to Crocker and Holland.[55]

reactors and a commercial steel alloy with 12 Cr-1 Mo-0.3 V which is designated alloy HT-9. Unfortunately, many of the data which do exist for these alloys have not yet been published.[64] Properties will therefore frequently have to be estimated from data obtained from similar steel alloys.

2.3.1 Thermal Properties

No thermal property data have been found for 9 Cr-1 Mo steel or HT-9. However, Peckner and Bernstein[1] have published recommended properties for 403 and 410 stainless steels and these steels are similar to 9 Cr-1 Mo and HT-9. Chapter 1 of Peckner and Bernstein gives the composition of 403 and 410 stainless steel as 0.15% maximum carbon, 1% mangenese and 11.5 to 13% chromium and points out that they are martensitic steels. The corresponding composition and martensitic structure of the 403 and 410 steels should make their thermal properties very similar to the thermal properties of 9 Cr-1 Mo and HT-9 so the 403 and 410 stainless steel properties are recommended as an interim estimate for the 9 Cr-1 Mo and HT-9 properties.

Values of the specific heat capacity of 410 stainless steel taken from a curve in Peckner and Bernstein[1] are displayed in Table 30 and Figure 19. The specific heat capacity of 410 stainless steel is about the same as the specific heat capacity of 316 stainless steel in the temperature range 250 to 700 K but for temperatures in the range 700 to 1350 K the specific heat capacity of 410 stainless steel is significantly larger than that of 316 stainless steel.

Thermal conductivities reported by Peckner and Bernstein[1] for 403 and 410 stainless steel are reproduced in Table 31 and Figure 20. The conductivities for these two steels are similar and nearly twice the thermal conductivity of 316 stainless steel.

Table 32 and Figure 21 illustrate the average thermal expansion coefficients for 403 and 410 stainless steel between 273 K and the temperature indicated. The two alloys differ by no more than five percent over the entire range of temperatures studied. When the average expansion

TABLE 30. SPECIFIC HEAT CAPACITIES OF 410 STAINLESS STEEL FROM CURVE OF PECKNER AND BERNSTEIN[1]

Temperature (K)	Specific Heat Capacity (J/kg•K)
255	457
311	463
342	467
386	475
404	480
443	490
456	494
502	510
516	516
543	531
563	540
592	556
625	576
659	599
691	623
754	674
816	726
875	779
928	831
982	882
1009	908
1065	693
1119	815
1177	655
1220	664
1237	668
1288	677
1307	680
1364	686

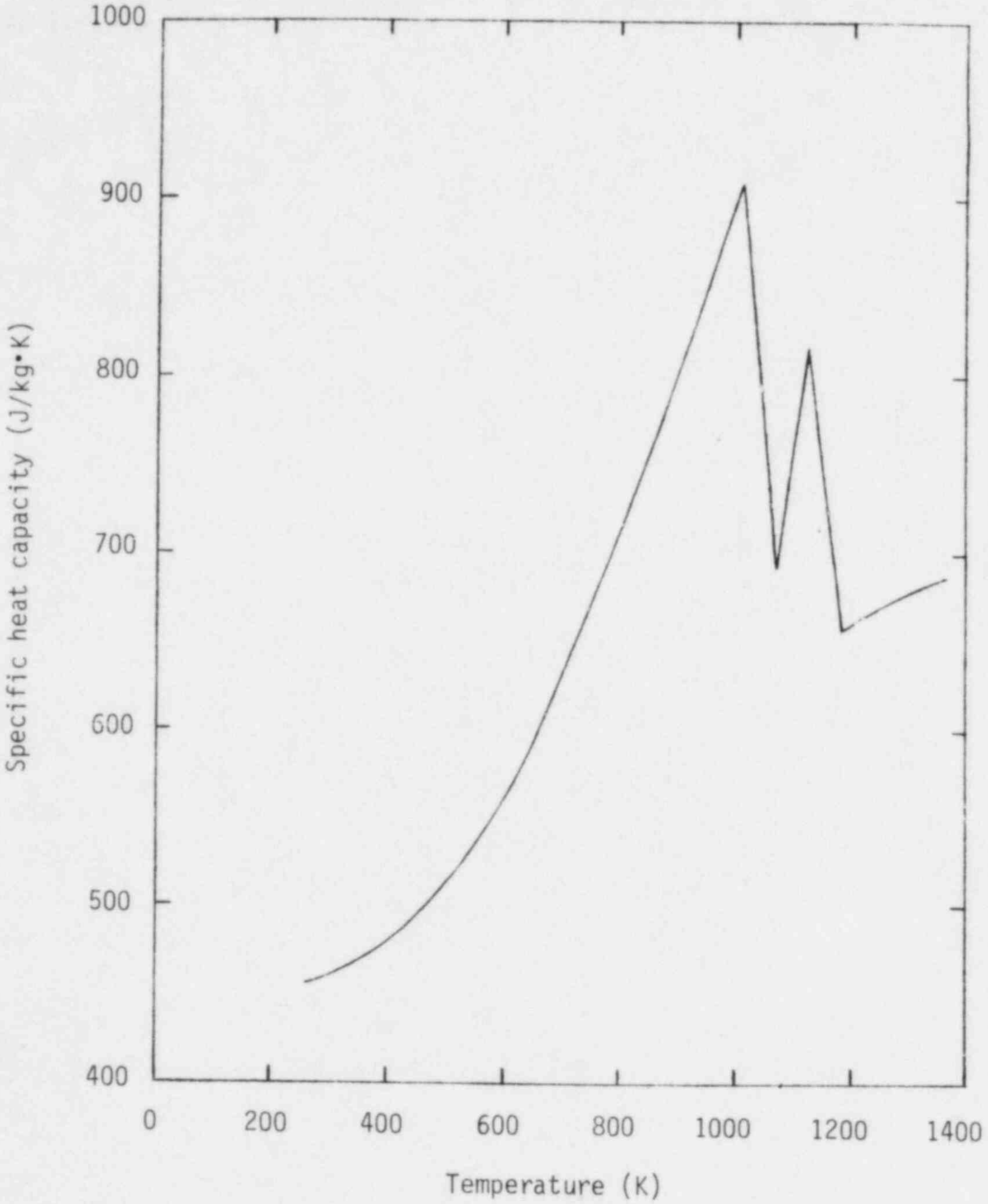

Figure 19. Specific heat capacity of 410 stainless steel given by Peckner and Bernstein[1].

TABLE 31. THERMAL CONDUCTIVITIES OF 403 AND 410 STAINLESS STEEL FROM CURVES OF PECKNER AND BERNSTEIN[1]

Temperature (K)	Thermal Conductivity (W/m•K)	Steel Type
380	22.5	403
497	24.3	403
621	26.4	403
742	28.4	403
380	24.8	410
489	26.0	410
615	27.2	410
768	28.8	410

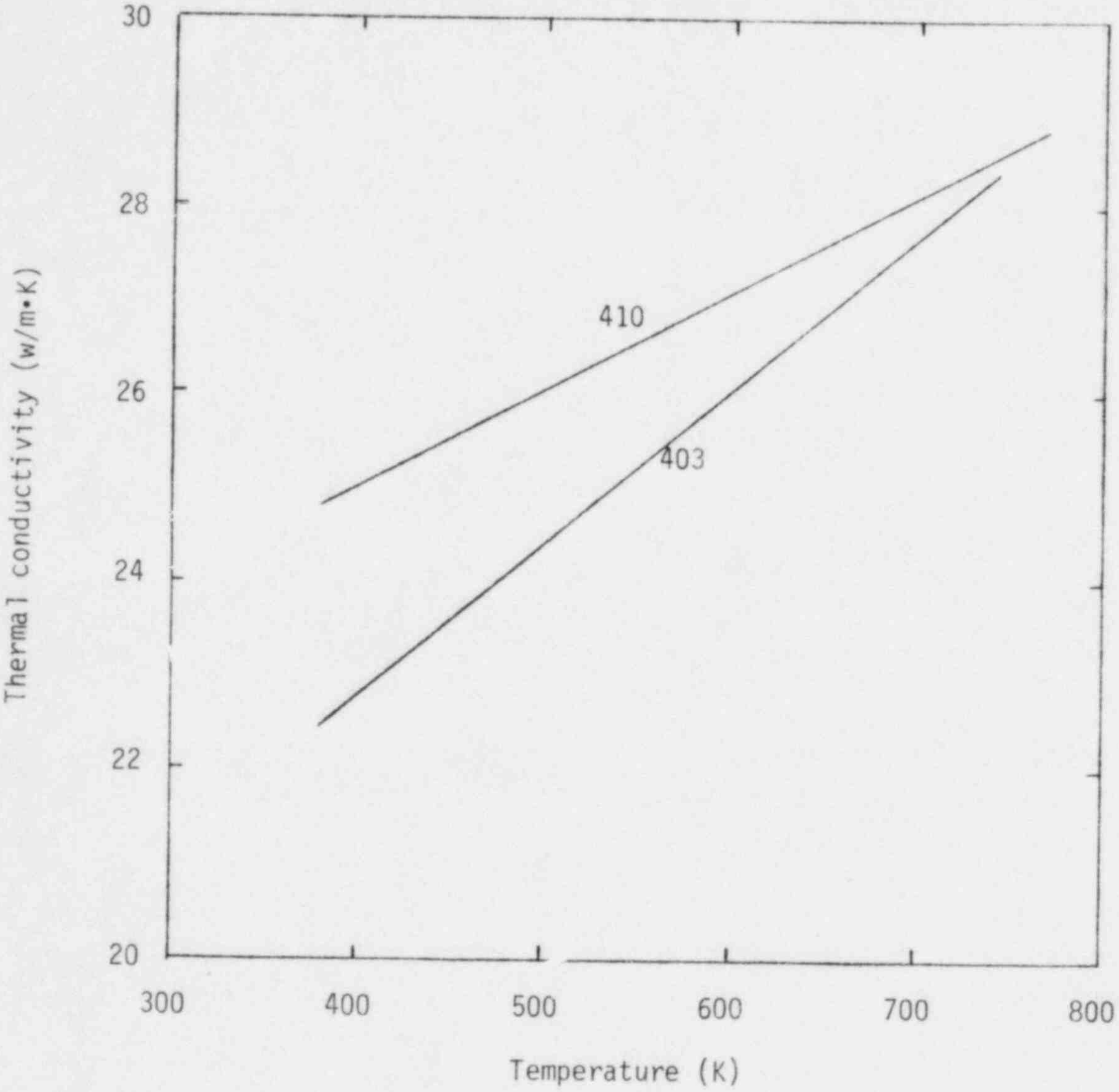

Figure 20. Thermal conductivity of 403 and 410 stainless steel according to Peckner and Bernstein[1].

TABLE 32. AVERAGE THERMAL EXPANSION COEFFICIENTS FOR 403 AND 410 STAINLESS STEEL FROM CURVES PUBLISHED BY PECKNER AND BERNSTEIN[1]

Upper Temperature (K)	Average Thermal Expansion Coefficient (10^{-6} m/m•K)	Steel Type
410	9.93	403
449	9.95	403
491	9.97	403
519	10.00	403
551	10.04	403
584	10.10	403
605	10.16	403
627	10.25	403
643	10.33	403
660	10.45	403
677	10.57	403
709	10.76	403
736	10.96	403
768	11.17	403
790	11.30	403
806	11.38	403
828	11.48	403
842	11.53	403
865	11.60	403
891	11.64	403
909	11.67	403
925	11.68	403
389	10.02	410
410	10.09	410
459	10.24	410
505	10.38	410
550	10.53	410
594	10.68	410
638	10.82	410
677	10.97	410
714	11.09	410
744	11.21	410
782	11.34	410
828	11.49	410
867	11.60	410

TABLE 32. (continued)

Upper Temperature (K)	Average Thermal Expansion Coefficient (10^{-6} m/m•K)	Steel Type
909	11.76	410
953	11.91	410
997	12.07	410
1036	12.21	410
1084	12.39	410
1122	12.56	410
1146	12.68	410
1168	12.81	410
1188	12.92	410
1208	13.04	410
1222	13.16	410
1238	13.26	410
1251	13.39	410
1261	13.50	410
1269	13.63	410

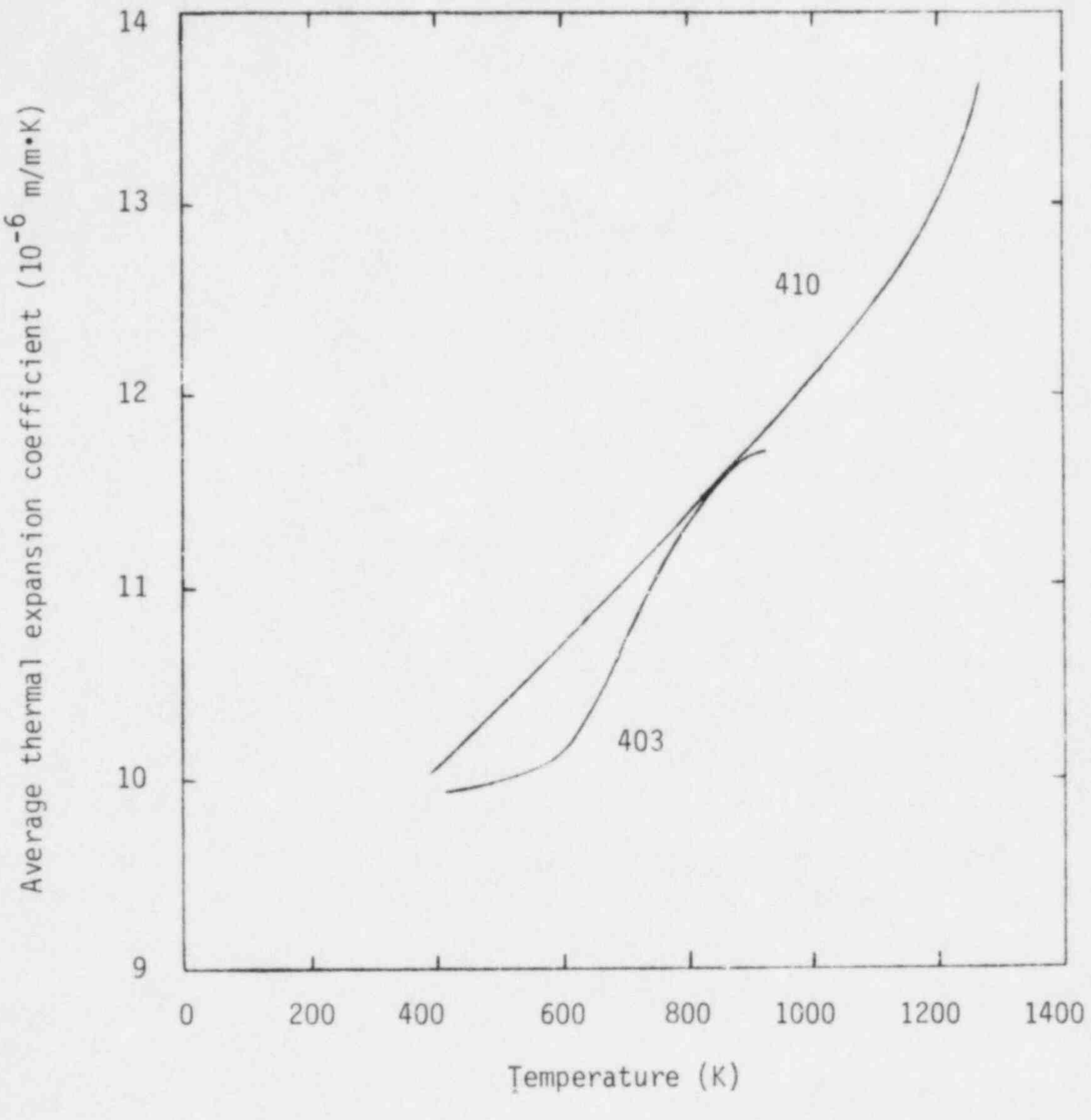

Figure 21. Average thermal expansion coefficients for 403 and 410 stainless steel between 283.15 K and the indicated temperature according to Peckner and Bernstein[1].

coefficients are converted to thermal strains between 273 K and a given temperature, the difference between 403 and 410 is seen to be negligible compared to the total strain. These results are shown in Table 33 and Figure 22. Figure 22 and Figure 4 show that the change in thermal strain of 316 stainless steel about 273 K is about 20% greater than that of 403 or 410 stainless steel.

No data have been found for the emissivity of ferritic/martensitic steel alloys. Estimated values of this parameter range from 0.1 for a clean surface to 0.8 for an oxidized surface.

Data for the heats of fusion and vaporization have not been found either. Until such data are available, the corresponding values for 316 stainless steel, 2.68×10^5 J/kg and 7.41×10^5 J/kg, are recommended as estimates.

2.3.2 Mechanical Properties

The mechanical properties of 9 Cr-1 Mo and HT-9 steel are only partly available so some data from the similar alloys 403 and 410 stainless steel are used to provide estimates for mechanical properties where better data are not available. The technique of using similar alloys to estimate mechanical properties is less reliable than it is for the thermal properties because of the sensitivity of many mechanical properties to relatively small changes in composition and structure. In addition, there are few data to quantify the effects of heat treatments, cold work and irradiation. For ferritic/martensitic steel alloys, the heat treatment effects are likely to be especially important.[1]

The best data that have been found to estimate elastic moduli are curves of recommended Young's moduli for 410 stainless steel published by Peckner and Bernstein.[1] Table 34 and Figure 23 are reproductions of these curves. No data for the shear modulus or Poisson's ratio have been found. The best recommendation that can be made for these properties is based on the observation that the Young's modulus of 410 stainless steel is about

TABLE 33. THERMAL STRAINS CALCULATED FROM AVERAGE THERMAL EXPANSION COEFFICIENT CURVES OF PECKNER AND BERNSTEIN[1]

Upper Temperature (K)	Thermal Strain (10^{-3} m/m)	Steel Type
273.15	0	403
410	1.36	403
449	1.75	403
491	2.17	403
519	2.46	403
551	2.79	403
584	3.14	403
605	3.37	403
627	3.63	403
643	3.82	403
660	4.04	403
677	4.27	403
709	4.69	403
736	5.07	403
768	5.53	403
790	5.84	403
806	6.06	403
828	6.37	403
842	6.56	403
865	6.87	403
891	7.19	403
909	7.42	403
925	7.61	403
389	1.16	410
410	1.38	410
459	1.90	410
505	2.41	410
550	2.92	410
594	3.43	410
638	3.95	410
677	4.43	410
714	4.89	410
744	5.28	410
782	5.77	410
828	6.38	410

TABLE 33. (continued)

Upper Temperature (K)	Thermal Strain (10^{-3} m/m)	Steel Type
867	6.89	410
909	7.48	410
953	8.10	410
997	8.74	410
1036	9.31	410
1084	10.05	410
1122	10.66	410
1146	11.07	410
1168	11.46	410
1188	11.82	410
1208	12.19	410
1222	12.49	410
1238	12.79	410
1251	13.09	410
1261	13.34	410
1269	13.57	410

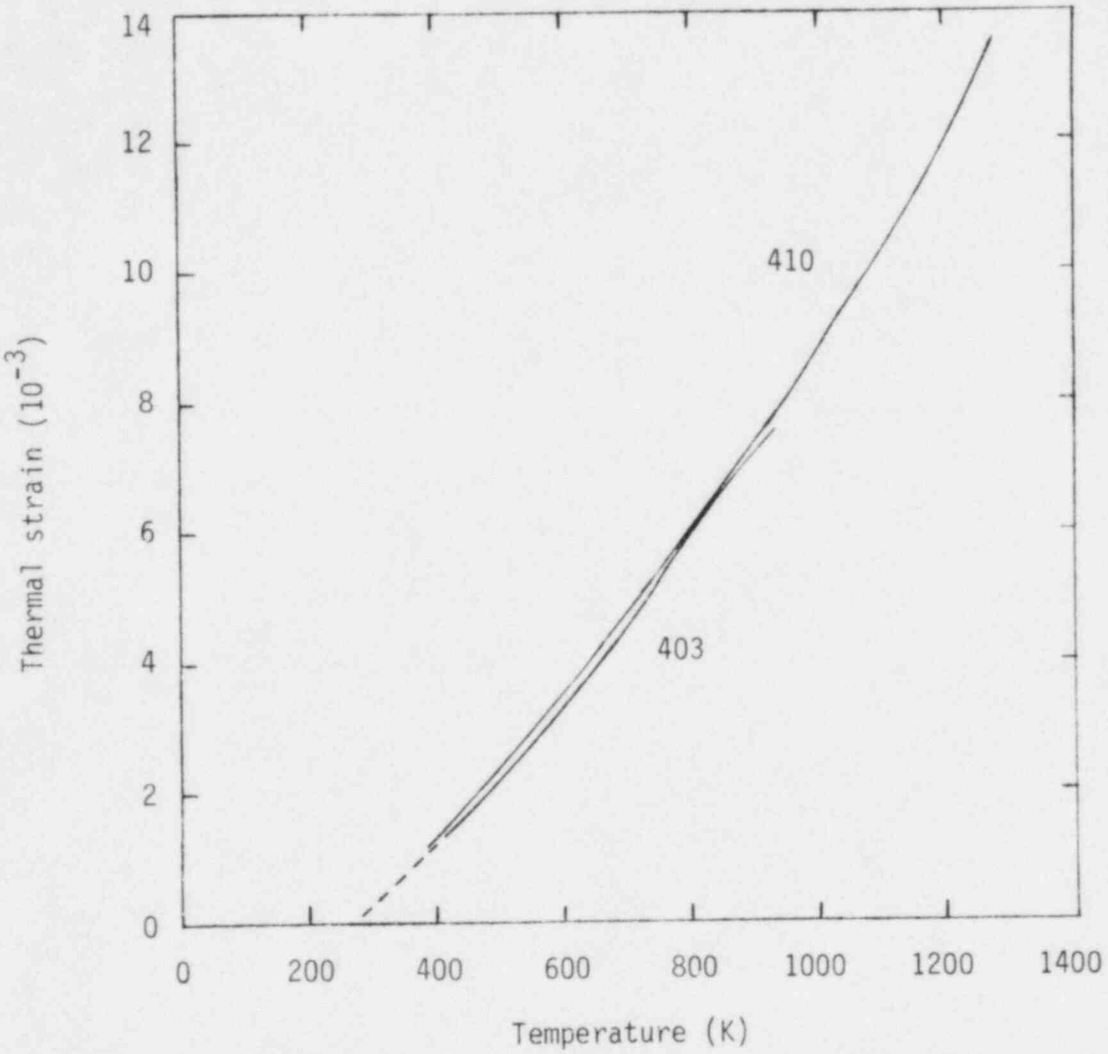

Figure 22. Thermal strains of 403 and 410 stainless steel referenced to 273.15 K obtained from the average thermal expansion coefficients given by Peckner and Bernstein[1].

TABLE 34. 410 STAINLESS STEEL ELASTIC MODULUS ACCORDING TO PECKNER AND BERNSTEIN[1]

Temperature (K)	Young's Modulus (10^9 N/m^2)
319	220
397	214
491	207
575	199
667	191
752	183
837	175
914	167
992	159
1031	155

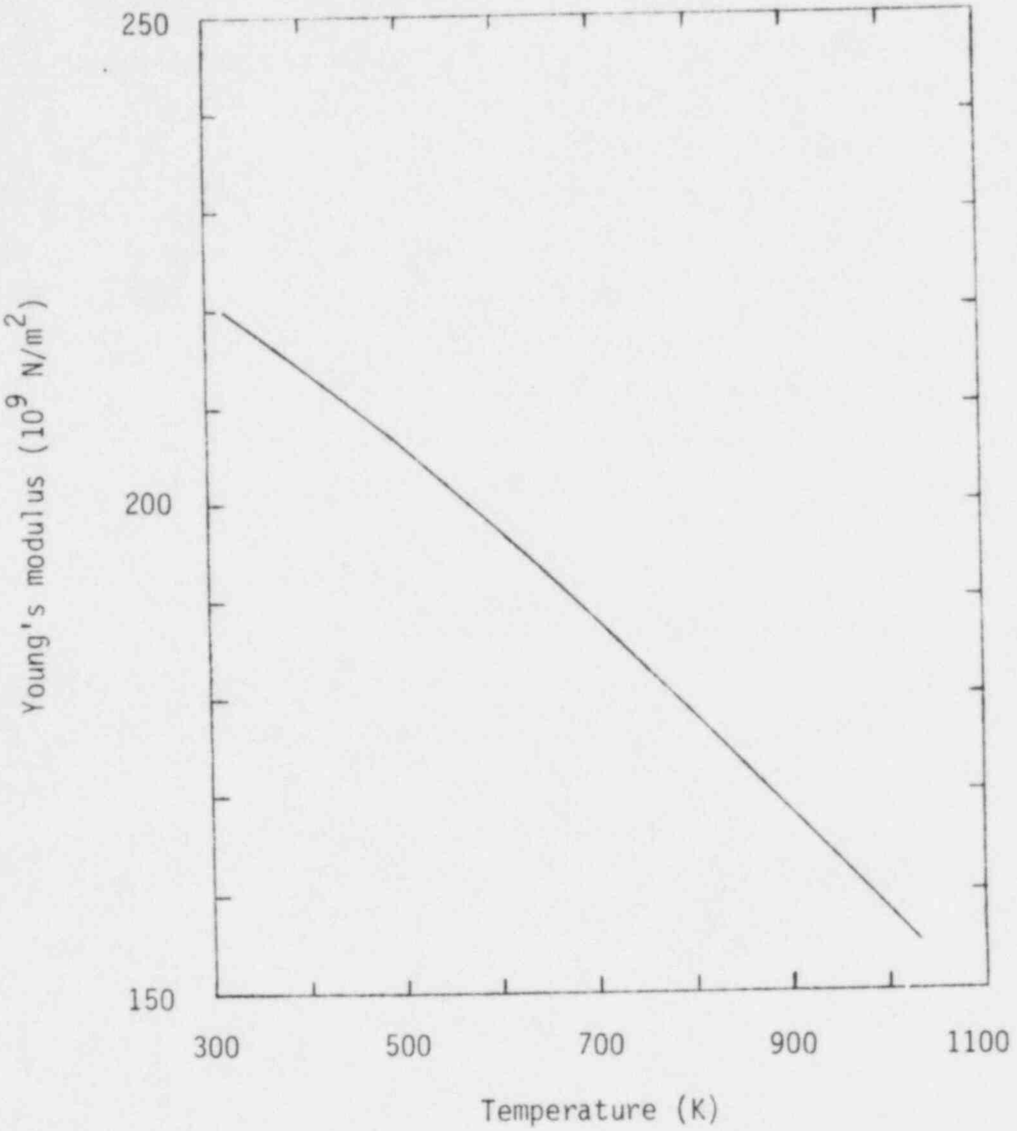

Figure 23. Young's modulus of 410 stainless steel according to Peckner and Bernstein[1].

1.1 times the Young's modulus of 316 stainless steel given in Table 5. The shear moduli for 410 stainless steel and the other ferritic/martensitic steels should also be approximately 1.1 times the shear moduli in Table 5 and the Poisson's ratio should be similar to that calculated for 316 stainless steel with Equation (1).

The available plastic deformation data are reproduced in Tables 35 and 36. Figure 24 is a plot of the yield strengths versus temperature and Figure 25 shows the available ultimate strength information from these tables. The change in yield and ultimate strength with increasing temperature shown in the figures is characteristic of most metals. The 410 stainless steel data also illustrate the great change in yield and ultimate strength with heat treatment. Unfortunately, the only data for HT-9 steel[64] do not include information about the heat treatment of the alloy so considerable uncertainty must remain about its plastic deformation properties. Additional uncertainty is introduced by the complete lack of data on the effect of neutron irradiation.

Since the strength coefficient and strain hardening exponent are not a strong function of the uniform elongation, it should be possible to use the technique discussed for 316 stainless steel to deduce a stress versus strain correlation for low temperatures (less than 700 K) by assuming that the uniform elongation is approximately equal to the total elongation given in Table 35. Valid equations of state for higher temperatures will require data on the relation between strain rate and stress.

The available data for creep (strain rates less than about 10^{-6}/s) are given in Tables 37 and 38. These data are not sufficient to construct models for creep. The three data offered for HT-9 steel by Paxton et al.[65] are all at one temperature and fluence so there is no way to determine the effect of temperature or fluence variations. Also, there are no measurements of strain versus time so that primary and secondary creep can be modeled. The 403 and 410 stainless steel data from Peckner and Bernstein[1] may be useful to estimate the effect of temperature on thermal creep, but

TABLE 35. HT-9 PLASTIC DEFORMATION DATA FROM RAWLS ET AL.[64]

Temperature (K)	Yield Strength (10^6 Pa)	Ultimate Strength (10^6 Pa)	Elongation (m/m)
312	530	759	0.265
339	530	749	0.250
376	530	735	0.226
406	529	725	0.214
443	525	709	0.199
465	524	701	0.191
494	520	690	0.185
523	514	680	0.179
546	510	672	0.178
581	499	657	0.179
619	488	644	0.180
642	477	633	0.184
664	471	626	0.188
683	461	612	0.190
700	451	597	0.192
720	444	580	0.199
738	432	557	0.201
756	421	533	0.211
773	409	508	0.218
792	392	483	0.228
812	374	448	0.238
832	353	414	0.254
851	329	379	0.263
869	312	352	0.278
890	283	314	0.298
904	259	283	0.316
923	236	256	0.338

TABLE 36. 410 STAINLESS STEEL PLASTIC DEFORMATION PROPERTIES FROM PECKNER AND BERNSTEIN[1]

Temperature (K)	Yield Strength (10^6 Pa)	Ultimate Strength (10^6 Pa)	Material Condition
294	275.8	517.1	Annealed
294	999.8	1068.7	Heat-treated
477	930.8	1034.3	Heat-treated
589	861.9	999.8	Heat-treated
700	792.9	896.4	Heat-treated
811	655	689.5	Heat-treated
922	275.8	310.3	Heat-treated
1033	--	124.1	Heat-treated
1144	--	103.4	Heat-treated

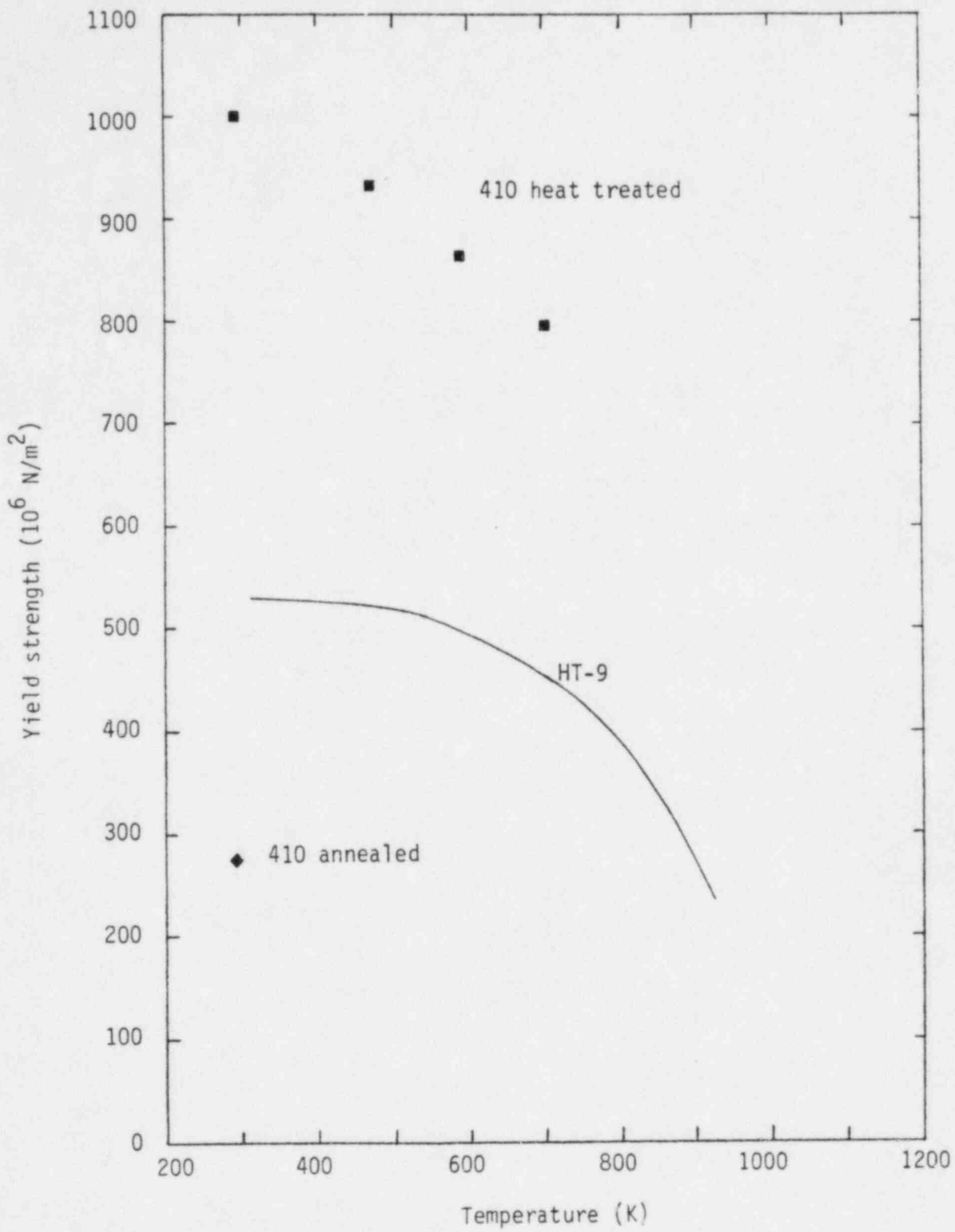

Figure 24. Yield strength of HT-9 steel, annealed 410 stainless steel, and heat treated 410 stainless steel according to Rawls et al[64] and Peckner and Bernstein[1].

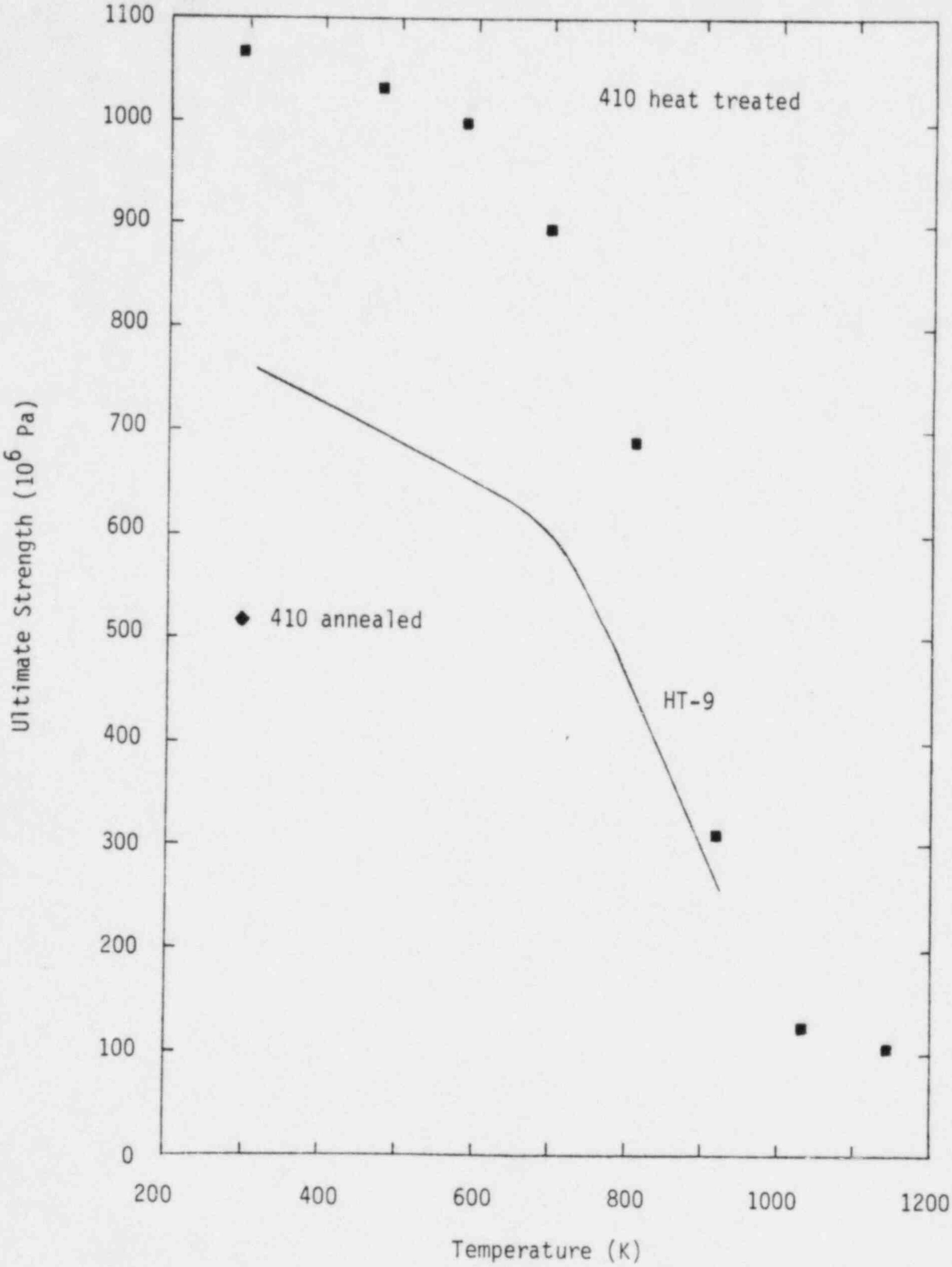

Figure 25. Ultimate strength of HT-9 steel, annealed 410 stainless steel, and heat treated 410 stainless steel according to Rawls et al[64] and Peckner and Bernstein[1].

TABLE 37. HT-9 STEEL CREEP DATA FROM PAXTON ET AL.[65]

Temperature (K)	Neutron Fluence (10^{26} n/m^2)	Hoop Strain (10^6 Pa)	Diametral Strain (10^{-4} m/m)
818	2	27.5	2.69
818	2	55.7	8.65
818	2	110.2	23.2

TABLE 38. 403 AND 410 STAINLESS STEEL CREEP DATA FROM PECKNER AND BERNSTEIN[1]

Temperature (K)	Neutron Fluence (10^{26} n/m^2)	Stress (10^6 Pa)	Strain (m/m)	Time (hours)	Steel Type
811	0	75.8	0.01	10,000	403
866	0	31	0.01	10,000	403
922	0	13.8	0.01	10,000	403
977	0	9.7	0.01	10,000	403
811	0	79.3	0.01	10,000	410
866	0	29.6	0.01	10,000	410
922	0	13.8	0.01	10,000	410
977	0	10.3	0.01	10,000	410

the samples were unirradiated so they offer no information about irradiation-induced creep, which is frequently much larger than thermal creep. If creep strains turn out to be an important consideration, many more experiments will be required to characterize the ferritic/martensitic steel alloys.

No data for true failure stress of ferritic/martensitic steels have been found. The best available estimate is the product of the ultimate strength and the square of one plus the elongation shown in Table 35. This product is a lower bound to the true failure stress because it assumes the strain at failure is completely uniform and thus that the cross-sectional area is reduced by a factor of the square of one plus the elongation everywhere in the deforming region.

Data for cyclic fatigue descriptions are almost nonexistent. Peckner and Bernstein[1] present some data for 410 stainless steel in their Figure 21 which show 0.1 to 10 million cycles to failure for bending stresses near 4×10^8 Pa. Since these data do not measure crack growth rates, the existing 316 stainless steel crack growth data are recommended as a first approximation to ferritic/martensitic steel cyclic fatigue information. The approximation is probably very poor because the differing crystaline structure of the two steels is likely to be very significant for crack initiation and growth.

As has been mentioned in previous sections, irradiation growth and swelling are typically not considered to be materials properties and are therefore not discussed in detail. Some data for ferritic/martensitic steels are discussed in Gold et al.,[24] Rawls et al.,[64] and Little and Stow.[63] These authors find that void swelling is much less in ferritic/martensite steels like HT-9 than it is in 316 stainless steel with 20% cold work.

No fracture toughness data have been found for the ferritic/martensitic steels. The most relevant data are measurements of energy absorbed for 410 stainless steel reported in Table 8 and Figure 20 of Peckner and

Bernstein.[1] The energy absorbed is reported to vary from 20 joules for material tempered near 750 K to 145 joules for annealed 410 stainless steel.

2.3.3 Electromagnetic Properties

The magnetic permeability of a 12 Cr-1 Mo sample of steel has been reported to be 1.0 to 1.6 for a saturated sample[64] and 700 to 1000 for unsaturated samples of 403 and 410 stainless steels at room temperature.[1]

Although no data have been found for the electrical resistivity of HT-9 steel, the curve for 410 stainless steel given by Peckner and Bernstein[1] should provide a reasonable first estimate. This curve is reproduced in Figure 26 and Table 39. It predicts a resistivity which is only 0.75 that predicted for 316 stainless steel by Equation (15) at room temperature but increases to 0.95 of the value from the equation at higher temperatures. No data for the resistivity of irradiated ferritic/martensitic steels have been found.

2.3.4 Physical/Chemical Properties

Many of the physical/chemical properties of the ferritic/martensitic steels are not yet available and must be estimated from similar data. Peckner and Bernstein[1] report a density of 7700 kg/m^3 at 300 K and a melting range of 1756 to 1805 K for both 403 and 410 stainless steel. The density is some 300 kg/m^3 less than that of 316 stainless steel and the melting temperatures are about 100 K higher than those of 316 stainless steel.

Although some initial results indicating that hydrogen trapping problems may be minimal have been claimed,[24] no specific data for hydrogen isotope permeability, diffusion rates, solubility, reflection coefficients, trapping, molecular recombination rates or sputtering rates have yet been found. For all of these properties except diffusion rates, the values for 316 stainless steel are recommended as a first approximation.

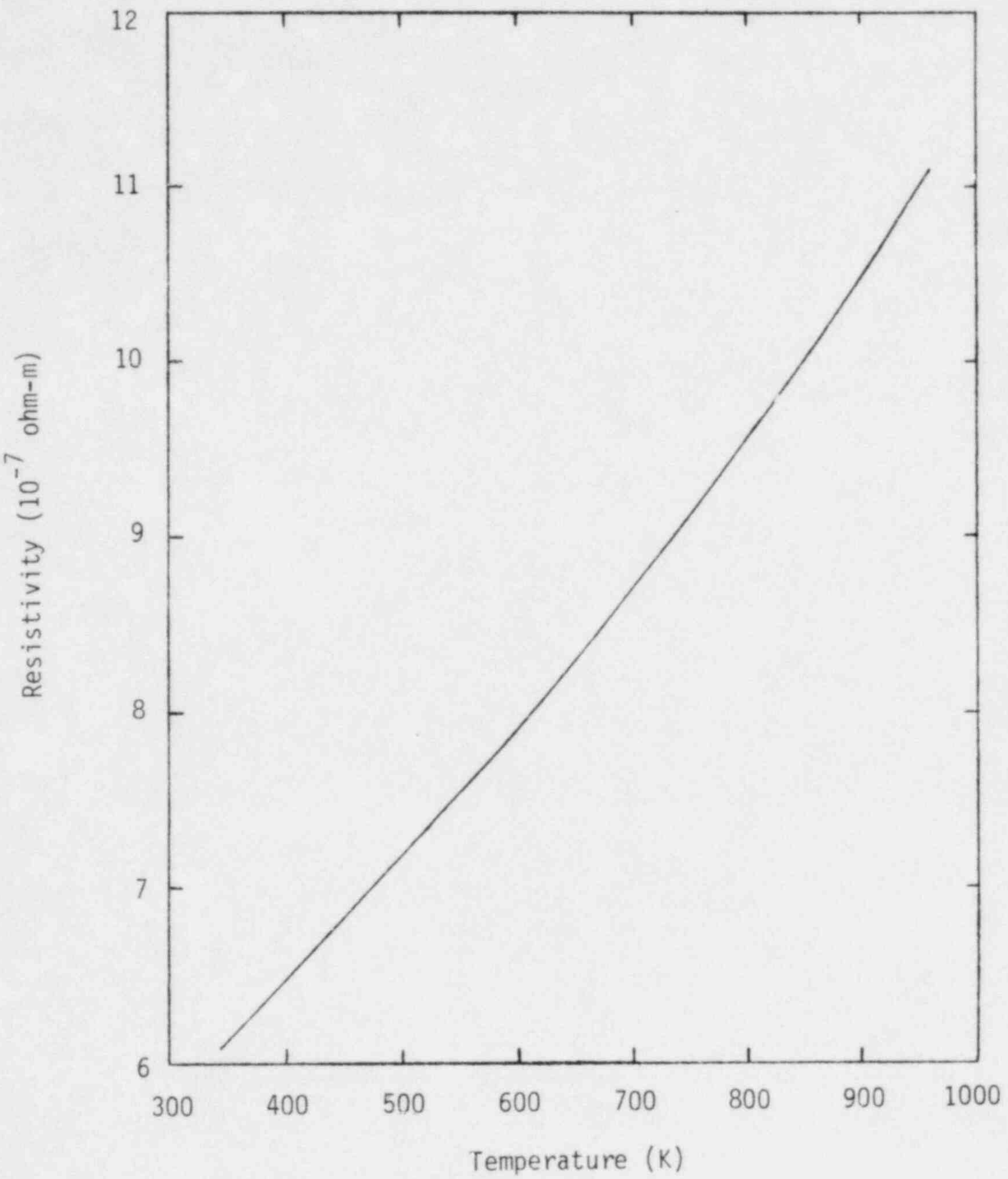

Figure 26. Resistivity of 410 stainless steel reported by Peckner and Bernstein[1].

TABLE 39. ELECTRICAL RESISTIVITY OF 410 STAINLESS STEEL FROM CURVE OF PECKNER AND BERNSTEIN[1]

Temperature (K)	Resistivity (10^{-9} ohm·m)
344	606
381	634
446	680
522	733
596	786
667	845
738	903
808	960
872	1019
911	1057
959	1108

The diffusion coefficient for 316 stainless steel is probably orders of magnitude too low for martensitic steels because the face centered cubic structure of the 316 stainless steel is a close-packed structure while the body centered tetragonal structure of martensite[66] is a more open lattice. Based on data from pure iron (which has a body centered cubic structure) to be presented in Appendix A, a diffusion coefficient of 1000 times that of 316 stainless steel is recommended for the ferritic/martensitic steels until more direct data are available.

Corrosion data are almost nonexistent. Gold et al.[24] claim liquid lithium causes severe intergranular corrosion of the 2 Cr-1 Mo-0.3 V alloy but the reference on which this claim is based is unavailable. For the time being, the 316 stainless steel corrosion rates are recommended as a first estimate in spite of the fact that its high chromium content probably implies less corrosion than the ferritic/martensitic alloys.[1]

The radioactivity from activation products has been calculated and reported by Rawls et al.[64] Their results are shown in Table 40 and Figure 27. The values are similar to those for 316 stainless steel reported in Table 24 and Figure 14.

2.4 Graphite, Pyrolytic Carbon, Vitreous Carbon and Fibrous Graphite

The carbon family of materials have been considered for protection of other fusion reactor components,[6] reflectors,[6] shields,[6] and limiters. Their use now seems limited to temperatures below 670 K because of carbon contamination.[68]

Since graphite has been used extensively in high temperature gas-cooled reactor development, several summaries of many of the appropriate properties are available.[69-71] The principal complication in modeling the behavior of this material is the anisotropy of the graphite. Variations of 0.3 of measured properties with direction are common. Another complication is caused by the many different grades of graphite and the fact that the grade of the material is not always reported.

TABLE 40. RADIOACTIVITY OF HT-9 STEEL AFTER SHUTDOWN ACCORDING TO RAWLS ET AL.[64]

Time After Shutdown (s)	Radioactivity (Ci/kW(th))
0	1.17×10^3
8.64×10^4 = 1 day	6.6×10^2
2.63×10^6 = 1 month	5.9×10^2
3.16×10^7 = 1 year	4.0×10^2
3.16×10^{10} = 1 millenium	1.8×10^{-2}

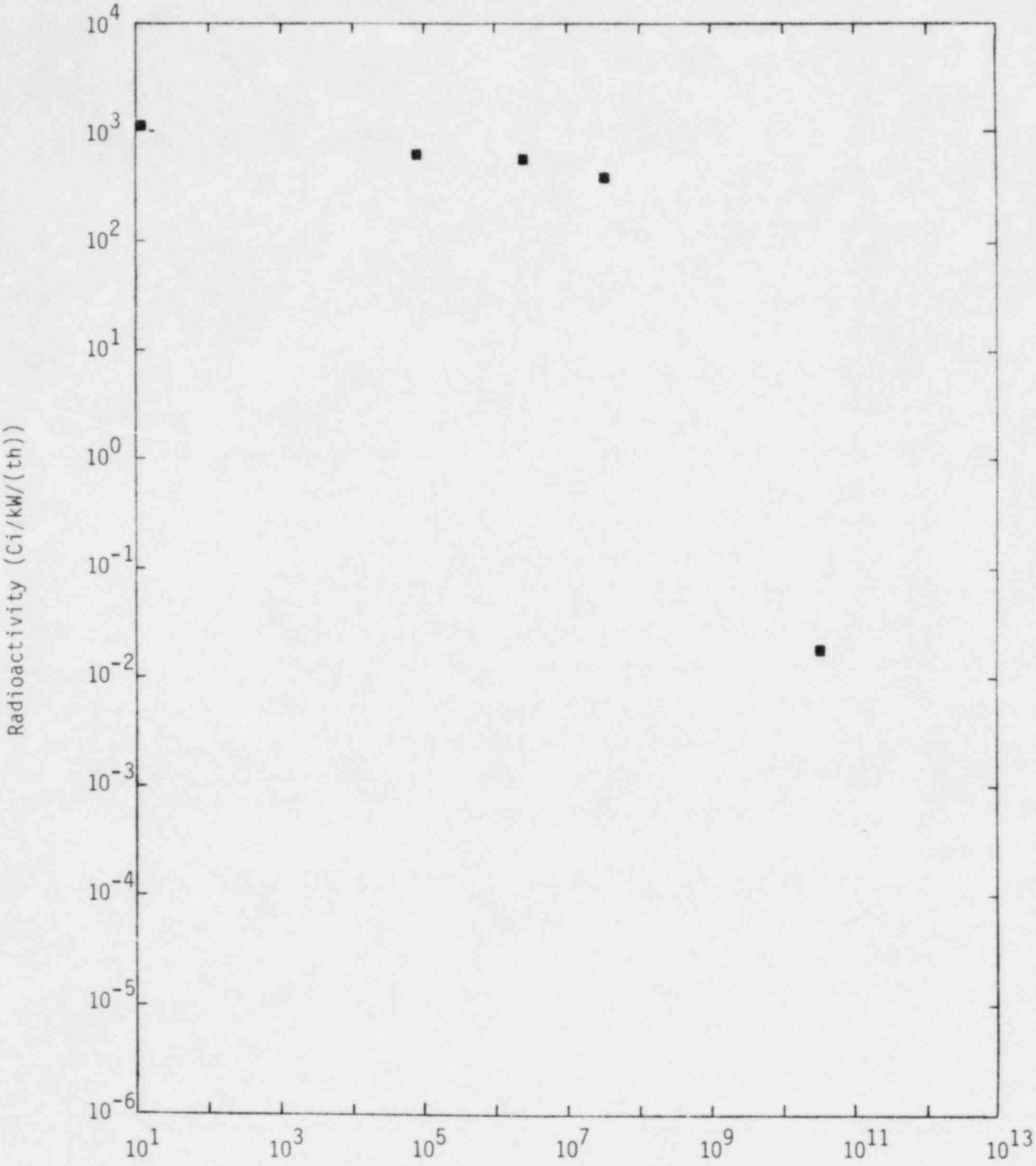

Figure 27. Radioactivity of HT-9 steel after shutdown according to Rawls et al[64].

2.4.1 Thermal Properties

All of the thermal properties that have been located are for graphite. The available data concerning specific heat capacity, enthalpy, thermal conductivity, thermal expansion, emissivity, and heat of sublimation of the graphites will be discussed in this section.

Nightingale has published a table of recommended values for the specific heat capacity and enthalpy. His table is reproduced as Table 41. Unfortunately, the reference that Nightingale credits for the table is unavailable, so details of the source of these recommendations are unknown. The specific heat capacity for graphite is higher than that of the metals in the previous sections because of the small atomic weight of carbon.

The thermal conductivity of graphite has been reported by several authors.[70-74] Engle and Beavan[70] measured the thermal conductivity of three different grades of graphite rod with the results shown in Table 42. There is significant anisotropy but even larger sample-to-sample variation which does not seem to be simply related to density variations. Additional data with different samples were presented by Ford et al. at the Bournemouth symposium.[71] These data are reproduced in Table 43 and are consistent with the results of Engle and Beavan.

Matsuo[71] presents data which do show a correlation between thermal conductivity and density (open porosity). In Matsuo's experiments, the change in open porosity was caused by oxidation. A correlation between porosity and thermal conductivity is also claimed by Kinglery[73] and demonstrated by Francl and Kingery.[74]

Data from Matsuo (Figures 1 and 2) are shown in Table 44 and the thermal conductivities measured by Francl and Kingerly are reproduced in Table 45. The results in Reference 74 are probably not measurements but least squares fits to the data in Table 45.

TABLE 41. SPECIFIC HEAT CAPACITY AND ENTHALPY AT CONSTANT PRESSURE OF GRAPHITE RECOMMENDED BY NIGHTINGALE ET AL.[69]

Temperature (K)	Specific Heat Capacity[a] (J/kg•K)	Enthalpy Change from 298 K (10^3 J/kg)
298	721	0
300	725	1.4
400	993	87.4
500	1220	198.
600	1404	330.
700	1543	477.
800	1655	637
900	1735	807
1000	1790	983.
1100	1836	1165.
1200	1888	1349.
1300	1940	1542.
1400	1975	1738.
1500	2006	1937.
1600	2031	2140.
1700	2055	2344.
1800	2073	2550.
1900	2090	2758.
2000	2107	2968.
2100	2125	3181
2200	2139	3395
2300	2153	3609
2400	2167	3825
2500	2181	4041
2600	2195	4260
2700	2205	4480
2800	2215	4703
2900	2226	4926
3000	2236	5149
3500	2599	6305

---

[a] The specific heat capacities were converted from cal/mole to J/kg using 4.184 J/cal and 12.0111×10^{-3} kg/g-mole.

TABLE 42. THERMAL CONDUCTIVITY OF SOME GRAPHITES MEASURED BY ENGLE AND BEAVAN[70]

Temperature (K)	Density (kg/m^3)	Direction	Thermal Conductivity (W/m•K)
295	1780	Axial	63.0
295	1780	Radial	62.4
295	1760	Axial	87.2
295	1760	Radial	94.3
295	1800	Axial	124.2
295	1800	Radial	128.8
673	1780	Axial	53.7
673	1780	Radial	57.2
673	1760	Axial	64.7
673	1760	Radial	67.4
673	1800	Axial	93.2
673	1800	Radial	93.5
1073	1780	Axial	40.8
1073	1780	Radial	43.9
1073	1760	Axial	47.8
1073	1760	Radial	47.2
1073	1780	Axial	65.0
1073	1780	Radial	67.3

TABLE 43. THERMAL CONDUCTIVITY OF SOME GRAPHITES REPORTED AT THE BOURNEMOUTH SYMPOSIUM[71]

Temperature (K)	Density (kg/m^3)	Direction	Thermal Conductivity (W/m•K)
373	1660-1770	Longitudinal	63
373	1660-1770	Transverse	38
373	1720	Longitudinal	67
373	1720	Transverse	33
373	1790	Longitudinal	79
373	1790	Transverse	54

TABLE 44. THERMAL CONDUCTIVITY OF SM2-24 GRAPHITE ACCORTING TO MATSUO[72]

Temperature (K)	Density (kg/m^3)	Direction	Thermal Conductivity (W/m•K)
298	1688	Perpendicular	152
298	1667	Perpendicular	142
298	1657	Parallel	114
298	1637	Parallel	127
298	1577	Perpendicular	124
298	1576	Perpendicular	120
298	1519	Parallel	111
298	1499	Parallel	98
298	1458	Perpendicular	100
298	1442	Perpendicular	102
298	1383	Parallel	76
298	1347	Perpendicular	82
298	1335	Parallel	83
298	1326	Perpendicular	77
298	1242	Perpendicular	65
298	1240	Parallel	57
298	1212	Perpendicular	67
298	1193	Parallel	59
298	1153	Perpendicular	44
298	1123	Parallel	53
298	1078	Perpendicular	45
298	1063	Parallel	39

TABLE 45. THERMAL CONDUCTIVITY OF GRAPHITE REPORTED BY FRANCL AND KINGERY[74]

Temperature (K)	Density (kg/m^3)	Direction	Thermal Conductivity (W/m•K)
351	1550	Unknown	138
352	1550	Unknown	125
417	1550	Unknown	119
417	1550	Unknown	112
473	1550	Unknown	103
501	1550	Unknown	103
505	1550	Unknown	96
566	1550	Unknown	87
566	1550	Unknown	94
695	1550	Unknown	75
695	1550	Unknown	81
772	1550	Unknown	72
807	1550	Unknown	69
807	1550	Unknown	73
860	1550	Unknown	62
861	1550	Unknown	67
992	1550	Unknown	55
994	1550	Unknown	62
1071	1550	Unknown	54
1088	1550	Unknown	53
1091	1550	Unknown	57

All of the available thermal conductivity data for graphite are shown as a function of temperature in Figure 28. The large scatter shown in the figure shows that accurate modeling of graphite thermal conductivity will require consideration of more parameters than just temperature. Since the single-crystal conductivity of graphite is about five times as large in the [001] direction as it is perpendicular to this direction,[69] the crystaline structure (orientation) is a parameter that may have to be specified or held constant. Density is another important parameter that may have to be controlled since most of the graphites that are measured are far less dense than the theoretical density of 2220 kg/m^3.[73]

Linear thermal expansion data for graphite have been reported by Fulkerson,[75] Engle and Beavan,[70] and by Ford, Hurden and Wiggs.[71] The measurements by Fulkerson are the most complete and are reproduced in Table 46. Four samples were employed, two oriented parallel to the direction of extrusion of the CS 312 graphite rod and two oriented perpendicular to the direction of extrusion. The samples cut perpendicular to the direction of extrusion have nearly 50% more thermal strain than those cut parallel to the direction of extrusion. Unfortunately, Fulkerson does not report the density of his samples.

Thermal strain data from Engle and Beavan are shown in Table 47. The data were presented as a mean coefficient of thermal expansion over the temperature range 295 to 773 K but have been converted to thermal strains. The strains from this reference are consistently less than those which would be inferred from Fulkerson's measurements.

The thermal strains from Ford et al.[71] shown in Table 48 were also calculated from a mean coefficient of thermal expansion. For the different graphites tested, the transverse strains were significantly greater than the longitudional strains.

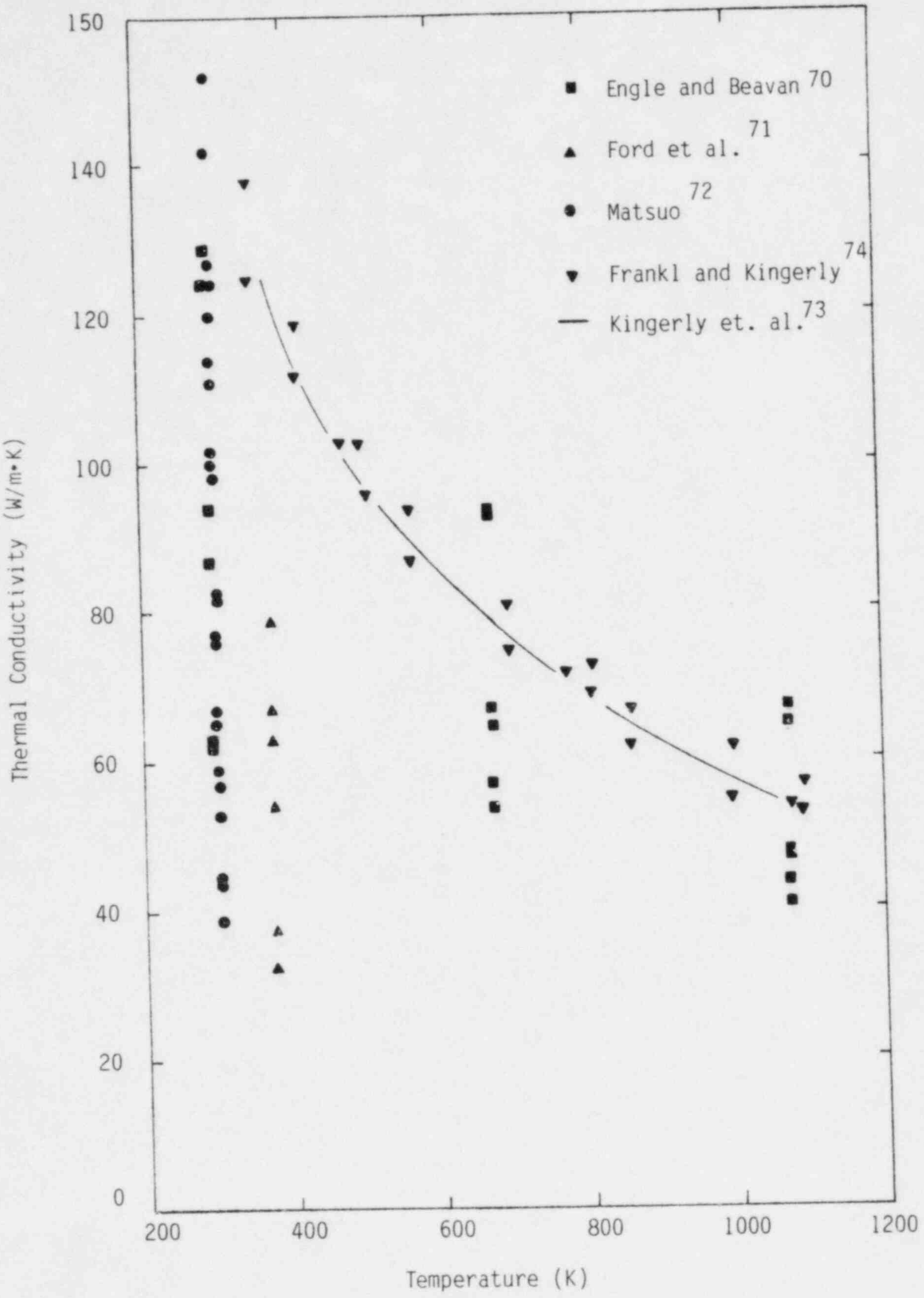

Figure 28. Thermal conductivity of several graphites as a function of temperature.

TABLE 46. LINEAR THERMAL EXPANSION STRAINS OF GRAPHITE REPORTED BY FULKERSON[75]

Temperature (K)	Direction/Location	Thermal Strain (10^{-3}m/m)
313	Parallel to extrusion, near outside	0.21
353	Parallel to extrusion, near outside	0.36
393	Parallel to extrusion, near outside	0.45
433	Parallel to extrusion, near outside	0.56
473	Parallel to extrusion, near outside	0.72
513	Parallel to extrusion, near outside	0.84
553	Parallel to extrusion, near outside	0.96
593	Parallel to extrusion, near outside	1.07
633	Parallel to extrusion, near outside	1.22
673	Parallel to extrusion, near outside	1.36
713	Parallel to extrusion, near outside	1.50
753	Parallel to extrusion, near outside	1.64
793	Parallel to extrusion, near outside	1.77
833	Parallel to extrusion, near outside	1.91
873	Parallel to extrusion, near outside	2.02
913	Parallel to extrusion, near outside	2.13
953	Parallel to extrusion, near outside	2.32
993	Parallel to extrusion, near outside	2.47
1033	Parallel to extrusion, near outside	2.64
1073	Parallel to extrusion, near outside	2.76
1113	Parallel to extrusion, near outside	2.93
1153	Parallel to extrusion, near outside	3.09
1193	Parallel to extrusion, near outside	3.23
1233	Parallel to extrusion, near outside	3.39
1273	Parallel to extrusion, near outside	3.54
1313	Parallel to extrusion, near outside	3.68
1353	Parallel to extrusion, near outside	3.83
1393	Parallel to extrusion, near outside	3.93
1433	Parallel to extrusion, near outside	4.02
1473	Parallel to extrusion, near outside	4.16
1513	Parallel to extrusion, near outside	4.34
1553	Parallel to extrusion, near outside	4.49
1593	Parallel to extrusion, near outside	4.68
1608	Parallel to extrusion, near outside	4.78
314	Parallel to extrusion, at center	0.18

TABLE 46. (continued)

Temperature (K)	Direction/Location	Thermal Strain (10^{-3}m/m)
336	Parallel to extrusion, at center	0.24
353	Parallel to extrusion, at center	0.31
372	Parallel to extrusion, at center	0.39
392	Parallel to extrusion, at center	0.44
416	Parallel to extrusion, at center	0.48
435	Parallel to extrusion, at center	0.53
452	Parallel to extrusion, at center	0.57
473	Parallel to extrusion, at center	0.64
513	Parallel to extrusion, at center	0.74
553	Parallel to extrusion, at center	0.86
593	Parallel to extrusion, at center	0.98
633	Parallel to extrusion, at center	1.14
673	Parallel to extrusion, at center	1.29
713	Parallel to extrusion, at center	1.40
753	Parallel to extrusion, at center	1.50
793	Parallel to extrusion, at center	1.60
833	Parallel to extrusion, at center	1.76
873	Parallel to extrusion, at center	1.92
913	Parallel to extrusion, at center	2.05
953	Parallel to extrusion, at center	2.21
993	Parallel to extrusion, at center	2.41
1033	Parallel to extrusion, at center	2.55
1073	Parallel to extrusion, at center	2.64
1113	Parallel to extrusion, at center	2.86
1153	Parallel to extrusion, at center	2.97
1193	Parallel to extrusion, at center	3.13
1233	Parallel to extrusion, at center	3.27
1273	Parallel to extrusion, at center	3.40
1313	Parallel to extrusion, at center	3.55
1353	Parallel to extrusion, at center	3.65
1393	Parallel to extrusion, at center	3.73
1433	Parallel to extrusion, at center	3.88
1473	Parallel to extrusion, at center	4.02
1513	Parallel to extrusion, at center	4.21
1553	Parallel to extrusion, at center	4.40

TABLE 46. (continued)

Temperature (K)	Direction/Location	Thermal Strain (10^{-3}m/m)
1593	Parallel to extrusion, at center	4.59
1618	Parallel to extrusion, at center	4.70
292	Perpendicular to extrusion, at 1/2 radius	0.10
303	Perpendicular to extrusion, at 1/2 radius	0.16
314	Perpendicular to extrusion, at 1/2 radius	0.22
332	Perpendicular to extrusion, at 1/2 radius	0.28
352	Perpendicular to extrusion, at 1/2 radius	0.35
374	Perpendicular to extrusion, at 1/2 radius	0.48
393	Perpendicular to extrusion, at 1/2 radius	0.54
412	Perpendicular to extrusion, at 1/2 radius	0.61
436	Perpendicular to extrusion, at 1/2 radius	0.69
473	Perpendicular to extrusion, at 1/2 radius	0.85
493	Perpendicular to extrusion, at 1/2 radius	0.94
513	Perpendicular to extrusion, at 1/2 radius	1.04
553	Perpendicular to extrusion, at 1/2 radius	1.24
593	Perpendicular to extrusion, at 1/2 radius	1.41
633	Perpendicular to extrusion, at 1/2 radius	1.65
673	Perpendicular to extrusion, at 1/2 radius	1.86
713	Perpendicular to extrusion, at 1/2 radius	2.05
753	Perpendicular to extrusion, at 1/2 radius	2.23
793	Perpendicular to extrusion, at 1/2 radius	2.45
833	Perpendicular to extrusion, at 1/2 radius	2.65
873	Perpendicular to extrusion, at 1/2 radius	2.86
913	Perpendicular to extrusion, at 1/2 radius	3.11
953	Perpendicular to extrusion, at 1/2 radius	3.35
993	Perpendicular to extrusion, at 1/2 radius	3.59
1033	Perpendicular to extrusion, at 1/2 radius	3.82
1073	Perpendicular to extrusion, at 1/2 radius	4.07
1113	Perpendicular to extrusion, at 1/2 radius	4.31
1153	Perpendicular to extrusion, at 1/2 radius	4.53
1193	Perpendicular to extrusion, at 1/2 radius	4.76
1233	Perpendicular to extrusion, at 1/2 radius	4.97
1273	Perpendicular to extrusion, at 1/2 radius	5.24
1313	Perpendicular to extrusion, at 1/2 radius	5.43
1353	Perpendicular to extrusion, at 1/2 radius	5.62

TABLE 46. (continued)

Temperature (K)	Direction/Location	Thermal Strain (10^{-3}m/m)
1393	Perpendicular to extrusion, at 1/2 radius	5.81
1433	Perpendicular to extrusion, at 1/2 radius	6.05
1473	Perpendicular to extrusion, at 1/2 radius	6.24
1513	Perpendicular to extrusion, at 1/2 radius	6.47
1553	Perpendicular to extrusion, at 1/2 radius	6.77
1593	Perpendicular to extrusion, at 1/2 radius	7.04
1612	Perpendicular to extrusion, at 1/2 radius	7.18
293	Perpendicular to extrusion, at center	0.12
313	Perpendicular to extrusion, at center	0.22
333	Perpendicular to extrusion, at center	0.31
353	Perpendicular to extrusion, at center	0.42
373	Perpendicular to extrusion, at center	0.53
393	Perpendicular to extrusion, at center	0.62
413	Perpendicular to extrusion, at center	0.69
433	Perpendicular to extrusion, at center	0.78
453	Perpendicular to extrusion, at center	0.88
473	Perpendicular to extrusion, at center	0.98
493	Perpendicular to extrusion, at center	1.04
513	Perpendicular to extrusion, at center	1.12
533	Perpendicular to extrusion, at center	1.18
553	Perpendicular to extrusion, at center	1.26
573	Perpendicular to extrusion, at center	1.40
593	Perpendicular to extrusion, at center	1.52
613	Perpendicular to extrusion, at center	1.59
633	Perpendicular to extrusion, at center	1.66
653	Perpendicular to extrusion, at center	1.73
673	Perpendicular to extrusion, at center	1.84
693	Perpendicular to extrusion, at center	1.92
713	Perpendicular to extrusion, at center	2.02
733	Perpendicular to extrusion, at center	2.12
753	Perpendicular to extrusion, at center	2.21
773	Perpendicular to extrusion, at center	2.33
793	Perpendicular to extrusion, at center	2.41
813	Perpendicular to extrusion, at center	2.52
833	Perpendicular to extrusion, at center	2.59

TABLE 46. (continued)

Temperature (K)	Direction/Location	Thermal Strain (10^{-3}m/m)
873	Perpendicular to extrusion, at center	2.81
913	Perpendicular to extrusion, at center	3.06
953	Perpendicular to extrusion, at center	3.33
993	Perpendicular to extrusion, at center	3.55
1033	Perpendicular to extrusion, at center	3.78
1073	Perpendicular to extrusion, at center	4.02
1113	Perpendicular to extrusion, at center	4.21
1153	Perpendicular to extrusion, at center	4.42
1193	Perpendicular to extrusion, at center	4.63
1233	Perpendicular to extrusion, at center	4.83
1273	Perpendicular to extrusion, at center	5.08
1313	Perpendicular to extrusion, at center	5.29
1353	Perpendicular to extrusion, at center	5.48
1393	Perpendicular to extrusion, at center	5.64
1433	Perpendicular to extrusion, at center	5.84
1473	Perpendicular to extrusion, at center	6.03
1513	Perpendicular to extrusion, at center	6.25
1553	Perpendicular to extrusion, at center	6.44
1593	Perpendicular to extrusion, at center	6.70
1619	Perpendicular to extrusion, at center	6.95

TABLE 47. LINEAR THERMAL EXPANSION STRAINS OF GRAPHITES REPORTED BY ENGLE AND BEAVAN[70]

Temperature (K)	Grade	Direction/Location	Density kg/m^3	Thermal Strain ($10^{-3}m/m$)
773	2020	Axial/end	1784±130	1.61
773	2020	Radial/end	1784±130	1.57
773	2020	Axial/midlength	1784±130	1.63
773	2020	Radial/midlength	1784±130	1.52
773	HLM	Axial/end center	1770-1830	1.18
773	HLM	Radial/end center	1770-1830	1.37
773	HLM	Axial/end midradius	1770-1830	1.20
773	HLM	Radial/end midradius	1770-1830	1.37
773	HLM	Axial/end edge	1770-1830	1.09
773	HLM	Radial/end edge	1770-1830	1.42
773	HLM	Axial/midlength center	1770-1830	1.21
773	HLM	Radial/midlength center	1770-1830	1.30
773	HLM	Axial/midlength midradius	1770-1830	1.20
773	HLM	Radial/midlength midradius	1770-1830	1.34
773	HLM	Axial/midlength edge	1770-1830	1.17
773	HLM	Radial/midlength edge	1770-1830	1.36

TABLE 48. LINEAR THERMAL EXPANSION STRAINS OF GRAPHITES REPORTED AT THE BOURNEMOUTH SYMPOSIUM[71]

Temperature (K)	Grade	Direction	Density kg/m^3	Thermal Strain $(10^{-3} m/m)$
1273	EY9	Longitudinal	1660-1770	2.9
1273	EY9	Transverse	1660-1770	5.6
1273	EYX60	Longitudinal	1720	3.0
1273	EYX60	Transverse	1720	6.0
1273	EYX66	Longitudinal	1790	2.8
1273	EYX66	Transverse	1790	4.7

Figure 29 illustrates all the available thermal strain data. Not only is considerable sample-to-sample variation present, but a significant anisotropy is obvious in the figure. The significant effect of direction suggests that an uncertainty of less than 30% will require characterization of the graphite's grain structure or data from material produced in a manner very similar to the graphite being modeled. Even larger uncertainties are suggested by Nightingale[69] but not supported by data.

The only graphite emissivity data found are a value of 0.82 at 773 K published by Francl and Kingery[74] and a recommended linear increase with temperature by these authors. The increase suggested can be approximated in the temperature range 700 K to 1400 K with the relation

$$\varepsilon = 0.73 + 1.28 \times 10^{-4}\ T \tag{30}$$

where

ε = total normal emissivity

T = temperature (K).

Since the triple point of carbon is 100 atmospheres and 4100 K,[69] the heats of fusion and vaporization are not needed. Nightingale[69] reports that the heat of sublimation is in some doubt because of an uncertainty in the composition of the vapor. Theoretical calculations predict heats of sublimation ranging from 5.9112 J/kg solid if the vapor is carbon atoms to 8.104 J/kg solid for C_5 vapor.

2.4.2 Mechanical Properties

Most of the carbon mechanical properties that have been located are for nuclear grade graphites. The available data for elastic moduli, plastic moduli or creep, failure stress, cyclic fatigue, irradiation growth or swelling, and fracture toughness will be discussed.

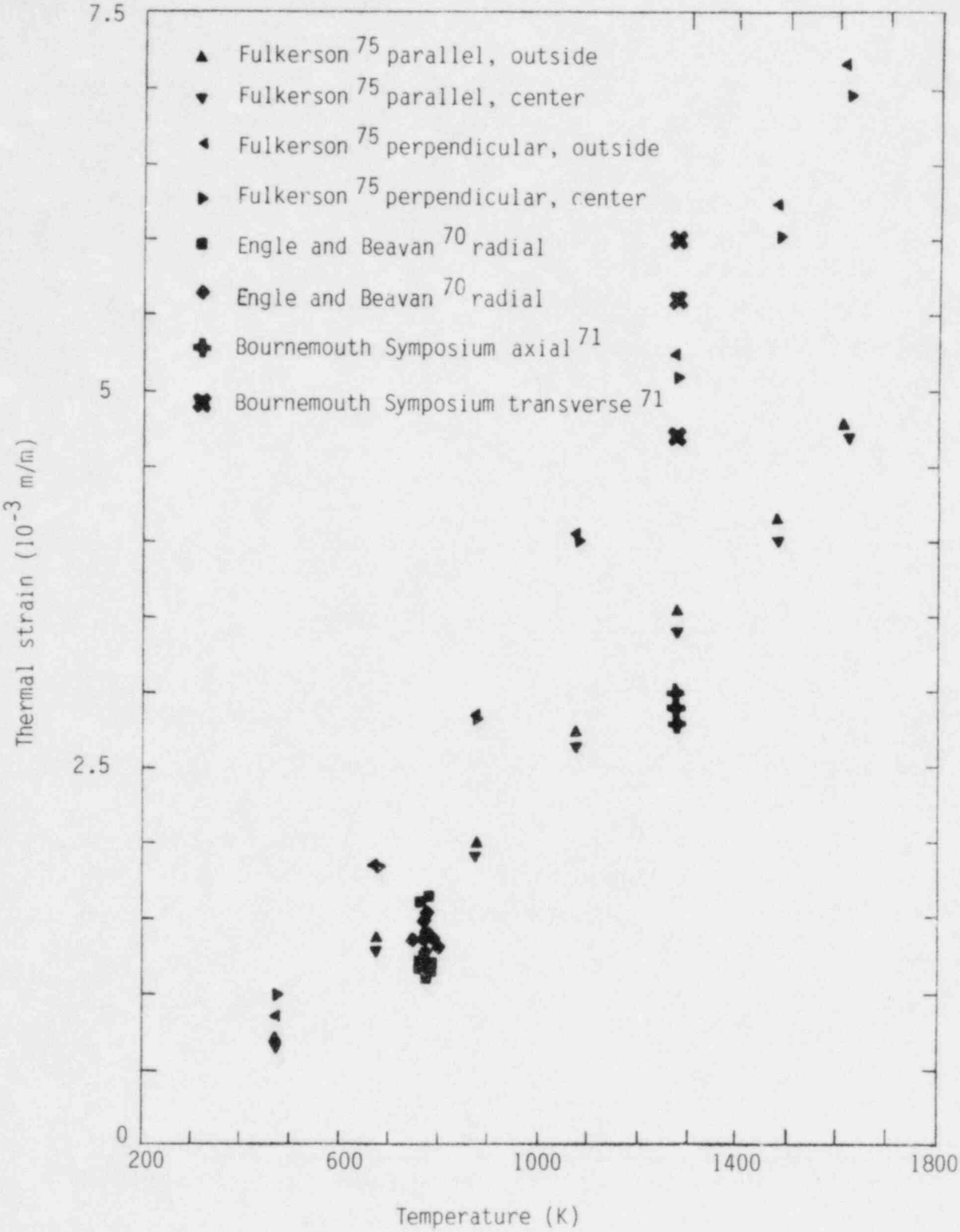

Figure 29. Thermal strains for several graphites.

The elastic modulus for graphites is difficult to define because the stress-strain curve is not linear on the first loading.[69,71] Typically, the second loading curve is used to define a slope because it is fairly linear. Young's moduli defined in this manner by Ford, Hurden, and Wiggs[71] are shown in Table 49. The moduli are a function of the sign of the stress as well as it's direction relative to the grain of the extruded graphites. In addition to the compression and tension modes shown in the table, a vibrational mode was used which yielded Young's moduli of 13.0 x 10^9 Pa in the longitudional direction and 5.4 x 10^9 Pa in the transverse direction. These values were reported to increase gradually with temperature in the range 273 to 1273 K, producing a 10% increase by 1273 K.

An extensive collection of Young's moduli measurements by Engle and Beavan[70] is reproduced in Table 50. Unfortunately the measurement temperature was not given in Reference 70. All measurements are therefore assumed to be at room temperature.

No data for the shear moduli of graphite have been found but a Poisson's ratio of about 0.4 is suggested by Ford et al. This value can be used with Equation (1) to provide a crude estimate for the shear modulus but the result is suspect since neither Poisson's ratio, the shear modulus, nor Equation (1) is uniquely defined for an anisotropic material like graphite.

The only other data on graphite elastic moduli that have been found are a value of 6.2 x 10^9 Pa in a sample of PGX graphite (direction unknown)[77] and a report that the shear modulus increases by more than it's zero-fluence value when graphite is irradiated.[77]

Numerous authors[68-71,76] report the tensile and compression strengths of graphite. Unfortunately, these data are not sufficient to provide the means of relating stress to deformation that is likely to be needed for analysis. The method proposed to deduce an equation of state for 316 stainless steel from yield strength, ultimate strength, and uniform elongation fails because the yield strength and uniform elongation are not available

TABLE 49. YOUNG'S MODULUS OF GRAPHITE REPORTED AT THE BOURNEMOUTH SYMPOSIUM[71]

Temperature (K)	Grade	Directions	Density kg/m^3	Young's Modulus (10^9 Pa)
300	EY9	Longitudinal/compression		7.3
300	EY9	Transverse/compression		3.8
300	EY9	Longitudinal/tension		12.
300	EYX60	Longitudinal/compression		9.8
300	EYX60	Transverse/compression		6.3
300	EYX66	Longitudinal/compression		8.8
300	EYX66	Transverse/compression		4.3

TABLE 50. YOUNG'S MODULUS OF GRAPHITES MEASURED BY ENGLE AND BEAVAN[70]

Temperature (K)	Grade	Directions	Density (kg/m^3)	Young's Modulus (10^9 Pa)
300	2020	Axial/compression	1787	10.0
300	2020	Axial/tension	1787	7.3
300	2020	Axial/tension	1764	8.1
300	2020	Axial/tension	1789	9.3
300	2020	Axial/compression	1790	8.7
300	2020	Axial/tension	1790	7.1
300	2020	Axial/tension	1772	8.2
300	2020	Axial/tension	1793	9.2
300	2020	Radial/compression	1790	9.9
300	2020	Radial/tension	1789	7.9
300	2020	Radial/tension	1763	8.7
300	2020	Radial/tension	1792	9.9
300	2020	Radial/compression	1796	9.8
300	2020	Radial/tension	1796	7.6
300	2020	Radial/tension	--	9.4
300	2020	Radial/tension	1773	8.6
300	2020	Radial/tension	1798	10.1
300	PGX	Axial/compression	1790	5.4
300	PGX	Axial/tension	1790	6.3
300	PGX	Axial/tension	1740	6.3
300	PGX	Axial/compression	1774	5.2
300	PGX	Axial/tension	1774	6.2
300	PGX	Axial/tension	1740	5.9
300	PGX	Axial/compression	1781	5.6
300	PGX	Axial/tension	1781	6.5
300	PGX	Axial/tension	1745	5.8
300	PGX	Axial/compression	1790	5.5
300	PGX	Axial/tension	1790	6.6
300	PGX	Axial/tension	1750	6.2
300	PGX	Axial/compression	1780	5.4
300	PGX	Axial/tension	1780	6.5
300	PGX	Axial/tension	1745	6.0
300	PGX	Axial/compression	1779	5.0
300	PGX	Axial/tension	1779	6.2
300	PGX	Axial/tension	1732	5.7

TABLE 50. (continued)

Temperature (K)	Grade	Directions	Density (kg/m^3)	Young's Modulus (10^9 Pa)
300	PGX	Axial/compression	1780	4.7
300	PGX	Axial/tension	1780	6.1
300	PGX	Axial/tension	1730	5.7
300	PGX	Axial/compression	1773	4.5
300	PGX	Axial/tension	1773	6.0
300	PGX	Axial/tension	1730	5.6
300	PGX	Axial/compression	1783	4.9
300	PGX	Axial/tension	1783	6.2
300	PGX	Axial/tension	1736	5.7
300	PGX	Radial/compression	1790	5.4
300	PGX	Radial/tension	1790	7.2
300	PGX	Radial/tension	1742	7.3
300	PGX	Radial/compression	1774	5.3
300	PGX	Radial/tension	1774	6.8
300	PGX	Radial/tension	1739	7.2
300	PGX	Radial/compression	1776	5.4
300	PGX	Radial/tension	1776	6.7
300	PGX	Radial/tension	1735	7.7
300	PGX	Radial/compression	1791	6.4
300	PGX	Radial/tension	1791	7.7
300	PGX	Radial/tension	1748	7.5
300	PGX	Radial/compression	1783	5.9
300	PGX	Radial/tension	1783	7.3
300	PGX	Radial/tension	1744	7.5
300	PGX	Radial/compression	1778	6.0
300	PGX	Radial/tension	1778	7.1
300	PGX	Radial/tension	1734	7.1
300	PGX	Radial/compression	1775	5.3
300	PGX	Radial/tension	1775	6.9
300	PGX	Radial/tension	1731	6.9
300	PGX	Radial/compression	1777	5.5
300	PGX	Radial/tension	1777	6.9
300	PGX	Radial/tension	1733	7.2
300	PGX	Radial/compression	1777	5.8
300	PGX	Radial/tension	1777	7.4

TABLE 50. (continued)

Temperature (K)	Grade	Directions	Density (kg/m^3)	Young's Modulus (10^9 Pa)
300	PGX	Radial/tension	1740	7.2
300	HLM	Axial/compression	1772	6.7
300	HLM	Axial/tension	1772	7.4
300	HLM	Axial/tension	1807	9.3
300	HLM	Axial/compression	1774	5.0
300	HLM	Axial/tension	1774	7.0
300	HLM	Axial/tension	1806	9.2
300	HLM	Axial/compression	1784	5.1
300	HLM	Axial/tension	1784	6.9
300	HLM	Axial/tension	1796	8.7
300	HLM	Axial/compression	1794	7.1
300	HLM	Axial/tension	1794	7.7
300	HLM	Axial/tension	1796	9.2
300	HLM	Axial/compression	1798	5.7
300	HLM	Axial/tension	1798	7.2
300	HLM	Axial/tension	1807	9.2
300	HLM	Axial/compression	1796	5.3
300	HLM	Axial/tension	1796	6.9
300	HLM	Axial/tension	1817	9.0
300	HLM	Axial/tension	1802	9.1
300	HLM	Axial/tension	1809	9.3
300	HLM	Axial/tension	1820	9.2
300	HLM	Radial/compression	1771	5.3
300	HLM	Radial/tension	1771	5.8
300	HLM	Radial/tension	1808	7.7
300	HLM	Radial/compression	1774	5.7
300	HLM	Radial/tension	1774	6.2
300	HLM	Radial/tension	1806	8.1
300	HLM	Radial/compression	1780	5.9
300	HLM	Radial/tension	1780	6.6
300	HLM	Radial/tension	1797	8.1
300	HLM	Radial/compression	1794	5.9
300	HLM	Radial/tension	1794	6.1
300	HLM	Radial/tension	1798	7.3
300	HLM	Radial/compression	1795	5.8

'ABLE 50. (continued)

Temperature (K)	Grade	Directions	Density (kg/m^3)	Young's Modulus (10^9 Pa)
300	HLM	Radial/tension	1795	6.2
300	HLM	Radial/tension	1809	7.8
300	HLM	Radial/compression	1796	5.9
300	HLM	Radial/tension	1796	6.6
300	HLM	Radial/tension	1817	8.0
300	HLM	Radial/tension	1811	7.6
300	HLM	Radial/tension	1819	8.2
300	HLM	Radial/tension	1822	8.2

and because the form of the equation of state for metals may well be incorrect for graphite. At the present time, the best that can be done is to assume an equation of state of the form of Equation (2), and adjust the strength coefficient and strain hardening exponent until typical stress-strain diagrams like those of Reference 69 are approximated by the elastic and plastic equations of state.

Although no data for graphite creep have been found, Nightingale[69] has provided a useable summary of creep behavior. He reports that creep in the temperature range 1473 to 2273 K can be modeled with one equation

$$\varepsilon = \sigma\left[\frac{1}{M_T} + \frac{13 \log t}{M_R} \exp\left(\frac{-10000}{T}\right) + 3.31 \times 10^{-11}\ t \exp\left(\frac{-20000}{T}\right)\right] \tag{31}$$

where

ε = strain at time t (min)

σ = applied stress (dynes/cm^2)

M_R = elastic modulus at room temperature (dynes/cm^2)

M_T = elastic modulus at test temperature (dynes/cm^2)

t = time (min)

T = temperature (K).

When the applied stress is removed, the transient component of the creep strain is supposed to be recovered logarithmically but no quantative expression is given.

In the temperature range 2273 to 3273 K Nightingale proposes the following equation to describe graphite steady-state creep:

$$\frac{de}{dt} = K\left(\frac{\sigma}{\sigma_B}\right)^{3.8} e - \frac{\Delta E}{T} \qquad (32)$$

where

$\frac{de}{dt}$ = strain rate (m/m)

σ = applied stress (Pa)

σ_B = stress required to produce failure (Pa). (This property will be discussed below.)

ΔE = a constant, 25000 for compression and 34000 for tension

K = a constant, 40 for compression and 4 for tension.

Short-term tensile creep in the temperature range 2273 to 2673 K is not described by Nightingale but part of an expression for 2673 to 3273 K is presented. The only other source of creep information is a general discussion by Bokros et al.[78]

The only failure stresses reported as such found for graphites are those reported by Brown and Brant on page 221 of Reference 71. The value given by these authors, 21.7×10^6 Pa at room temperature, is similar to the tensile strength of graphite because the strain at failure of graphite is exceedingly small. Nightingale[69] says on page 149 that the breaking strain is typically 0.0 to 0.003 in tension and 0.01 to 0.04 in compression. These small strains are confirmed by Langley et al.[68] and the small failure strains suggest that the curves for ultimate strength versus temperature in Nightingale's text may be used as a reasonable estimate of the true failure stress.

No data for graphite cyclic fatigue have been found. Since graphite is not a metal, cyclic fatigue is probably not an important phenomena.

Although irradiation growth and swelling are typically not considered to be a material property, they are often modeled with a correlation as though they were a property. The subject will thus be dismissed by mentioning that some information is available in References 78 through 81.

Unfortunately, no fracture toughness data have been found for graphite. This mode of failure is potentially important so the lack of data is serious.

2.4.3 Electromagnetic Properties

The electrical resistivity of several nuclear graphites at room temperature are reported by Ford et al.[71] and by Shimotomai et al.[82] In addition, Ford presents several high temperature measurements on one graphite. The available data are reproduced in Table 51, where it can be seen that the electrical resistivity is highly anisotropic, inversely proportional to the density and decreases with increasing temperature. The resistivity is surprisingly low for a nonmetal, in fact in some high-density graphites it is lower than the electrical resistivity of 316 stainless steel.

A little information about the significant increase in resistivity in irradiated graphites is presented in Figure 3 of Shimotomai et al. According to this figure annealing occurs mostly in the range 1473 to 1773 K and reduces the room temperature resistivity to one tenth of its irradiated value.

No information on the magnetic properties of graphite has been located.

2.4.4 Physical/Chemical Properties

The physical/chemical properties of graphite that will be discussed are density, melting temperature, hydrogen isotope permeability, hydrogen isotope diffusion rates, hydrogen isotope solubility, hydrogen isotope

TABLE 51. ELECTRICAL RESISTIVITY OF SEVERAL GRAPHITES

Temperature (K)	Material	Density (kg/m^3)	Direction	Resistivity (10^{-7} ohm•m)
293	highly oriented pyrolytic graphite[a]	2.260	"a-axis"	4.0-4.2
293	pyrolytic graphite annealed at 3270 K[a]	2.250	"a-axis"	8.0
293	nuclear graphite from Tokai Carbon Co[a]	1700	"a-axis"	95
293	Natural monocrystalline flaky graphite[a]	2260	"a-axis"	4.0
293	pyrolytic graphite as deposited[a]	2200	"a-axis"	45.0
293	EYX9 nuclear graphite[b]	--	longitudinal	200
293	EYX9 nuclear graphite[b]	--	transverse	420
293	EYX60 nuclear graphite[b]	1720	longitudinal	230
293	EYX60 nuclear graphite[b]	1720	transverse	410
293	EYX66 nuclear graphite[b]	1790	longitudinal	125
293	EYX66 nuclear graphite[b]	1790	transverse	195
293	EY9 nuclear graphite[b]	1660-1770	longitudinal	200
293	EY9 nuclear graphite[b]	1660-1770	transverse	420
573	EY9 nuclear graphite[b]	1660-1770	longitudinal	157
573	EY9 nuclear graphite[b]	1660-1770	transverse	323
873	EY9 nuclear graphite[b]	1660-1770	longitudinal	138
873	EY9 nuclear graphite[b]	1660-1770	transverse	274
1173	EY9 nuclear graphite[b]	1660-1770	longitudinal	129
1173	EY9 nuclear graphite[b]	1660-1770	transverse	252
1473	EY9 nuclear graphite[b]	1660-1770	longitudinal	127

TABLE 51. (continued)

Temperature (K)	Material	Density (kg/m^3)	Direction	Resistivity (10^{-7} ohm·m)
1473	EY9 nuclear graphite[b]	1660-1770	transverse	242
1673	EY9 nuclear graphite[b]	1660-1770	longitudinal	127
1673	EY9 nuclear graphite[b]	1660-1770	transverse	238

a. From Ford et al.[72]

b. From Shimotomin et al.[83]

reflection coefficients, hydrogen isotope trapping coefficients, hydrogen isotope molecular recombination rates, isotope sputtering yields, oxidation rates and activation product decay times.

Nightingale[69] provides a useful summary of most of the physical properties of graphites. He reports that the theoretical density of graphite is 2260 kg/m^3. The lowest densities found are for activated carbon (1460 kg/m^3) and sugar carbon (1500 kg/m^3) while densities approaching theoretical densities are possible in petroleum cokes and natural graphite.

The melting point of graphite, 4000 K, is somewhat academic since a pressure of 100 atmospheres is required for the existence of the liquid phase.[60]

Hydrogen isotope permeability and solubility do not follow a (pressure difference)$^{0.5}$ relation in graphite like they do in the previously discussed metals. Presumably, this is because the hydrogen concentration across a graphite barrier is not caused by solubility differences. The appropriate relation, according to J. L. Jackson in Section 6-9 of Reference 69, is

$$\frac{1}{A}\frac{dn}{dt} = \frac{K}{L}\,\Delta\left(\frac{n}{v}\right) \tag{33}$$

where

A = cross-sectional area of the barrier (m^2)

n = number of hydrogen molecules

v = gas volume (m^3)

K = a permeability coefficient (1/m^2)

L = length of the graphite barrier in the direction of flow (m).

(For an ideal gas, n/v is proportional to the pressure, not the square root of the pressure.) The permeability coefficient is proportional to the mean pressure of the gas in the graphite and inversely proportional to the viscosity of the gas (Darcy's law) as long as the diameters of pores in the body are less than or equal to the mean free paths of the gas molecules. Permeabilities of several graphites from Table 6.22 of Reference 69 are reproduced in Table 52.

Although an informative treatment of the self-diffusion in graphite is available beginning on page 127 of Reference 69, no direct treatment of hydrogen in graphite has been found. The best approach that the author can suggest at present would be to use the ideal gas law to determine a concentration difference at the two surfaces of graphite; then employing this result with Equation (33) to deduce an expression for the volume diffusion rate of hydrogen in graphite.

An important difference between the usual laboratory measurement of hydrogen permeation in graphite, which is driven by pressure differences, and the fusion-reactor situation is that the fusion reactor hydrogen isotope concentration gradient is established by plasma particles striking the surface, not steady state pressure. Thus hydrogen isotope reflection coefficients and trapping coefficients data are needed. Although several authors have begun to investigate hydrogen[83-85] and helium[86] isotope release from graphites, the needed data have not yet been published in usable form. The most useful results are the calculated results presented in Figure 5 of Reference 37 and the data of Hucks, Flaskamp and Vietzke[85] which show that the fraction of hyperthermal (2700 K) hydrogen ions retained by pyrolytic graphite varies from 0.04 at a fluence of $10^{19}/m^2$ to 0.0024 at $10^{23}/m^2$. The trapping efficiency is reported to rise with temperatures up to 700 K and then decrease drastically.

Surface sputtering yield data for several incident hydrogen isotopes have been reported by Das, Kaminsky, and Tishler,[87] Behrisch et al.[49] and Roth et al.[88] An excellent summary of these and other data is available in Reference 37 which points out that more low energy data are needed. The available data are reproduced in Table 53.

TABLE 52. PERMEABILITIES OF SEVERAL GRAPHITES ACCORDING TO JACKSON[69]

Material	Permeability ($1/m^2$)
British Pile Grade A	2×10^{-16} to 3×10^{-15}
National Carbon Grade AVF	4×10^{-15}
Pyrolytic graphite	2.7×10^{-14}

TABLE 53. GRAPHITE SPUTTERING YIELD MEASUREMENTS

Hydrogen Isotope	Target Material	Particle Energy (10^{-16} J)	Bulk Temperature	Surface Temperature	Surface Orientation	Reference	Sputtering Yield
H_2^+	ATJ graphite	64	305	305 to 473	--	Das et al[87]	$(3.5\pm0.3)\times10^{-3}$
H_2^+	ATJ graphite	96	323	323 to 473	--	Das et al[87]	$(5.5\pm0.4)\times10^{-3}$
H_2^+	ATJ graphite	192	368	533	--	Das et al[87]	$(3.5\pm0.1)\times10^{-2}$
H_2^+	pyrolytic graphite	12	--	--	--	Behriesh et al[49]	$(1.5\pm0.3)\times10^{-2}$
H_2^+	pyrolytic graphite	4.8	--	--	--	Behriesh et al[49]	$2.4\ \times10^{-2}$
H_2^+	pyrolytic graphite	4.8	--	--	--	Behriesh et al[49]	$2.6\ \times10^{-3}$
H_3^+	pyrolytic graphite	3.2	--	--	--	Behriesh et al[49]	$4.8\ \times10^{-3}$
H_3^+	pyrolytic graphite	1.6	--	--	--	Behriesh et al[49]	$2.3\ \times10^{-3}$
H_3^+	phrolytic graphite	2.1	--	--	--	Behriesh et al[49]	$4\ \times10^{-3}$
H_2^+	glassy carbon	4.8	--	--	--	Behriesh et al[49]	$1.4\ \times10^{-2}$
H_2^+	graphite fibers	4.8	--	--	--	Behriesh et al[49]	$2.6\ \times10^{-2}$
H_e^+	pyrolytic graphite	9.6	--	--	--	Behriesh et al[49]	$1.8\ \times10^{-1}$
H_2^+	pyrolytic graphite	12	--	--	edge	Roth et al[88]	$(1.5\pm0.3)\times10^{-2}$
H_2^+	pyrolytic graphite	4.8	--	--	edge	Roth et al[88]	$(1.7\pm0.7)\times10^{-2}$
H_2^+	pyrolytic grphite	4.8	--	--	basal	Roth et al[88]	$1.2\ \times10^{-2}$
H_3^+	pyrolytic graphite	4.8	--	--	basal	Roth et al[88]	$1.53\ \times10^{-2}$
H_e^+	pyrolytic graphite	9.6	--	--	basal	Roth et al[88]	$9.1\ \times10^{-2}$
H_2^+	pyrolytic graphite	4.8	--	--	edge	Roth et al[88]	$2.6\ \times10^{-3}$
H_3^+	pyrolytic graphite	3.2	--	--	edge	Roth et al[88]	$(4.9\pm0.5)\times10^{-3}$
H_3^+	pyrolytic graphite	2.7	--	--	edge	Roth et al[88]	$4.\ \times10^{-3}$
H_3^+	pyrolytic graphite	3.7	--	--	edge	Roth et al[88]	$2.3\ \times10^{-3}$

The data for graphite oxidation that have been found are extremely limited. Ford et al.[71] report weight losses of 20×10^{-3}, 75×10^{-3} and 80×10^{-3} kg/m^2 surface at 873 K for three different graphites in air. No data on the rates at other temperatures or in low partial pressures of oxygen have been found.

Although radioactivity from activation products is a significant concern for reactor safety, no data have been found on the radioactivity of typical graphites as a function of time after shutdown. Since the radioactivity can be affected by impurities and since these vary significantly from lot-to-lot, considerable variation must be expected. A scoping experimental measurement would be a useful project.

2.5 Silicon Carbide

Silicon carbide is the prime candidate ceramic for use as a first-wall structure, limiter or armor.[24] Two signficant summaries of basic silicon carbide properties have been published,[89,90] but many of the specialized properties required for fusion reactor analysis are not available. Also, the data which describe the effect of radiation on the properties are very limited.

2.5.1 Thermal Properties

Although some data are available for silicon carbide specific heat capacity, enthalpy, thermal conductivity, thermal expansion, emissivity, and heat of fusion, most of the original references are difficult to obtain.

Goldsmith et al. recommend[90] the silicon carbide specific heat capacity values reproduced in Figure 30. The curve is based on data from four references which are not reproduced because the original sources are not yet available. Table 54 is a series of points that were used to generate the curve shown in Figure 30. The specific heat capacity of SiC is higher than that of metals but lower than the specific heat capacity of carbon because

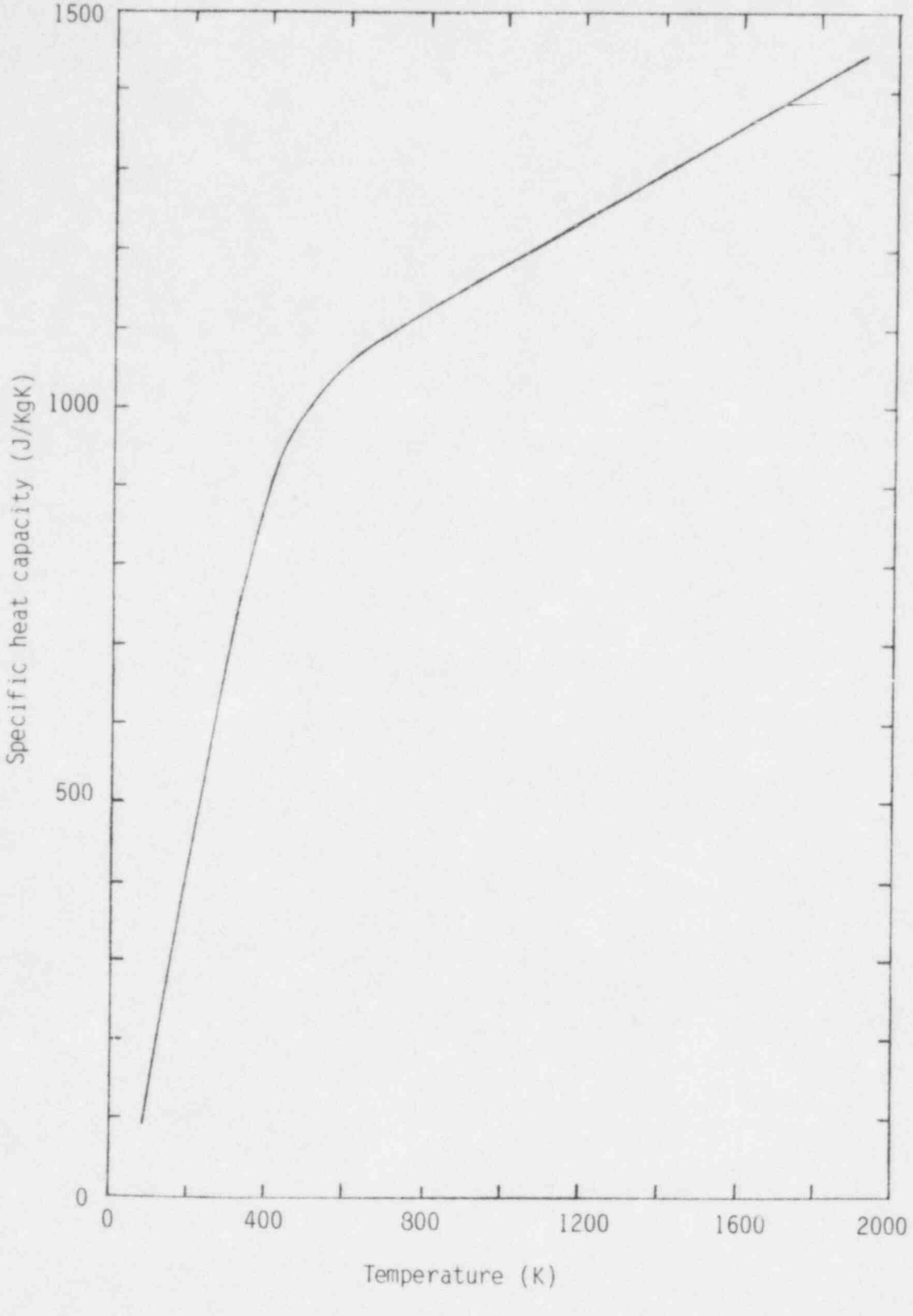

Figure 30. Silicon carbide specific heat capacity values recommended by Goldsmith et al.89

TABLE 54. SPECIFIC HEAT CURVE FOR SiC RECOMMENDED BY GOLDSMITH ET AL.[89]

Temperature (K)	Specific Heat Capacity (J/kg•K)
84	91
128	211
182	377
238	528
279	640
321	738
368	843
382	871
409	919
438	956
467	982
511	1016
544	1032
584	1052
630	1072
686	1089
797	1122
930	1160
1096	1211
1284	1267
1532	1336
1736	1396
1911	1447

the molecular weight of the compound is intermediate. Most of the data presented by Goldsmith are very close (within ±0.1 of the given value) to the curve he presents so that considerable confidence in the curve is justified.

The thermal conductivity of silicon carbide varies much more from sample to sample than the specific heat capacity does. Numerous sources of data[a] are mentioned in Goldsmith et al.[89] and in Lynch.[90] The principal conclusion from these data is that the sample-to-sample variations are large at lower temperatures (less than 1500 K). Since the material is a semi-conductor, the classical phonon theory should apply and the low temperature scatter should disappear at higher temperatures where impurities and density variations are not so important. Representative data from several sources[91-93] are shown in Table 55. The reciprocal temperature dependence of phonon conductivity and reduction in the low temperature conductivity with radiation damage are evident. Additional measurements of thermal diffusivity are available from Lee et al.[94]

Table 56 and Figure 31 display those silicon carbide thermal strain data for which the first reference has been found. The data of Fulkerson[55] were decreased by 0.1×10^{-3} m/m to account for the fact that his reference temperature was 273 K instead of 298 K and additional data are referenced in both Goldsmith et al.[89] and Lynch.[90] The principal feature of the data in Table 56 and Figure 31 is that the four samples do not show the large sample-to-sample scattering that was evident in thermal conductivity. It is also interesting to note that the thermal strains are similar to the thermal strains found with graphite and about half the thermal strains of vanadium and 316 stainless steel.

No first-hand data for the emissivity of silicon carbide are available but Goldsmith et al.[89] have published results from an unavailable reference showing a total emissivity which varies between 0.81 and 0.85 in the temperature range 0 to 1800 K.

---

[a] These data have not been reproduced because the original references have not been found.

TABLE 55. SILICON CARBIDE THERMAL CONDUCTIVITY MEASUREMENTS

Temperature (K)	Density (kg/m^3)	Fast Neutron Fluence (n/m^2)	Thermal Conductivity (W/m•K)	Reference
343	2800	0	205	Weeks and Seifert[91]
293	--	0	63	Price[92]
293	--	0	50	Price[92]
293	--	3.8×10^{25}	19	Price[92]
293	--	2.7×10^{25}	8	Price[92]
293	--	6.0×10^{25}	10	Price[92]
293	--	6.0×10^{25}	10	Price[92]
293	--	7.7×10^{25}	9	Price[92]
293	--	7.7×10^{25}	8	Price[92]
293	--	5.2×10^{25}	11	Price[92]
293	--	5.2×10^{25}	12	Price[92]
414	0.783 theoretical	0	41.7	Vasilos and Kingery[93]
490	0.783 theoretical	0	38.9	Vasilos and Kingery[93]
577	0.783 theoretical	0	35.1	Vasilos and Kingery[93]
600	0.783 theoretical	0	33.7	Vasilos and Kingery[93]
695	0.783 theoretical	0	30.9	Vasilos and Kingery[93]
780	0.783 theoretical	0	27.9	Vasilos and Kingery[93]

TABLE 55. (continued)

Temperature (K)	Density (kg/m^3)	Fast Neutron Fluence (n/m^2)	Thermal Conductivity (W/m•K)	Reference
884	0.783 theoretical	0	24.0	Vasilos and Kingery[93]
969	0.783 theoretical	0	22.8	Vasilos and Kingery[93]
1070	0.783 theoretical	0	19.8	Vasilos and Kingery[93]
1173	0.783 theoretical	0	18.1	Vasilos and Kingery[93]

TABLE 56. SILICON CARBIDE THERMAL EXPANSION MEASUREMENTS

Temperature	Thermal Strain (10^{-3} m/m)	Sample	Reference
473	0.70	--	Fulkerson[75]
673	1.62	--	Fulkerson[75]
873	2.55	--	Fulkerson[75]
1073	3.60	--	Fulkerson[75]
1273	4.61	--	Fulkerson[75]
1473	5.47	--	Fulkerson[75]
1593	5.85	--	Fulkerson[75]
573	1.05	recrystallized (heating element)	Whittemore and Ault[95]
873	2.47	recrystallized (heating element)	Whittemore and Ault[95]
1173	3.94	recrystallized (heating element)	Whittemore and Ault[95]
1473	5.64	recrystallized (heating element)	Whittemore and Ault[95]
1773	7.67	recrystallized (heating element)	Whittemore and Ault[95]
573	0.99	clay-bonded	Whittemore and Ault[95]
873	2.70	clay-bonded	Whittemore and Ault[95]
1173	4.29	clay-bonded	Whittemore and Ault[95]
1473	5.99	clay-bonded	Whittemore and Ault[95]
1773	8.26	clay-bonded	Whittemore and Ault[95]
573	1.38	bonded glazed brick	Whittemore and Ault[95]
873	2.93	bonded glazed brick	Whittemore and Ault[95]
1173	4.55	bonded glazed brick	Whittemore and Ault[95]
1473	6.46	bonded glazed brick	Whittemore and Ault[95]
1773	8.56	bonded glazed brick	Whittemore and Ault[95]

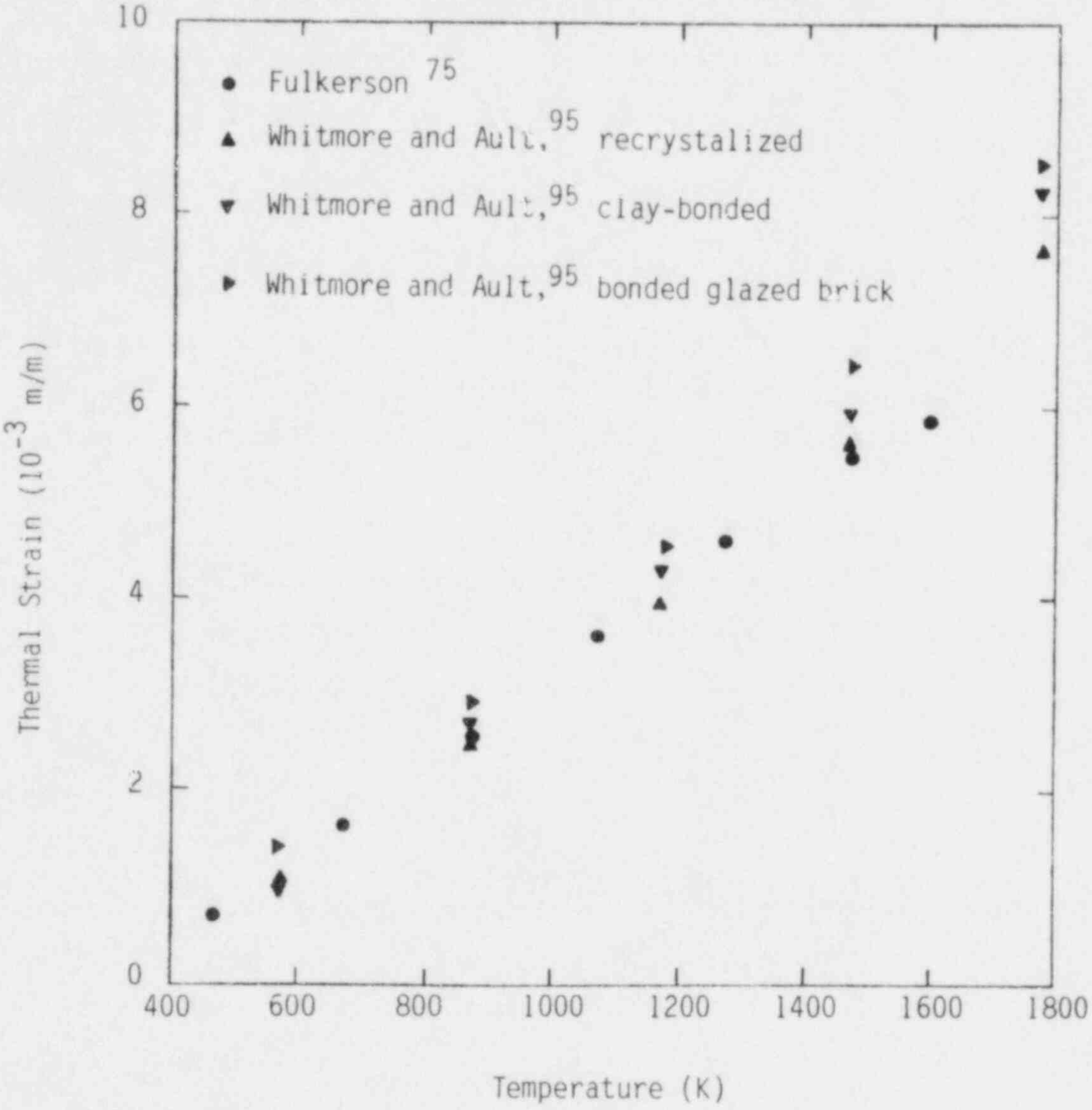

Figure 31. Silicon carbide thermal strains with a reference temperature of 298 K.

The heats of fusion and vaporization of silicon carbide are not needed because the compound decomposes near 2970 K.

2.5.2 Mechanical Properties

The only first-reference mechanical property data that have been found are some measurements by Price[96] of the change in Young's modulus and the modulus of rupture with neutron irradiation and some bend test data reported by General Atomic Company.[97] Unfortunately, Price reports only the ratios of the moduli in the irradiated state to those in the unirradiated state so his data are not yet useful. General Atomic reports average moduli of rupture of 2.3602 x 10^8, 2.5472 x 10^8, and 2.6700 x 10^8 Pa for four-point bend test loading rates of 5.1 x 10^4, 5.12 x 10^5, and 5.12 x 10^6 Pa/s (Table 3-2 of Reference 98). The tests were conducted at 295 K in air.

Data from references this author is unable to obtain are available in Lynch.[90] He reports measured moduli of elasticity of 2.1 x 10^{11}, 4.1 x 10^{11}, 4.8 x 10^{11} and 4.8 x 10^{11} Pa; Poisson's ratios of 0.19 and 0.24; compressive strengths of 1.4 x 10^9 and 1.4 x 10^9 Pa; and tensile strengths of 3.4 x 10^7 to 1.4 x 10^8 Pa at room temperature.

2.5.3 Electromagnetic Properties

Chiochetti and Henry[100] have reported values of resistivity for a silicon carbide refractory brick with an apparent porosity of 0.12. Their data are reproduced in Table 57 and plotted on semi-logarithmic axis in Figure 32. The data are remarkable because they do not define a straight line on the simi-log plot. Another feature of the available silicon carbide electrical resistivity data is the very low resistivities obtained in measurements on single crystals of carbide at low (80 to 340 K) temperatures.[89] The low temperature data which show resistivities three orders of magnitude smaller than those of Figure 32 are not reproduced because the original reference was not available.

TABLE 57. SILICON CARBIDE RESISTIVITY MEASURED BY CHIOCHETTI AND HENRY[100]

Temperature (K)	Resistivity (ohm•m)
923	872
1002	563
1089	358
1237	172
1407	74
1496	45
1685	16

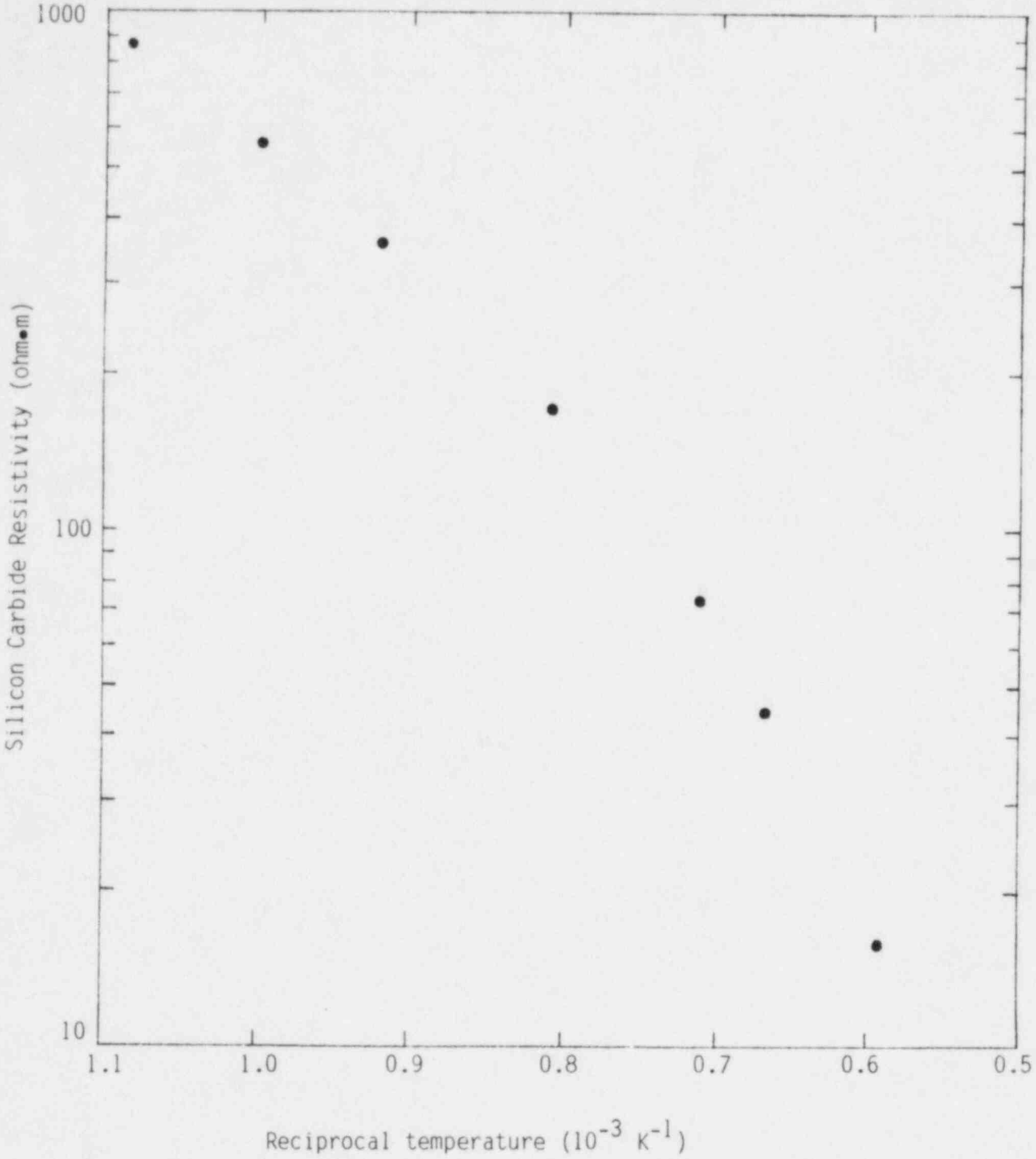

Figure 32. Resistivity of a silicon carbide sample according to Chiochetti and Henry[100].

2.5.4 Physical/Chemical Properties

The silicon carbide properties that will be discussed are the decomposition temperature, density, hydrogen isotope permeability, hydrogen isotope diffusion rates, hydrogen isotope solubility, hydrogen isotope reflection coefficients, hydrogen isotope trapping coefficient data, hydrogen isotope sputtering yields, corrosion rates and activation product decay times.

Goldsmith[89] reports a decomposition temperature of 2970 K for silicon carbide. This is lower than the melting temperature of the solid. The theoretical density of alpha phase silicon carbide is reported by Lynch[90] to be 3218 kg/m^3, presumably at room temperature.

The only source of data on the permeability, diffusion rates and solubility of hydrogen isotopes in silicon carbide that has been found is Verchese et al.[101] Unfortunately, their permeability data were changed from the values measured at 5 x 10^3 to 18 x 10^3 Pa to calculated values at 1.013 x 10^5 Pa assuming a square-root pressure dependence. Since the published permeabilities are therefore not measurements, they are not reproduced. The reader is advised to use the best fit correlation for permeability recommended by Verghese et al. until a data base is available. The their expression is

$$K = \left\{ 2.787 \times 10^{29} \right\} \exp - \left\{ \frac{66750}{T} \right\} \qquad (10)$$

where

K = the permeability of silicon carbide (H atoms - cm^{-1} - sec^{-1} - (10^3 Pa)$^{-0.5}$)

T = temperature (K).

Table 58 and Figure 33 illustrate the hydrogen diffusion coefficients in silicon carbide measured by Verghese et al. The coefficients are about two orders of magnitude lower than those for 316 stainless steel. However, the rather limited temperature range of the data and the fact that there is only one experiment suggests caution should be used in applying the data.

Table 59 and Figure 34 illustrate the limited solubility data for hydrogen in silicon carbide. Based on these data, Verghese et al. suggest that the solubility increases with decreasing temperature. This conclusion is too dependent on the single datum at 1424 K to be trusted very far.

Unfortunately, no data for hydrogen isotope reflection coefficients or trapping coefficients are available.

Surface sputtering yield data for several light isotopes are available in the literature[49,88,102] and are reproduced in Table 60. The yields are in the typical range of 10^{-3} to 10^{-2} atoms released per incident ion and are rather strongly dependent on the angle of incidence of the ion. Mohri et al.[102] find the yields at a 45-degree angle of incidence to be nearly an order of magnitude greater than those at a 90-degree angle of incidence.

Table 61 and Figure 35 are reproductions of the estimates of the radioactivity of typical silicon carbide samples published by Crocker and Holland.[55] The very rapid decrease of radioactivity with time for silicon carbide compared to most other first wall construction materials makes this material an attractive candidate for fusion reactors.

2.6 G-10 Insulation

Type G-10 insulation is a glass cloth reinforced epoxy insulation for superconducting magnets. The material is 0.007 mm diameter glass fibers woven on a conventional loom by interlacing warp (length) threads (16.9 ± 0.8/cm) and fill (width) threads (12.6 ± 0.8/cm).[103] The epoxy weight fraction is 0.32 to 0.36. The most obvious result of this woven construction is an isotopic materials properties.

TABLE 58. DIFFUSION COEFFICIENTS FOR HYDROGEN IN SILICON CARBIDE ACCORDING TO VERGHESE ET AL.[101]

Temperature (K)	Diffusion Coefficient (m^2/s)
1473	7.686×10^{-11}
1574	7.686×10^{-11}
1598	1.032×10^{10}
1622	3.183×10^{10}
1648	9.689×10^{-10}
1675	9.974×10^{-10}
1699	1.524×10^{-9}

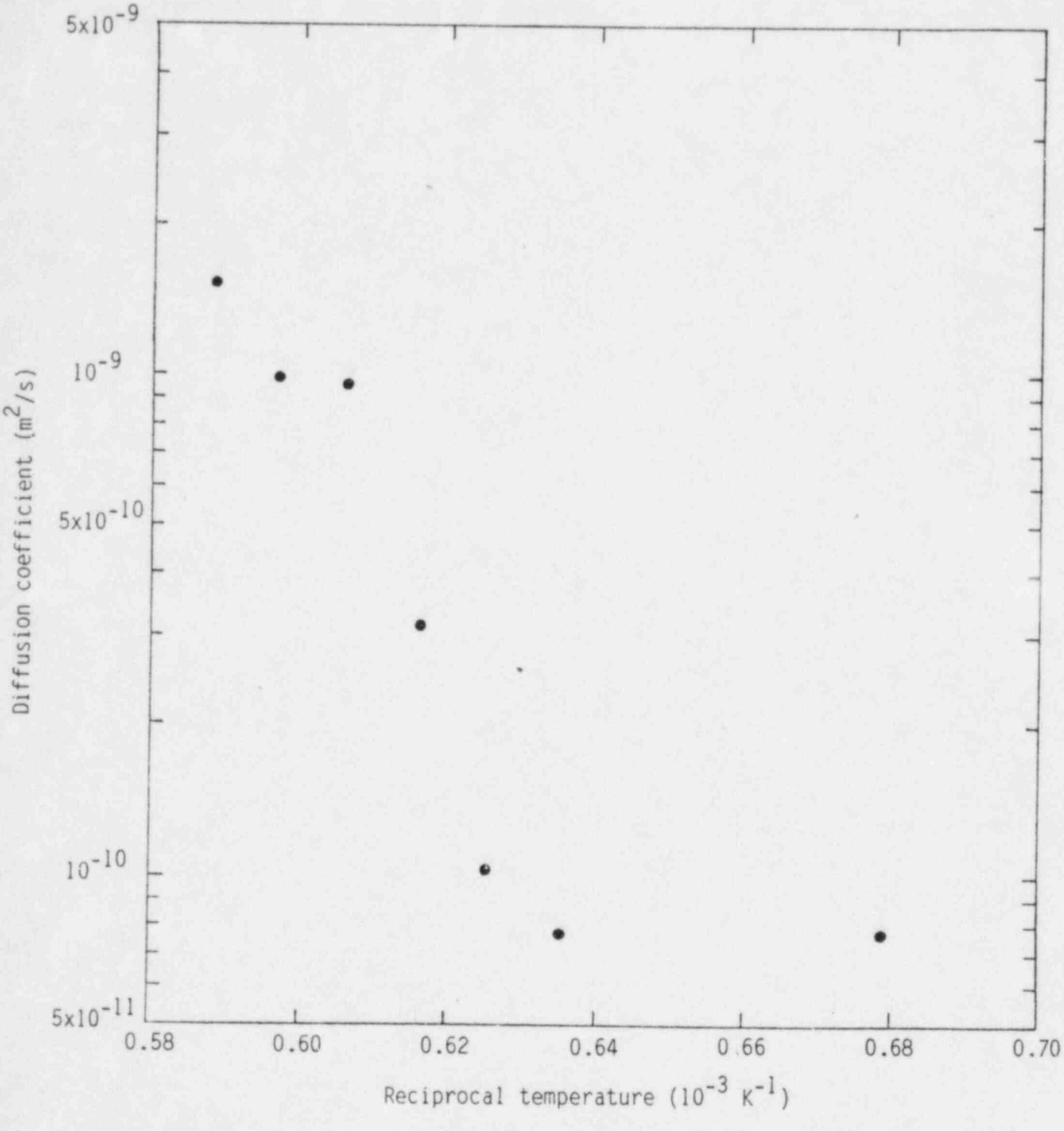

Figure 33. Hydrogen diffusion coefficients in silicon carbide measured by Verghese et al[101].

TABLE 59. SOLUBILITY OF HYDROGEN IN SILICON CARBIDE ACCORDING TO VERGHESE ET AL.[101]

Temperature (K)	Solubility (10^{24} H atoms/m^3)
1424	5.93
1524	4.27
1573	3.56
1574	2.36
1623	4.66
1678	3.91

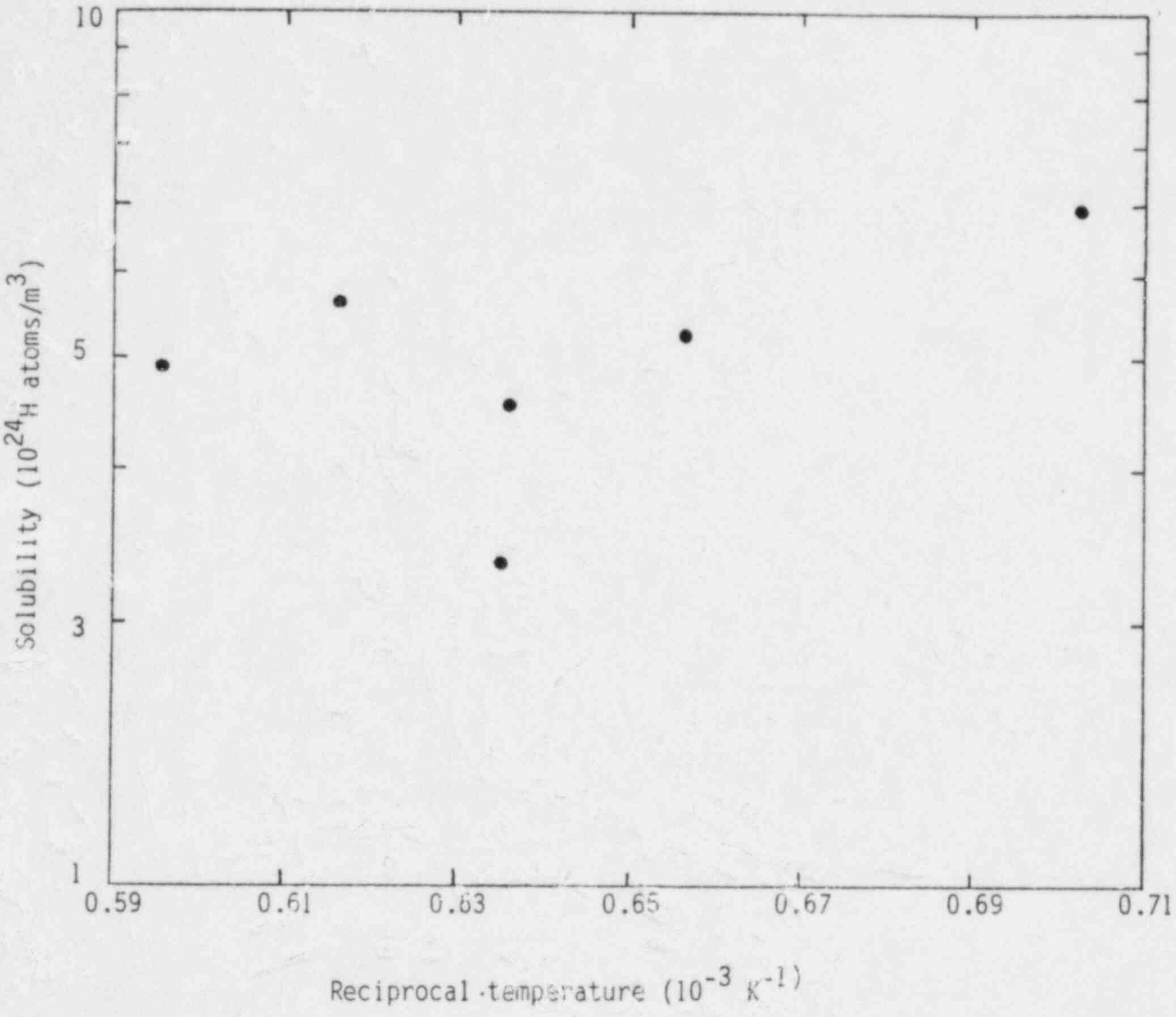

Figure 34. Hydrogen solubility in silicon carbide measured by Verghese et al.[101]

Table 60

TABLE 60. SPUTTERING YIELDS FROM SILICON CARBIDE SURFACES

Hydrogen Isotope	Target Material	Particle Energy (10^{-16} J)	Temperature (k)	Reference	Sputtering Yield
H_2^+	SiC	12	--	Behrisch et al.[49]	$(7 \pm 0.9) \times 10^{-3}$
H_2^+	SiC	8	--	Behrisch et al.[49]	9×10^{-3}
H_2^+	dense SiC	12	293	Roth et al.[88]	$(7 \pm 0.9) \times 10^{-3}$
H_2^+	dense SiC	8	293	Roth et al.[88]	9×10^{-3}
H_3^+	porous SiC	1.6	293	Roth et al.[88]	$(1.5 \pm 0.2) \times 10^{-2}$
H_3^+	porous SiC	1.6	808	Roth et al.[88]	2.1×10^{-2}
H_3^+	porous SiC	1.5	883	Roth et al.[88]	1.93×10^{-2}
H_1^+	SiC (90° incident)	16.	300	Mohri et al.[102]	5.67×10^{-3}
H_1^+	SiC (90° incident)	16.	326	Mohri et al.[102]	6.27×10^{-3}
H_1^+	SiC (90° incident)	16.	457	Mohri et al.[102]	5.65×10^{-3}
H_1^+	SiC (90° incident)	16.	652	Mohri et al.[102]	7.42×10^{-3}
H_1^+	SiC (90° incident)	16.	722	Mohri et al.[102]	5.36×10^{-3}
H_1^+	SiC (90° incident)	16.	822	Mohri et al.[102]	6.76×10^{-3}
H_1^+	SiC (90° incident)	16.	1024	Mohri et al.[102]	4.79×10^{-3}
H_1^+	SiC (90° incident)	16.	1073	Mohri et al.[102]	7.10×10^{-3}
H_1^+	SiC (90° incident)	16.	1275	Mohri et al.[102]	4.86×10^{-3}
H_1^+	SiC (90° incident)	16.	1374	Mohri et al.[102]	4.49×10^{-3}
H_1^+	SiC (45° incident)	16.	296	Mohri et al.[102]	2.62×10^{-2}
H_1^+	SiC (45° incident)	16.	301	Mohri et al.[102]	1.80×10^{-2}
H_1^+	SiC (45° incident)	16.	560	Mohri et al.[102]	3.58×10^{-2}
H_1^+	SiC (45° incident)	16.	678	Mohri et al.[102]	2.91×10^{-2}
H_1^+	SiC (45° incident)	16.	853	Mohri et al.[102]	5.55×10^{-2}
H_1^+	SiC (45° incident)	16.	962	Mohri et al.[102]	5.06×10^{-2}

Table 60 (continued)

TABLE 60. (continued)

Hydrogen Isotope	Target Material	Particle Energy (10^{-16} J)	Temperature (k)	Reference	Sputtering Yield
H_1^+	SiC (45° incident)	16.	1095	Mohri et al.[102]	6.85×10^{-2}
H_1^+	SiC (45° incident)	16.	1260	Mohri et al.[102]	5.15×10^{-2}
He^+	SiC (90° incident)	16.	299	Mohri et al.[102]	2.85×10^{-2}
He^+	SiC (90° incident)	16.	313	Mohri et al.[102]	2.24×10^{-2}
He^+	SiC (90° incident)	16.	663	Mohri et al.[102]	2.82×10^{-2}
He^+	SiC (90° incident)	16.	966	Mohri et al.[102]	4.69×10^{-2}
He^+	SiC (90° incident)	16.	1221	Mohri et al.[102]	4.15×10^{-2}
He^+	SiC (90° incident)	16.	1278	Mohri et al.[102]	4.44×10^{-2}
He^+	SiC (90° incident)	16.	1377	Mohri et al.[102]	7.02×10^{-2}
Ar^+	SiC (90° incident)	16.	299	Mohri et al.[102]	3.19×10^{-1}
Ar^+	SiC (90° incident)	16.	958	Mohri et al.[102]	4.26×10^{-1}
Ar^+	SiC (90° incident)	16.	1036	Mohri et al.[102]	4.44×10^{-1}

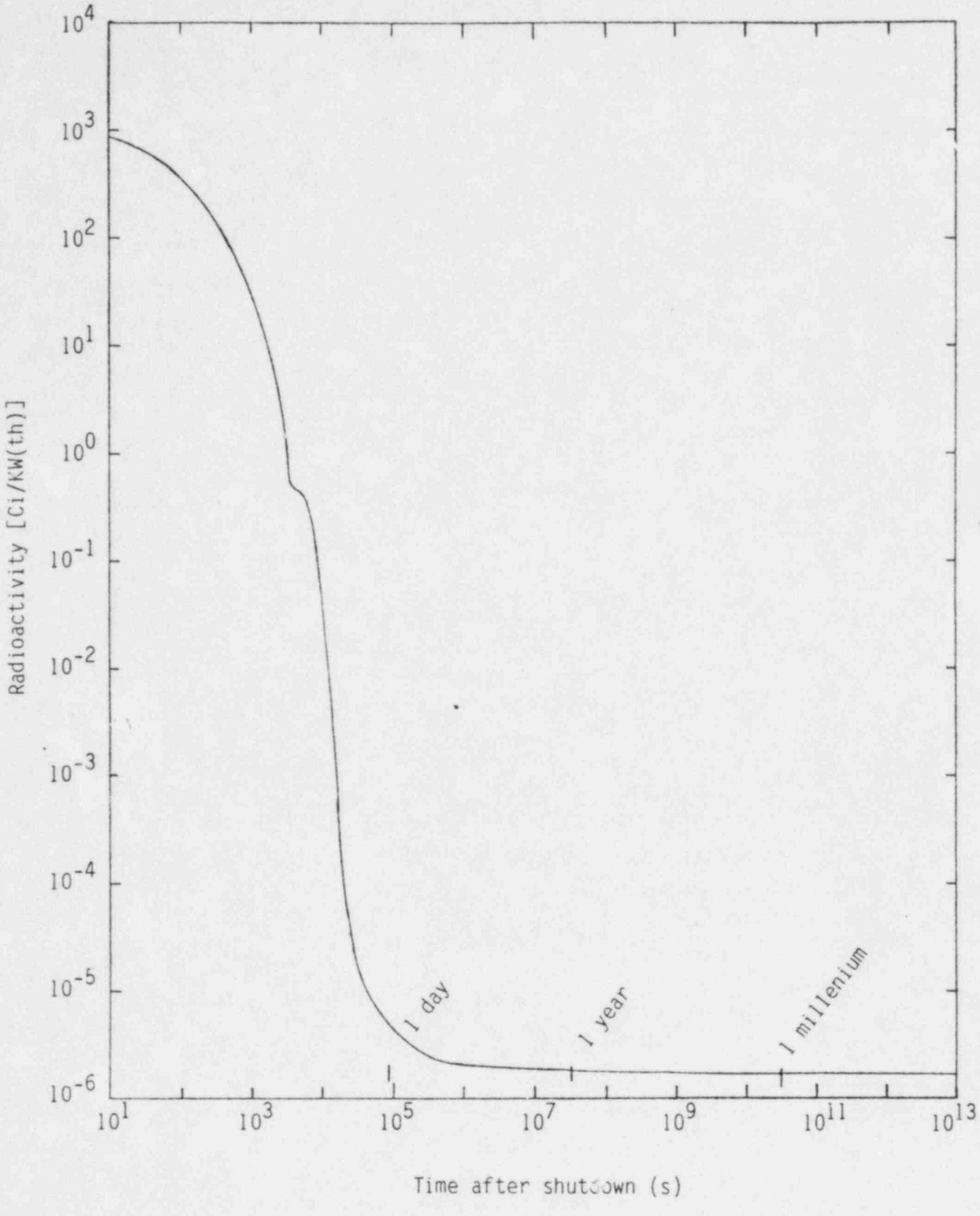

Figure 35. Radioactivity of silicon carbide after shutdown according to Crocker and Holland.[55]

TABLE 61. RADIOACTIVITY OF SILICON CARBIDE AFTER SHUTDOWN ACCORDING TO CROCKER AND HOLLAND[55]

Time After Shutdown (s)	Radioactivity (Ci/kW (th)
1.00×10^{1}	8.56×10^{2}
2.47×10^{1}	7.52×10^{2}
7.67×10^{1}	4.20×10^{2}
2.16×10^{2}	2.03×10^{2}
5.17×10^{2}	8.52×10^{1}
9.25×10^{2}	3.14×10^{1}
1.50×10^{3}	1.27×10^{1}
2.29×10^{3}	4.27
3.06×10^{3}	1.36
3.37×10^{3}	6.44×10^{-1}
4.37×10^{3}	4.97×10^{-1}
6.04×10^{3}	3.88×10^{-1}
6.44×10^{3}	2.88×10^{-1}
8.34×10^{3}	1.05×10^{-1}
1.08×10^{4}	2.46×10^{-2}
1.36×10^{4}	3.52×10^{-3}
1.70×10^{4}	5.03×10^{-4}
2.06×10^{4}	8.20×10^{-5}
2.20×10^{4}	4.88×10^{-5}
2.35×10^{4}	2.80×10^{-5}
3.25×10^{4}	1.56×10^{-5}
4.78×10^{4}	7.95×10^{-6}
8.03×10^{4}	5.53×10^{-6}
1.07×10^{5}	4.16×10^{-6}
2.26×10^{5}	2.93×10^{-6}
3.67×10^{5}	2.48×10^{-6}
1.03×10^{6}	2.07×10^{-6}
1.85×10^{6}	1.96×10^{-6}
1.72×10^{7}	1.91×10^{-6}
6.44×10^{8}	1.82×10^{-6}
1.21×10^{11}	1.70×10^{-6}
3.29×10^{12}	1.68×10^{-6}
1.00×10^{13}	1.62×10^{-6}

2.6.1 Thermal Properties

The only thermal property for which usable data have been found is the thermal conductivity. Data for specific heat capacity, thermal expansion and emissivity may be available in a handbook by Fickett, Reed and Dalder[104] but the author has been unable to locate a copy.

Table 62 is a reproduction of the thermal conductivity of several G-10 insulation samples measured by Hust.[105] Most of the data are reproduced in Figure 36, which shows that the conductivity normal to the threads is significantly lower than the conductivity in the warp direction. A probable trend for conductivity to increase with increasing density of the various samples is also shown by the data. Hust published additional thermal conductivity data from a piece of the G-10C4 sample that had been strained. The data indicate that the effects of small strains on thermal conductivity is not large.

2.6.2 Mechanical Properties

Some data on the mechanical properties of G-10 insulation are available, but they are far from complete. Like all other properties for this material, they are a function of direction.

Schramm and Kasen[106] and Ledbetter[107] have reported the limited elastic moduli data shown in Tables 63 and 64. The data of Schramm and Kasen are static moduli while those of Ledbetter are dynamic moduli but they differ very little. A noticable variation with direction in the warp-fill plane is present and a large change with the angle to this plane is indicated. In addition, Ledbetter concludes that the classical expressions for the effect of texture in homogeneous material can be applied to composites like G-10 insulation. Unfortunately, neither Schramm and Kasen nor Ledbetter reports the density of the samples they measured.

TABLE 72. THERMAL CONDUCTIVITY OF G-10 INSULATION SAMPLES ACCORDING TO HUST[105]

Temperature (K)	Density (kg/m^3)	Direction	Conductivity (W/m•K)	Sample Number
2.11	1904	normal to threads	0.0253	G-10C1
2.52	1904	normal to threads	0.0340	G-10C1
3.02	1904	normal to threads	0.0429	G-10C1
3.99	1904	normal to threads	0.0438	G-10C1
5.99	1904	normal to threads	0.0803	G-10C1
7.95	1904	normal to threads	0.0816	G-10C1
9.85	1904	normal to threads	0.108	G-10C1
14.9	1904	normal to threads	0.135	G-10C1
19.7	1904	normal to threads	0.150	G-10C1
29.9	1904	normal to threads	0.185	G-10C1
39.6	1904	normal to threads	0.214	G-10C1
59.8	1904	normal to threads	0.266	G-10C1
79.3	1904	normal to threads	0.312	G-10C1
98.6	1904	normal to threads	0.345	G-10C1
147.	1904	normal to threads	0.401	G-10C1
199.	1904	normal to threads	0.456	G-10C1
246.	1904	normal to threads	0.497	G-10C1
292.	1904	normal to threads	0.521	G-10C1
2.09	1904	Warp	0.0364	G-10C1
2.49	1904	Warp	0.0458	G-10C1
3.01	1904	Warp	0.0562	G-10C1
3.98	1904	Warp	0.0745	G-10C1
5.93	1904	Warp	0.102	G-10C1
7.92	1904	Warp	0.121	G-10C1
9.83	1904	Warp	0.137	G-10C1
14.9	1904	Warp	0.169	G-10C1
19.9	1904	Warp	0.194	G-10C1
29.8	1904	Warp	0.235	G-10C1
39.6	1904	Warp	0.281	G-10C1
59.5	1904	Warp	0.354	G-10C1
79.0	1904	Warp	0.429	G-10C1
98.4	1904	Warp	0.483	G-10C1
147	1904	Warp	0.605	G-10C1
196	1904	Warp	0.691	G-10C1
246	1904	Warp	0.767	G-10C1

TABLE 62. (continued)

Temperature (K)	Density (kg/m^3)	Direction	Conductivity (W/m•K)	Sample Number
293	1904	Warp	0.815	G-10C1
277	1741	normal to threads	0.417	G-10C3
75.0	1825	Warp	0.347	G-10C4
272.	1825	Warp	0.619	G-10C4
4.09	1720	Warp	0.0557	G-10C7
4.97	1720	Warp	0.0717	G-10C7
6.89	1720	Warp	0.0926	G-10C7
8.96	1720	Warp	0.105	G-10C7
13.9	1720	Warp	0.133	G-10C7
17.8	1720	Warp	0.147	G-10C7
24.8	1720	Warp	0.164	G-10C7
34.6	1720	Warp	0.193	G-10C7
49.9	1720	Warp	0.231	G-10C7
69.6	1720	Warp	0.276	G-10C7
88.6	1720	Warp	0.325	G-10C7
118	1720	Warp	0.380	G-10C7
166	1720	Warp	0.462	G-10C7
217	1720	Warp	0.520	G-10C7
293	1720	Warp	0.581	G-10C7

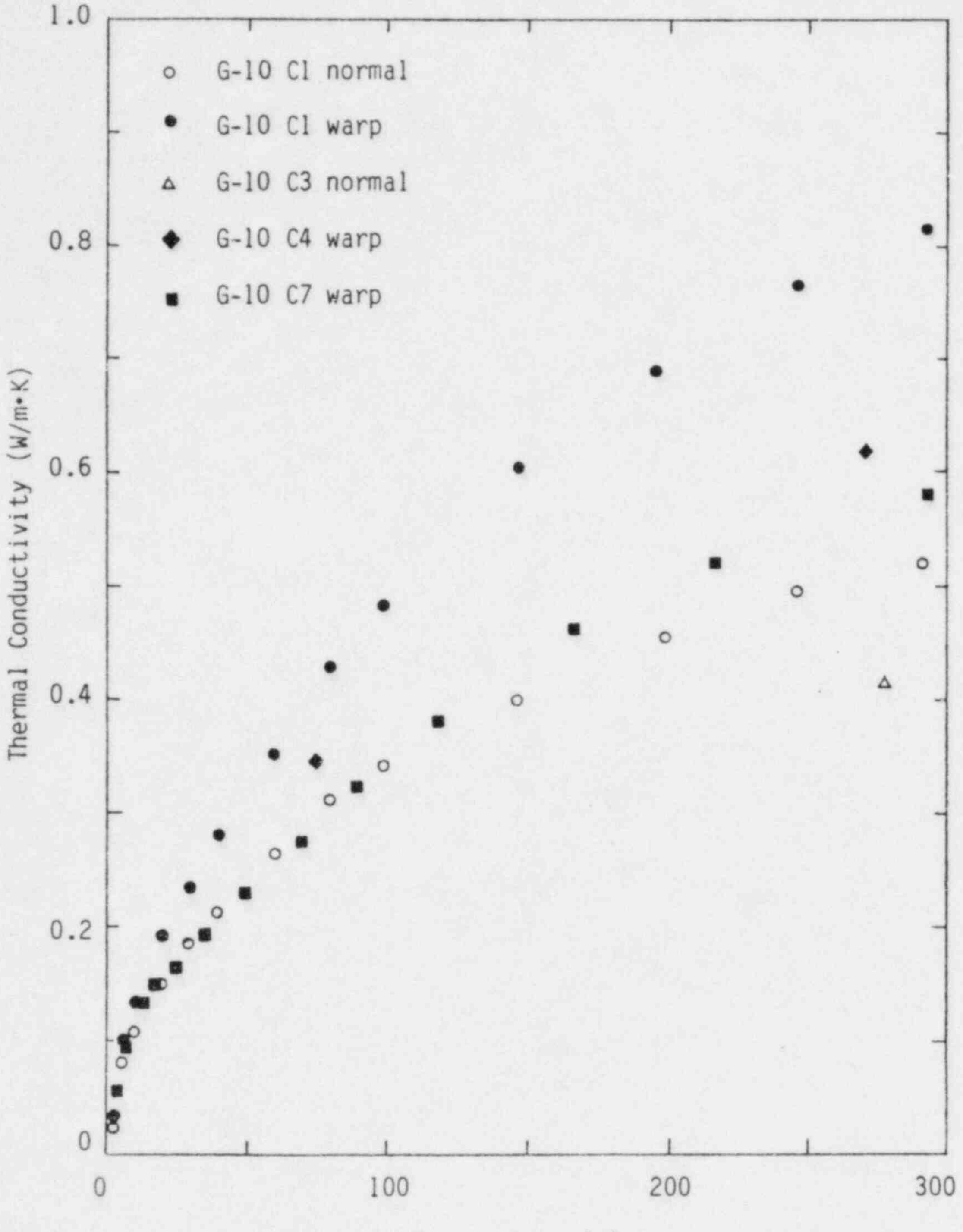

Figure 36. G-10 thermal conductivities measured by Hust[105].

TABLE 63. ELASTIC MODULI OF G-10 INSULATION SAMPLES ACCORDING TO SCHRAMM AND KASEN[106]

Temperature (K)	Density (kg/m^3)	Direction	Young's Modulus (10^9 Pa)	Poisson's Ratio	Sample No.
76	--	Warp	32.9	0.195	C
76	--	Warp	29.8	0.147	C
295	--	Warp	26.3	0.146	C
295	--	Warp	25.7	0.134	C
76	--	Warp	32.5	0.218	D
76	--	Warp	30.0	0.215	D
295	--	Warp	23.0	0.174	D
295	--	Warp	23.4	0.151	D

TABLE 64. ELASTIC MODULI OF G-10 INSULATION SAMPLES ACCORDING TO LEDBETTER[107]

Temperature (K)	Density (kg/m^3)	Direction	Young's Modulus (10^9 Pa)
295	--	Warp	29.4±1.0
295	--	fill	26.3±1.0
295	--	normal	14.0
295	--	fill-warp plane 15° from fill	22.7
295	--	fill-warp plane 30° from fill	18.6
295	--	fill-warp plane 45° from fill	17.5
295	--	fill-warp plane 60° from fill	19.0
295	--	fill-warp plane 75° from fill	24.2

The available plastic deformation data are usable for general guidance but not sufficient to define the equation of state that is needed for modeling deformation. Table 65 is a summary of the tensile strengths, compressive strengths and strains to failure for G-10 samples at liquid nitrogen and room temperatures reported by Schramm and Kasen.[106] Two other sources of data have been found. Fickett, Reed and Dalder[104] report normal direction compressive strengths of $744 \pm 85 \times 10^6$, $692 \pm 35 \times 10^6$, and $411 \pm 35 \times 10^6$ Pa at 7.6, 76 and 292 K. (The 7.6 K and 292 K are probably mis-plotted representations of 4.2 K and 295 K, the temperatures of liquid helium and typical rooms.) Kernohan, Long and Coltman[108] report compressive strengths of 602 and 837×10^6 Pa at 77 K for unirradiated material. Unfortunately, they did not publish orientation information. Companion samples which had been irradiated at liquid helium temperatures to a total gamma dose of 2×10^9 rad showed compressive strengths of only 225 and 237×10^6 Pa at 77 K.

Figure 37 is a plot of the compressive strength data. The outstanding feature shown by the plot is the factor or 0.7 decrease in compressive strength of the irradiated G-10 sample.

Since no data are available to define an equation of state for G-10 deformation, models will have to be crude estimates obtained from a power law fit to either tensile or compressive strengths which are assumed to occur near the failure strains given in Table 65. The tensile and compressive strengths would thus be an estimated failure stress too.

The only cyclic fatigue data that have been found are some peak stress versus number of cycles results together with an indication of whether or not the sample failed which have been reported by Erez and Becker.[109] Since these data do not help define the constants in the crack propagation equation, Equation (9), the data are not very useful.

No data about irradiation growth, swelling or fracture toughness of G-10 insulation have been found.

TABLE 65. G-10 PLASTIC DEFORMATION DATA FROM SCHRAMM AND KASEN[106]

Temperature (K)	Density (kg/m^3)	Direction	Tensile Strength (10^6 Pa)	Compressive Strength (10^6 Pa)	Strain to Failure (m/m)	Sample Number
76	--	Warp	763	733	0.0240	C
76	--	Warp	721	665	0.0284	C
295	--	Warp	410	342	0.0177	C
295	--	Warp	394	337	0.0247	C
76	--	Warp	877	698	0.0331	D
76	--	Warp	839	794	0.0291	D
295	--	Warp	454	395	0.0179	D
295	--	Warp	477	360	0.0256	D

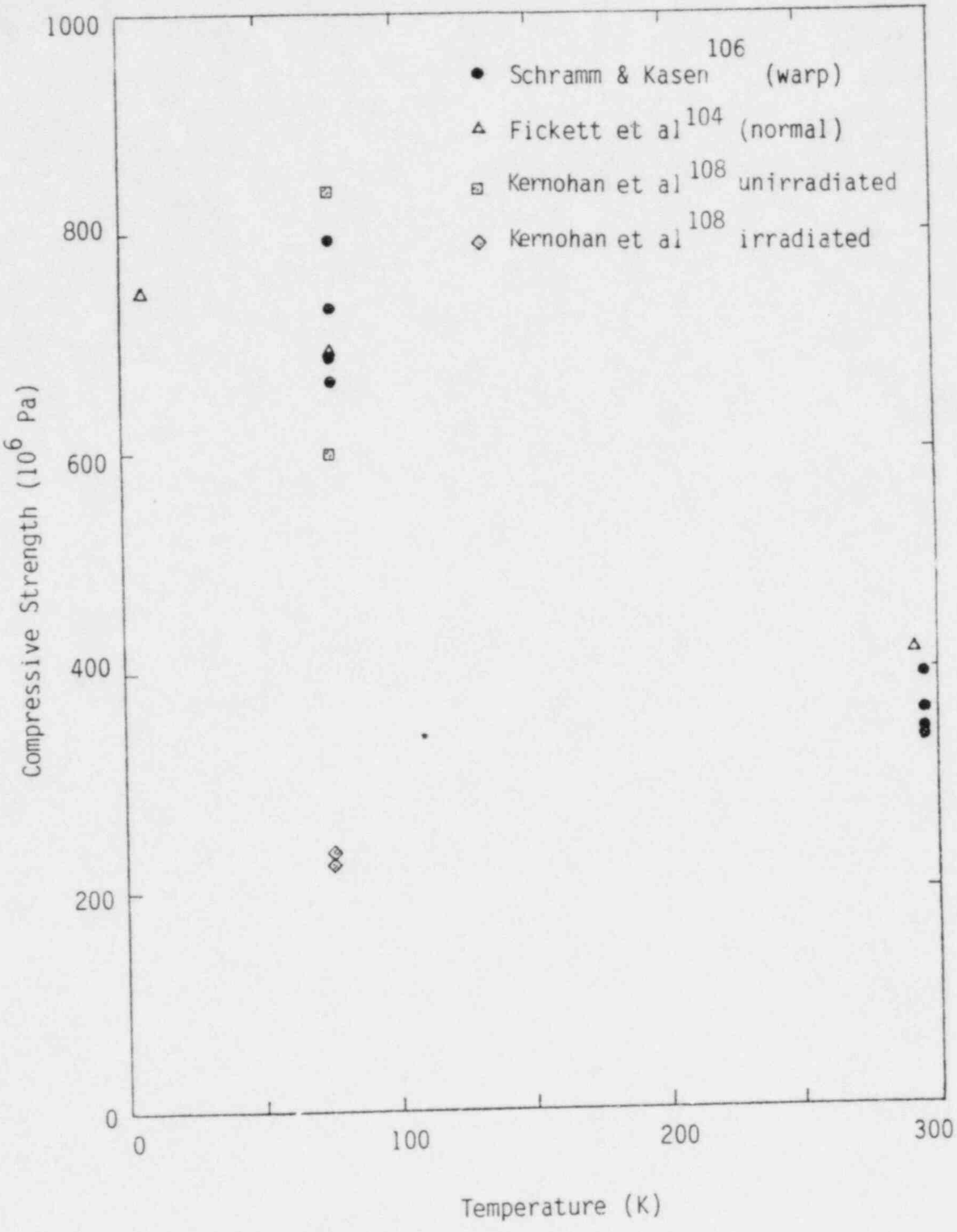

Figure 37. Compressive strength of G-10 insulation.

2.6.3 Electromagnetic Properties

The electrical resistivity of G-10 insulation has been reported by Kernohan et al.[108] to be 7×10^{13} ohm•m at room temperature for both irradiated and unirradiated samples. These authors also report a break-down field of 22×10^{6} V/m for both irradiated and unirradiated samples.

3. MATERIALS PROPERTIES PACKAGE DESIGN

This section discusses how the data reviewed in Section 2 might be collected into a package that can be used to support fusion reactor analysis. Experience with Light Water Reactor safety analysis has shown that many but not all users of such a package will be employing computer programs which should be able to rely on a standard set of subprograms to describe the materials employed. This experience has also shown that a materials properties package should be structured so that it can act as a convenient collecting site for new data (i.e., the package should be designed for easy change as new alloys are developed) and that it should have sufficient documentation to make it a target for knowledgeable criticism.

The package design presented in this section is a computer library consisting of separate subroutines or functions and detailed model descriptions consisting of a separate appendix for each material and a separate section for each property. Both documentation and computer programs can thus be changed property-by-property as the need arises.

Each section of each appendix of the documentation needs to have a summary, a review of literature and data, a description of the model development and a computer subcode listing with plots of the output generated by the listing. Appendix A of this report is an example of the documentation for one property of one material, hydrogen diffusion coefficients in 316 stainless steels.

The summary contains the main equations or tables of values used to describe the property, a description of the key parameters and an estimate of the model's uncertainty. The summary thus serves a purpose similar to materials properties handbooks like References 1 through 7. It provides a quick reference for users who simply want a value for the property.

The review of literature and data contains not only all references but a critical review and comparison of these references in order to determine which sources are appropriate to use for fusion reactors and which are not. This section provides confidence in the data used to generate equations presented in the summary, allows constructive criticism of the model, and makes subsequent improvement of the model much easier.

The model development subsection tells what was done with the data to arrive at the equations in the summary. The section invites knowledgeable criticism of the model, promotes confidence in the model, and justifies the uncertainty limits assigned to the model.

The computer subcode listing section provides a standard listing of the coding that is recommended to incorporate the equations in the summary. This avoids unnecessary duplication of coding effort by different users and provides completely consistent materials descriptions to support complex computer analysis. A computer generated plot confirms the accuracy of the coding and provides the user with a pictorial representation of the values calculated with the equations in the summary.

Comparison of the example materials properties documentation section in Appendix A with the discussion of hydrogen diffusion coefficients in Section 2.1.4 leads to an important recommendation. The time spent finding references for diffusion in vanadium, graphite, and silicon carbide yielded references for diffusion in stainless steels which were not known when Section 2.1.4 was written. This slow but steady accumulation and improvement in knowledge of available literature has been noticeable during the development of Light Water Reactor materials properties and strongly suggests that a small, long-term effort would be more beneficial than a short, high intensity effort to develop materials properties packages for fusion reactors.

The author is certain that starting this effort now, even at a low level will save a lot of needless duplication and confusion in fusion reactor analysis computer codes later. In fact, development of a fusion reactors materials property package should have already begun because several computer programs which should be using such a package are already under development without the package.[40,110,111]

4. REFERENCES

1. D. Peckner and I. M. Bernstein (eds.), *Handbook of Stainless Steels*, New York: McGraw-Hill Book Company, TA479 S7H28.

2. T. C. Chawla et al., *Thermophysical Properties of Mixed Oxide Fuel and Stainless Steel Type 316 for Use in Transition Phase Analysis*, ANL/RAS 81-16, April 1981.

3. H. C. Brassfield et al., *Recommended Property and Reaction Kinetics Data for Use in Evaluating a Light Water Cooled Reactor Incident Involving Zircaloy-4 or 304 SS Cladd UO_2*, GEMP 482, April 1968.

4. W. B. Murfin et al., *Core-Meltdown Experimental Review*, SAND 74-0382, 1977.

5. I. Catton et al., *Post-Accident Core Retention for LMFBRs*, UCLA-ENG-7343, July 1973.

6. Analysis and Evaluation Task Group of the United States Department of Energy Office of Fusion Energy, *Materials Handbook for Fusion Energy Systems*, DOE/TIC-10122, with updates 1-4 (to August 18, 1982).

7. L. Leibowitz et al., *Properties for LMFBR Safety Analysis*, ANL-CEN-RSD-76-1, March 1976.

8. W. C. Rion, Jr. (compiler), *Stainless Steel Information Manual for the Savannah River Plant, Vol. 1 Properties*, DP-860-1, July 1964.

9. J. C. Spanner (ed.), *Nuclear Systems Materials Handbook--Volume 1, Design Data*, TID-26666, 1976.

10. P. J. Barton and P. R. B. Higgins, "Some Observations on the Structure and Tensile Properties of AISI Type 316 Steel as a Function of Fast Reactor Irradiation Temperature," *Irradiation Effects on Structural Alloys for Nuclear Reactor Applications*, ASTM STP 484, 1970, pp. 362-374.

11. E. E. Bloom and F. W. Wiffen, "The Effects of Large Concentrations of Helium on the Mechanical Properties of Neutron-Irradiated Stainless Steel," *Journal of Nuclear Materials 58*, 1975, pp. 171-184.

12. E. E. Bloom, "Mechanical Properties of Materials in Fusion Reactor First-Wall and Blanket Systems," *Journal of Nuclear Materials 85 and 86*, 1979, pp. 795-804.

13. P. Fenici et al., "Influence of Lithium and Lithium Plus Lithium Hydride Exposures on the Uniaxial Tensile Properties of AISI 316 and 304 Type Stainless Steels," *Journal of Nuclear Materials 85 and 86*, 1979, pp. 277-281.

14. R. H. Jones et al., "Microstructure and Tensile Properties of T (d,n) and Be (d,n) Neutron Irradiated Nickel, Niobium and 316 SS," Journal of Nuclear Materials 85 and 86, 1979, pp. 889-893.

15. M. L. Grossbeck and P. J. Maziasz, "Tensile Properties of Type 316 Stainless Steel Irradiated in a Simulated Fusion Reactor Environment," Journal of Nuclear Materials 85 and 86, 1979, pp. 883-887.

16. G. R. Odette and D. Frey, "Development of Mechanical Property Correlation Methodology for Fusion Environments," Journal of Nuclear Materials 85 and 86, 1979, pp. 817-822.

17. V. K. Sikka and S. A. David, "Discontinuous Creep Deformation in an Type 316 Stainless Steel Casting," Metallurgical Transactions 12A, 1981, pp. 883-892.

18. A. J. Lovell and R. W. Barker, "Uniaxial and Biaxial Creep Rupture of Type 316 Stainless Steel After Fast Reactor Irradiation," Irradiation Effects on Structural Alloys for Nuclear Reactor Applications, ASTM STP 484, 1970, pp. 468-483.

19. R. F. Mattas et al., "Evaluation of Materials for EPR Power Generation," Journal of Nuclear Materials 85 and 86, 1979, pp. 171-175.

20. D. J. Michel et al., "Effects of Irradiation on Fatigue and Crack Propagation," Radiation Effects in Breeder Reactor Structural Materials, 1977, pp. 117-137.

21. J. M. Beeston and C. R. Brinkman, "Axial Fatigue of Irradiated Stainless Steels Tested at Elevated Temperatures," Irradiated Effects on Structural Alloys for Nuclear Reactor Applications, ASTM STP 484, 1970, pp. 419-450.

22. D. J. Michel and H. H. Smith, "Neutron Irradiation Effects on Fatigue Crack Propagation in Austenitic Stainless Steels and Nicket-Base Alloys," Journal of Nuclear Materials 85 and 86, 1979, pp. 845-849.

23. N. Nagata et al., "Low Cycle Fatigue Behavior of Blanket Structural Materials," Journal of Nuclear Materials 85 and 86, 1979, pp. 839-843.

24. R. E. Gold et al., "Materials Technology for Fusion: Current Status and Future Requirements," Nuclear Technology/Fusion 1, April 1981, pp. 169-237.

25. F. W. Wiffen and E. E. Bloom, "Effect of High Helium Content on Stainless-Steel Swelling," Nuclear Technology 25, January 1975, pp. 113-123.

26. M. R. Hayns et al., "The Derivation of a Simple Void-Swelling Equation for Cold-Worked 316 Austenitic Steel," Journal of Nuclear Materials 78, 1978, pp. 236-253.

27. J. F. Bates, "The Effects of Temperature Changes on the Swelling of AISI 316," *Journal of Nuclear Materials 98*, 1978, pp. 71-85.

28. H. R. Brager and F. A. Garner, "Comparison of the Swelling and Microstructural/Microchemical Evolution of AISI 316 Irradiated in EBR-II and HFIR," *Journal of Nuclear Materials 103 and 104*, 1981, pp. 993-998.

29. F. R. Fickett et al., "Structures, Insulators and Conductors for Large Superconducting Magnets," *Journal of Nuclear Materials 85 and 86*, 1979, pp. 353-360.

30. J. T. Stanley, "Magnetic Properties of Irradiated Austenitic Stainless Steel," *Journal of Nuclear Materials 85 and 86*, 1979, pp. 787-791.

31. V. A. Maroni and E. H. Van Deventer, "Materials Considerations in Tritium Handling Systems," *Journal of Nuclear Materials 85 and 86*, 1979, pp. 257-269.

32. J. H. Austin and T. S. Elleman, "Tritium Diffusion in 304- and 316-Stainless Steels in the Temperature Range 25 to 222°C," *Journal of Nuclear Materials 43*, 1972, pp. 119-125.

33. K. L. Wilson and M. I. Baskes, "Deuterium Trapping in Irradiated 316 Stainless Steel," *Journal of Nuclear Materials 76 and 77*, 1978, pp. 291-297.

34. R. D. Calder et al., "Grain Boundary Diffusion of Tritium in 304 and 316 Stainless Steel," *Journal of Nuclear Materials 46*, 1973, pp. 46-52.

35. F. Waelbroeck et al., "Hydrogen Solubilization into and Permeation Through Wall Materials," *Journal of Nuclear Materials 85 and 86*, 1979, pp. 345-349.

36. W. A. Swansiger and R. Bastasz, "Tritium and Deuterium Permeation in Stainless Steels: Influence of Thin Oxide Films," *Journal of Nuclear Materials 85 and 86*, 1979, pp. 335-339.

37. R. W. Conn and J. Kesner, "Plasma Modeling and First Wall Interaction Phenomena in Tokamaks," *Journal of Nuclear Materials 63*, 1976, pp. 1-14.

38. G. W. Look and M. I. Baskes, "Hydrogen Profiles in Tokamak Fusion Reactor First Walls, *Journal of Nuclear Materials 85 and 86*, 1979, pp. 995-999.

39. K. L. Wilson, "Hydrogen Recycling Properties of Stainless Steel," *Journal of Nuclear Materials 103 and 104*, 1981, pp. 453-464.

40. P. Wienhold et al, "Computer Code PERI for the Calculation of Recycling, Volume Distribution, and Permeation of Hydrogen in First Wall Materials of Tokamaks," *Journal of Nuclear Materials 93 and 94*, 1980, pp. 866-870.

41. W. Eckstein et al., "Reflection of Hydrogen from Stainless Steel and Nb," Journal of Nuclear Materials 63, 1976, pp. 199-204.

42. E. W. Thomas, "Retention and Re-Emission of 0.125-1-KeV Deuterium in Stainless Steel," Journal of Applied Physics 51, 1980, pp. 1176-1183.

43. N. J. Freeman et al., "Burial of 60 KeV Deuterium Ions in Stainless Steel and Titanium," Nature 212, 1966, pp. 1346-1347.

44. M. Braun et al., "Determination of Deuterium Surface Recombination Rates on Stainless Steeel," Journal of Nuclear Materials 93 and 94, 1980, pp. 861-865.

45. F. Waelbroeck et al., "Influence of the Wall Temperature on Hydrogen Recycling Phenomena in a SS Similation Apparatus," Journal of Nuclear Materials 103 and 104, 1981, pp. 471-476.

46. R. A. Kerst, "Surface Modification of 300 Series Stainless Steel by a Deuterium Plasma," Journal of Nuclear Materials 103 and 104, 1981, pp. 439-444.

47. P. Wienhold et al., "Comparison of Experimental Results and Numerical Calculations of Hydrogen Recycling from Stainless Steel," Journal of Nuclear Materials 93 and 94, 1980, pp. 540-541.

48. H. H. Anderson and H. L. Bay, "A Survey of Sputtering-Yield Data for Plasma-Wall Interactions Calculations," Journal of Nuclear Materials 93 and 94, 1980, pp. 625-633.

49. R. Behrisch et al., "Measurements of the Erosion of Stainless Steel, Carbon and SiC by Hydrogen Bombardment in the Energy Range of 0.5-7.5 KeV, Journal of Nuclear Materials 60, 1976, pp. 321-329.

50. J. Bohdansky, "Important Sputtering Yield Data for Tokamaks: A Comparison of Measurements and Estimates," Journal of Nuclear Materials 93 and 94, 1980, pp. 625-633.

51. P. Sigmund, "Theory of Sputtering. I. Sputtering Yield of Amorphous and Polycrystalline Targets," Physical Review 184, 1969, pp. 383-416 with errata in Physical Review 187, 1969, p. 768.

52. G. A. Whitlow et al., "Materials Behavior in Lithium Systems for Fusion Reactor Applications," Journal of Nuclear Materials 85 and 86, 1979, pp. 283-287.

53. P. F. Tortorelli and J. H. DeVan, "Thermal-Gradient Mass Transfer in Lithium-Stainless Steel Systems," Journal of Nuclear Materials 85 and 86, 1979, pp. 289-293.

54. W. C. Rion, Jr. (compiler), Stainless Steel Information Manual for the Savannah River Plant. Volume I--Properties, 1964, DP-860, Vol. I, Table 1.

55. J. G. Crocker and D. F. Holland, "Safety and Environmental Issues of Fusion Reactors," Proceedings of the IEEE 69. August 1981, pp. 968-976.

56. Y. S. Touloukian and C. Y. Ho, Properties of Selected Ferrous Alloying Elements, New York: McGraw-Hill Book Company, 1981.

57. M. B. Reynolds, "The Determination of the Elastic Constants of Metals by the Ultrasonic Pulse Technique," Transactions of the American Society for Metals 45, 1953, pp. 839-861.

58. G. E. Korth and R. E. Schmunk, "Low-Cycle Fatigue of Three Irradiated and Unirradiated Vanstar Alloys," Effects of Radiation on Structural Materials, ASTM STP 683, 1979, pp. 466-476.

59. M. P. Tanaka, E. E. Bloom and J. A. Horak, "Tensile Properties and Microstructure of Helium Injected and Reactor Irradiated V-20 Ti," Journal of Nuclear Materials 103 and 104, 1981, pp. 895-900.

60. E. R. Bradley and R. H. Jones, "Strength Changes in Vanadium and Titanium Irradiated with 14 MeV Neutrons," Journal of Nuclear Materials 103 and 104, 1981, pp. 901-906.

61. R. E. Gold and D. L. Harrod, "Refractory Metal Alloys for Fusion Reactor Applications," Journal of Nuclear Materials 103 and 104, 1981, pp. 805-815.

62. K. C. Liu, "High Temperature Fatigue Behavior of Unirradiated V-15 Cr-5 Ti Tested in Vacuum," Journal of Nuclear Materials 103 and 104, 1981, pp. 913-918.

63. E. A. Little and D. A. Stow, "Void-Swelling in Irons and Ferritic Steels," Journal of Nuclear Materials 87, 1979, pp. 25-39.

64. J. M. Rawls et al., Assessment of Martensitic Steels as Structural Materials in Magnetic Fusion Devices, GA-A15749, VC-20d, 1980.

65. M. M. Paxton et al., "Comparison of the In-Reactor Creep of Selected Ferritic, Solid Solution Strengthened, and Precipitation Hardened Commercial Alloys," Journal of Nuclear Materials 80, 1979, pp. 144-151.

66. C. E. Birchenall, "Physical Metallurgy," New York: McGraw-Hill Book Company, Inc., 1959.

67. T. Namba et al., "Hydrogen Permeation Through Vanadium and the Effect of Surface Impurity Layer on It," Journal of Nuclear Materials 105, 1982, pp. 318-325.

68. R. A. Langley et al., "The ISX-A Graphite Limiter Experiment," Journal of Nuclear Materials 85 and 86, 1979, pp. 215-219.

69. R. E. Nightingale, Nuclear Graphite, New York and London: Academic Press, 1962 (QCD 1620 N687).

70. G. B. Engle and L. A. Beavan, Properties of Unirradiated Graphites PGX, HLM, and 2020 for Support and Permanent Side Reflector LHTGR Components, GA-A14646, UC-77, June 1978.

71. Symposium at Bournemouth, Nuclear Graphite, Symposium at Bournemouth, England, November 1959.

72. H. Matsuo, "The Effect of Porosity on the Thermal Conductivity of Nuclear Graphite," Journal of Nuclear Materials 89, 1980, pp. 9-12.

73. W. D. Kingery et al., "Thermal Conductivity: X, Data for Several Pure Oxide Materials Corrected to Zero Porosity," Journal of the American Ceramic Society 37, 1954, pp. 107-110.

74. J. Francl and W. D. Kingery, "Thermal Conductivity: IX, Experimental Investigation of Effect of Porosity on Thermal Conductivity," Journal of the American Ceramic Society 37, 1954, pp. 99-107.

75. S. D. Fulkerson, Apparatus for Determining Linear Thermal Expansions of Materials in Vacuum or Controlled Atmosphere, ORNL-2856, January 1960.

76. R. J. Price and L. A. Beavan, Strength of Nonuniformly Oxidized PGX Graphite, GA-A16270 UC 77, May 1981.

77. W. J. Gray and W. C. Morgan, "Damage Function for Carbon at Neutron Energies up to 15 MeV," Journal of Nuclear Materials 85 and 86, 1979, pp. 237-240.

78. J. C. Bokros, G. L. Guthrie, R. W. Dunlap, and A. S. Schwartz, "Radiation-Induced Dimensional Changes and Creep in Carbonaceous Materials," Journal of Nuclear Materials 31, 1969, pp. 25-47.

79. P. A. Tempest and M. V. Speight, "A Model to Describe the Irradiation-Induced Dimensional Changes in Polycrystalline Graphites and Carbons," Journal of Nuclear Materials 97, 1981, pp. 225-230.

80. P. A. Tempest, "Preferred Orientation and Its Effect on Bulk Physical Properties of Hexagonal Polycrystalline Materials," Journal of Nuclear Materials 92, 1980, pp. 191-200.

81. R. D. Watson and W. G. Wolfer, "Mechanical Constitutive Laws for the Irradiation Behavior of Graphite," Journal of Nuclear Materials 85 and 86, 1979, pp. 159-164.

82. M. Shimotomai et al., "Irradiation Behavior of Graphite Probed by Positrons," Journal of Nuclear Materials 103 and 104, 1981, pp. 779-782.

83. M. Saeki, "Release Behavior of Tritium from Graphite Heavily Irradiated by Neutrons," *Journal of Nuclear Materials 99*, 1981, pp. 100-106.

84. M. C. Underwood, S. K. Erents, and E. S. Hotston, "Experimental Measurements of Hydrogen Exchange in Carbon Surfaces Under Ion Bombardment," *Journal of Nuclear Materials 93 and 94*, 1980, pp. 575-580.

85. P. Hucks, K. Flaskamp, and E. Vietzke, "The Trapping of Thermal Atomic Hydrogen on Pyrolytic Graphic," *Journal of Nuclear Materials 93 and 94*, 1980, pp. 558-563.

86. M. Saidoh, R. Yamada, and K. Nakamura, "Surface Erosion and Re-Emission Behavior of Various Types of Carbon Under Helium-Ion Bombardment," *Journal of Nuclear Materials 102*, 1981, pp. 97-108.

87. S. K. Das, M. Kaminsky, and R. Tishler, "Surface Damage and Sputtering of ATJ Graphite as Candidate Armor Plate Material for TFTR Under D^+ Bombardment," *Journal of Nuclear Materials 85 and 86*, 1979, pp. 225-230.

88. J. Roth et al., "Physical and Chemical Sputtering of Graphite and SiC by Hydrogen and Helium in the Energy Range of 600 to 7500 eV," *Journal of Nuclear Materials 63*, 1976, pp. 222-229.

89. A. Goldsmith et al., *Handbook of Thermophysical Properties of Solid Materials*, New York: The Maxmillan Company, TA 407 A73, 1961.

90. C. T. Lynch, *Handbook of Materials Science Volume II: Metals, Composites, and Refractory Materials*, Cleveland, Ohio, CRC Press, Inc., TA 403.4 L94 V2, 1975.

91. J. L. Weeks and R. L. Seifert, "Apparatus for the Measurement of the Thermal Conductivity of Solids," *The Review of Scientific Instruments 24*, 1953, pp. 1054-1057.

92. R. J. Price, "Thermal Conductivity of Neutron-Irradiated Pyrolytic β-Silicon Carbide," *Journal of Nuclear Materials 46*, 1973, pp. 268-272.

93. T. Vasilos and W. D. Kingery, "Thermal Conductivity: XI, Conductivity of Some Refractory Carbides and Nitrides," *Journal of the American Ceramic Society 37*, 1954, pp. 409-414.

94. C. W. Lee, F. J. Pineau, and J. C. Corelli, "Thermal Properties of Neutron-Irradiated SiC; Effects of Boron Doping," *Journal of Nuclear Materials 108 and 109*, 1982, pp. 678-684.

95. O. J. Whittemore, Jr. and N. N. Ault, "Thermal Expansion of Various Ceramic Materials to 1500°C," *Journal of Nuclear Materials 39*, 1956, pp. 443-444.

96. R. J. Price, "Effects of Fast-Neutron Irradiation on Pyrolytic Silicon Carbide," *Journal of Nuclear Materials 33*, 1969, pp. 17-22.

97. General Atomic Company, *Low Activation Materials Safety Studies Annual Report for Fiscal Year 1981, October 1, 1980-September 30, 1981, GA-A16425 UC-20de, September 1981.*

98. R. J. Price, "Neutron Irradiation-Induced Voids in β-Silicon Carbide," *Journal of Nuclear Materials 48*, pp. 47-57.

19. F. W. Clinard, Jr., "Ceramics of Applications in Fusion Systems," *Journal of Nuclear Materials 85 and 86*, 1979, pp. 393-404.

100. V. E. J. Chiochetti and E. C. Henry, "Electrical Conductivity of Some Commercial Refractories in the Temperature Range 600 to 1500°C," *Journal of the American Ceramic Society 36*, 1953, pp. 180-184.

101. K. Verghese et al., "Hydrogen Permeation Through Nonmetalic Solids," *Journal of Nuclear Materials 85 and 86*, 1979, pp. 1161-1164.

102. M. Mohri et al., "AES-SIMS (IMA) Study of Physical and Chemical Sputtering Processes of Low-Z Materials by Energetic Ions," *Journal of Nuclear Materials 85 and 86*, 1979, pp. 1185-1189.

103. M. B. Kasen et al., "Mechanical, Electrical and Thermal Characterization of G-10 CR and G-11 Cr Glass Cloth/Epoxy Laminates Between Room Temperature and 4 K," *Advances in Cryogenic Engineering, Vol. 26*, New York: A. F. Clark and R. P. Reed, Eds., Plenum Press, 1980, pp. 235-244.

104. F. R. Fickett, R. P. Reed, and E. N. C. Dalder, "Structures, Insulators and Conductors for Large Superconducting Magnets," *Journal of Nuclear Materials 85 and 86*, 1979, pp. 353-360.

105. J. G. Hurst, "Thermal Conductivity of G-10 CR and G-11 Cr Industrial Laminates and Their Component Parts at Low Temperatures," *Materials Studies for Magnetic Fusion Energy Applications at Low Temperatures--V, NBSIR 82-1667, May 1982, pp. 411-427.*

106. R. E. Schramm and M. B. Kasen, "Effect of Cryogenic Temperatures on the Mechanical Performance of Glass-Fabric-Reinforced Laminates," *Materials Studies for Magnetic Fusion Energy Applications at Low Temperatures--V*, NBSIR 82-1667, May 1982, pp. 391-406.

107. H. M. Ledbetter, "Elastic Constants and Internal Friction of Fiber-Reinforced Composites," *Materials Studies for Magnetic Fusion Energy Applications at Low Temperatures--V*, NBSIR 82-1667, May 1982. pp. 441-448.

108. R. H. Kernohan, C. J. Long, and R. R. Coltman, Jr., "Cryogenic Radiation Effects on Electric Insulators," *Journal of Nuclear Materials 85 and 86*, 1979, pp. 379-383.

109. E. A. Erez and H. Becker, "Radiation Damage in Thin Sheet Fiberglass Insulators," *Meeting on Electrical Insulators Fusion Magnets, Germantown, Maryland, December 2-3, 1980*, CONF-801237 UC-20C.

110. M. I. Baskes, *Diffuse: A Code to Calculate One-Dimensional Diffusion and Trapping*, SAND 80-8201, January 1980.

111. D. F. Holland and B. J. Merril, "Analysis of Tritium Migration and Deposition in Fusion Reactor Systems," *Proceedings of the 9th Symposium on Engineering Problems of Fusion Research, Chicago, Illinois, October 26-29, 1981*, IEEE Pub. No. 81CH1715-2, pp. 1209-1212.

APPENDIX A

EXAMPLE MATERIAL PROPERTY COMPUTER SUBCODE. HYDROGEN ISOTOPES DIFFUSION COEFFICIENTS IN 316 STAINLESS STEEL (SDIF)

APPENDIX A

EXAMPLE MATERIAL PROPERTY COMPUTER SUBCODE.

HYDROGEN ISOTOPES DIFFUSION COEFFICIENTS IN 316 STAINLESS STEEL (SDIF)

The rate of diffusion of hydrogen isotopes in 316 stainless steel is important to tritium inventory calculations for fusion reactors. The SDIF subroutine calculates the diffusion coefficients for the concentration-driven migration of hydrogen, deuterium and tritium in the usual transport equation (Fick's law)

$$\vec{J} = D\ \vec{\nabla}C \tag{A-1}$$

where

$\vec{J}$ = hydrogen isotope flux (isotope atoms/m^2 s)

D = diffusion coefficient (m^2/s)

$\vec{\nabla}C$ = gradient of the hydrogen isotope concentration (isotope atoms/m^4).

A.1 Summary

Calculation of the diffusion coefficients for hydrogen isotopes requires only the steel temperature as input information. The expression used to calculate coefficient values is

$$D = \frac{1}{\sqrt{m}}\ 9.8 \times 10^{-6}\ \exp(-7073/T) \tag{A-2}$$

where

m = isotopic mass number (atomic units)

T = 316 stainless steel temperature (K).

The equation is based on experimental measurements of concentration gradients in the metal as well as permeation rate measurements. The effect of irradiation is not modeled because no data for irradiated stainless steel have been found.

Equation (A-2) can be expected to have a standard error of +4.5 and -0.8 of the calculated value for hydrogen, +1.0 and -0.5 of the calculated value for deuterium, and +5.4 and -0.84 of the calculated value for tritium. The expression is valid in the temperature range 375 to 1000 K and is known not to be valid below 300 K because of grain boundary diffusion.

A.2 Literature and Data

Investigators generally agree that an exponential dependence on temperature is the appropriate expression for the diffusion coefficient of hydrogen isotopes in stainless steels.[A-1-A-9] In addition, the rather limited data are consistent with the classical reciprocal square root dependence of the diffusion coefficient on the diffusing isotope's mass.[A-5,A-9]

There are, however, several complicating features. In most metals hydrogen diffuses in the atomic state.[A-10] In order to move across a metal barrier from one outside gas volume to another, the molecular hydrogen in the gas must dissociate at one surface and recombine on the other surface. Thus measurement techniques which rely on measuring membrane permeation rates[A-2,A-5,A-7] must be careful to properly consider the possibility of delays due to time required for dissociation and recombination at the metal barrier's surfaces. Care must also be taken that surface layers such as metallic oxides which may form during the measurements do not cause a significant time-varying reduction in the rate of surface dissociation and recombination.[A-11]

A second complication is the existence of a rapid diffusion path which is available to a small fraction of the diffusing hydrogen isotopes. Most authors believe this rapid path is grain boundary diffusion[A-1,A-3,A-8,A-9] and it is probably only important at temperatures below 375 K.[A-9] At least one author[A-1] has derived an expression for an effective diffusivity which includes the grain boundary diffusion but does not specifically consider the parallel paths. If such detail is necessary, a parallel-path approach using the grain boundary diffusivity of Reference A-3 and the estimated grain boundary fractional area of $\sim 4 \times 10^{-5}$ from Reference A-1 is recommended. In the SDIF subroutine the grain boundary contribution will be neglected and the range of application will thus be limited to greater than 300 K.

Variations from one type of stainless steel to another are not a fundamental problem, but could cause a practical problem in finding sufficient data to use if the variations were large. The data to be reviewed in this subsection and Reference A-9 indicate that there are no substantial differences in austenitic stainless steels but that phase transitions can cause a substantial change in the diffusion rate.[A-9] Thus the usable data are limited to austenitic stainless steels but not to 316 stainless steel.

A serious problem is presented by the fact that no data for irradiated stainless steel have been found. Experiments now planned should resolve this problem in the near future.

The two sources of information for hydrogen diffusion in austenitic steels are Maroni and Van Deventer[A-4] and Randall and Salmon.[A-5] Both sources employ permeation measurements but only Randall and Salmon actually publish a diffusion coefficient expression,

$$D = 2.551 \times 10^{-6} \exp(-7460/T) \quad . \qquad \text{(A-3)}$$

The expression is based on data at 842 and 971 K in 347 stainless steel.

Maroni and Van Deventer[A-4] has figures showing hydrogen permeability and hydrogen solubility for 300 series stainless steels and iron, respectively. They also state that the permeability can be determined as the direct product of the hydrogen concentration gradient and the bulk diffusion coefficient. From Figure 3 of Reference A-4, the permeability can be found to be

$$\phi = 2.17 \times 10^{-7} \exp(-7823/T) \frac{\Delta(\sqrt{p})}{X} \qquad \text{(A-4)}$$

where

ϕ = flux of hydrogen through a 31ˢ stainless steel plate (m^3 of hydrogen at STP/$m^2 s$)

X = plate thickness (m)

$\Delta(\sqrt{p})$ = difference of the square root at pressure across the plate ($\sqrt{10^3 \text{ Pa}}$).

From Figure 1 of Reference A-4, the solubility can be found to be

$$S = 6.3 \exp\left(\frac{-3155}{T}\right) \sqrt{P} \qquad \text{(A-5)}$$

where

S = amount of hydrogen dissolved (atomic parts per million)

P = pressure (Pa).

If the permeability can be determined as the product of the hydrogen concentration gradient and the bulk diffusion coefficient (i.e., if the time required for surface dissociation at the high pressure surface and for surface recombination at the low pressure face is negligible) one can write

$$d' = -D \frac{dc}{dX} = \frac{-D\left(S'_{\text{one face}} - S'_{\text{other face}}\right)}{X} \quad \text{(A-6)}$$

where

ϕ' = flux of hydrogen through a 316 stainless steel plate (kg of hydrogen/m^2s)

S' = amount of hydrogen dissolved (kg of hydrogen/m^3 steel).

Combining Equations (A-4) to (A-6) with suitable units conversions[a] leads to an expression for the diffusion coefficient of hydrogen in 300 series stainless steels,

$$D = 6.8 \times 10^{-7} \exp(-4668/T) \quad . \quad \text{(A-7)}$$

The equation is somewhat suspect because of the assumption that surface dissociation and recombination rates are negligibly small, but may be satisfactory for the 673 to 973 K temperature range that these authors consider.

Two references for deuterium diffusion in austenitic stainless steels have been found. Wilson and Baskes[A-6] found

$$D = 1.2 \times 10^{-5} \exp(-7096/T) \quad \text{(A-8)}$$

for deuterium in 316 stainless steel. The expression was obtained from experimental data promised in a later publication but not found by this

---

[a] The following units conversions were employed: 1 m^3 of hydrogen at STP = 8.88×10^{-2} kg hydrogen; 1 atomic ppm in 316 stainless steel = 1.43×10^{-4} kg hydrogen/m^3 steel.

author. No temperature range was published for Equation (A-8) so it is assumed that the expression is valid only over the range of temperatures which are discussed in Reference A-6, 300 to 440 K.

Deuterium diffusion data from Braun, Emmoth, Waelbroeck and Wienhold[A-7] are by far the most useful information on the topic of hydrogen isotope diffusion that have been published because individual data are presented. These data which were obtained from Figure 3 of Reference A-7 are reproduced as Table A-1. The data were obtained by using the permeation measurement technique on a 304 stainless steel membrane. Temperatures from 360 to 865 K were employed.

From their data Braun et al. deduced an expression for the diffusion coefficient of deuterium in austentitic stainless steels,

$$D = 1.8 \times 10^{-5} \exp(-7450/T) \quad . \qquad (A-9)$$

Tritium diffusion data are available from Austin and Elleman,[A-8] Louthan et al.[A-9] and Randall and Salmon.[A-5] Austin and Elleman found

$$D = 1.8 \times 10^{-6} \exp(-7079/T) \qquad (A-10)$$

for tritium in 304- and 316-stainless steel over the temperature range 298 to 495 K. Concentration profiles rather than permeation rates were employed to determine Equation (A-10). Louthan et al. also used concentration profiles to find

$$D = 2.71 \times 10^{-7} \exp(-6490/T) \qquad (A-11)$$

for temperatures above 373 K in 304 L stainless steel. No upper bound was published for Equation (A-11) so it was assumed to be valid only over the range in which it was used, 373 to 475 K. Randall and Salmon found

TABLE A-1. DEUTERIUM DIFFUSION COEFFICIENTS MEASURED IN 304 STAINLESS STEEL BY BRAUN ET AL.[A-7]

Temperature (K)	Diffusion Coefficient (m^2/s)
360	6.89×10^{-14}
383	1.69×10^{-13}
419	2.26×10^{-13}
444	2.85×10^{-12}
494	4.74×10^{-12}
546	2.82×10^{-11}
554	4.34×10^{-11}
563	3.29×10^{-11}
571	4.00×10^{-11}
573	7.22×10^{-11}
592	5.18×10^{-11}
592	6.30×10^{-11}
632	2.53×10^{-10}
652	2.46×10^{-10}
655	1.86×10^{-10}
663	2.15×10^{-10}
666	2.67×10^{-10}
701	7.80×10^{-10}
717	7.89×10^{-10}
737	8.78×10^{-10}
762	8.73×10^{-10}
787	1.13×10^{-9}
865	2.78×10^{-9}

$$D = 1.293 \times 10^{-6} \exp(-7081/T) \quad \text{(A-12)}$$

from their membrane permeation rate measurements at 842 and 971 K with 347 stainless steel.

The published information on hydrogen isotope diffusion in stainless steels is remarkable for the limited amount of data that are published to support the many differing equations that are presented. There is little significant difference between the austenitic stainless steels but a large difference between these steels and iron. When the differing equations are compared (as they are in the next subsection) it becomes apparent that there is nearly an order-of-magnitude difference between the various equations. The most logical explanation of these differences is unconsidered surface effects in the high temperature permeation measurements and grain boundary diffusion enhancement in the low temperature measurements. At the present time, no data for the effect of irradiation on diffusion have been found.

A.3 Model Development

Since the literature and data reviewed in the last section show that hydrogen isotope diffusion coefficients in austenitic stainless steels are proportional to the reciprocal square root of the diffusing element's atomic mass, all of the data can be normalized to hydrogen diffusion rates and considered together. The six usable sources discussed in Subsection A.2 have thus been represented together in Figure A-1. In addition the iron data of Waelbroeck et al.,[A-2] the grain boundary diffusion data of Calder et al.[A-3] and calculations with Equation (A-2) are shown. The iron data and grain boundary diffusion data clearly belong to a different population than the remaining data.

The data shown in Figure A-1 define a linear band of diffusion coefficients which is about an order of magnitude wide with no change in

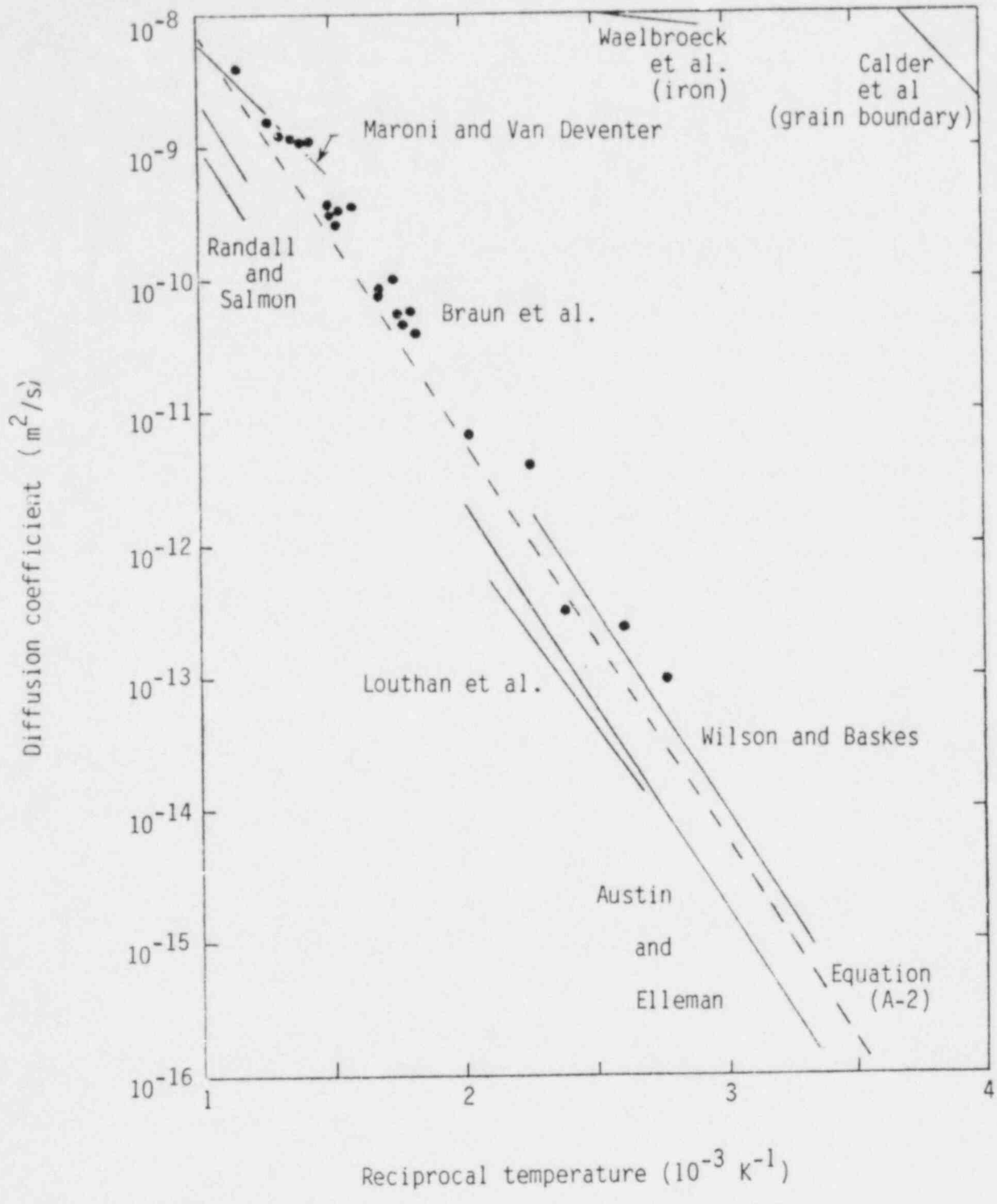

Figure A-1. Hydrogen isotope diffusion coefficient data normalized to one atomic weight unit.

slope in the range of reciprocal temperatures for which the data are valid (temperatures from 1000 to 300 K). A least squares natural log fit to a single equation of the form

$$D = A \exp(-B/T) \tag{A-13}$$

where A and B are constants was therefore employed to describe the information in Figure A-1. Each line was represented by its two end points and another point at the average of the end point temperatures. The resultant expression is Equation (A-2) and is represented by the dashed line in Figure A-1.

Several attempts were required to describe the scatter of the data in Figure A-1. For the traditional standard error approach, some transformation which produces a temperature-independent scatter is necessary. Use of the diffusion coefficient in the defining expression

$$S = \frac{\sum_{i=1}^{n} [Y(T) - Y_i]^2}{n - \text{degrees of freedom}} \tag{A-14}$$

where

S = standard error of correlation with respect to its data base

$Y(T)$ = calculated quantity

Y_i = measured quantity

n = number of data used to test the model

would give far too much weight to the high temperature data where the absolute differences are large but the fractional differences are small.

Defining Y to be the ratio of the measured diffusion coefficient to the predicted one produced standard errors greater than one, thus implying possible negative diffusion coefficients.

The approach that was finally adopted defined Y(T) as the natural log of the predicted diffusion coefficient and Y_i to be the natural log of the measured diffusion coefficient. The asymmetric uncertainties thus obtained for the diffusion coefficients reflect the symmetric scatter of the data about the center of the band shown in Figure A-1 as well as the least-squares-log technique used to determine the constants in Equation (A-13).

A.4 SDIF Subroutine Listing and Plots

Table A-2 is a listing of the SDIF subroutine and Figure A-2 is a subroutine-generated plot of diffusion coefficients calculated for hydrogen (top line), deuterium (middle line), and tritium (bottom line) in 316 stainless steel as a function of reciprocal temperature.

TABLE A-2. LISTING OF THE SDIF SUBROUTINE

```
          SUBROUTINE SDIF(TEMP,HDIF,DDIF,TDIF)
C
C         HDIF   = OUTPUT DIFFUSION COEFFICIENT FOR HYDROGEN IN
C                       316 STAINLESS STEEL (M**2/S)
C         DDIF   = OUTPUT DIFFUSION COEFFICIENT FOR DEUTERIUM IN
C                       316 STAINLESS STEEL (M**2/S)
C         TDIF   = OUTPUT DIFFUSION COEFFICIENT FOR TRITIUM IN
C                       316 STAINLESS STEEL (M**2/S)
C
C         TEMP   = INPUT 316 STAINLESS STEEL TEMPERATURE (K)
C
C         SDIF WAS CODED BY D. L. HAGRMAN OCTOBER 1982
C
          HDIF = 9.8E-06 * EXP(-7073./TEMP)
          DDIF = 0.7071067 * HDIF
          TDIF = 0.5773502 * HDIF
C
          RETURN
          END
```

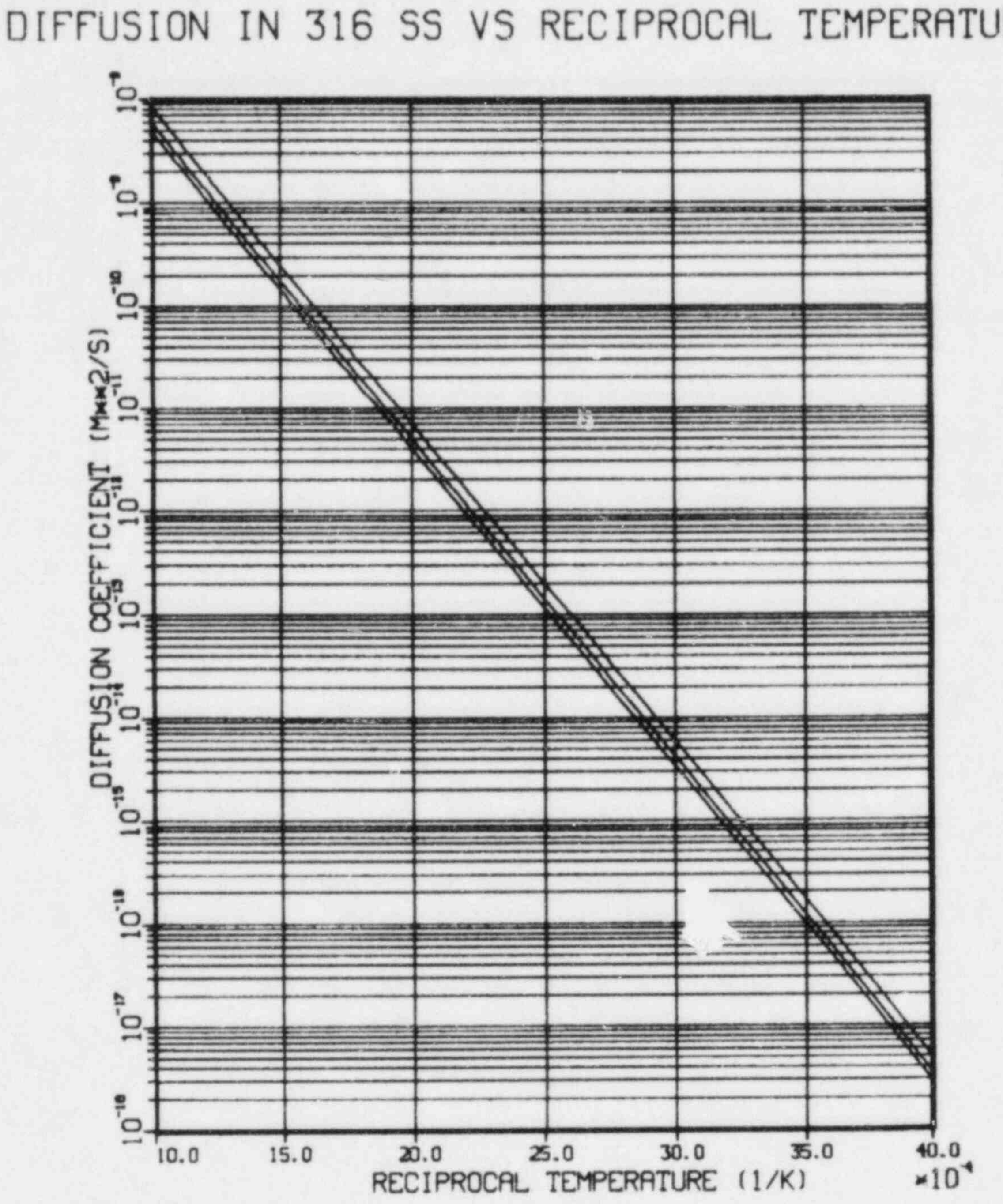

Figure A-2. Values of the hydrogen (top line), deuterium (middle line), and tritium (bottom line) diffusion coefficients in 316 stainless steel calculated by the SDIF subroutine as a function of reciprocal temperature.

A.5 References

A-1. H. J. Garber, *Studies of the Permeation and Diffusion of Tritium and Hydrogen in TFTR*, WFPS-TME-012, 1975.

A-2. F. Waelbroeck et al., "Hydrogen Solubilization Into and Permeation Through Wall Materials," *Journal of Nuclear Materials 85 and 86*, 1979, pp. 345-349.

A-3. R. D. Calder, T. S. Elleman, and K. Verghese, "Grain Boundary Diffusion of Tritium in 304- and 316-Stainless Steels," *Journal of Nuclear Materials 46*, 1973, pp. 46-52.

A-4. V. A. Maroni and E. H. Van Deventer, "Materials Consideration in Tritium Handling Systems," *Journal of Nuclear Materials 85 and 86*, 1979, pp. 257-269.

A-5. D. Randall and O. N. Salmon, *Diffusion Studies 1. The Permeability of Type 347 Stainless Steel to Hydrogen and Tritium*, KAPL-904, 1953.

A-6. K. Wilson and M. I. Baskes, "Deuterium Trapping in Irradiated 316 Stainless Steel," *Journal of Nuclear Materials 76 and 77*, 1978, pp. 291-297.

A-7. M. Braun et al., "Determination of Deuterium Surface Recombination Rates on Stainless Steel," *Journal of Nuclear Materials 93 and 94*, 1980, p. 861-865.

A-8. J. H. Austin and T. S. Elleman, "Tritium Diffusion in 304- and 316-Stainless Steels in the Temperature Range 25 to 222°C," *Journal of Nuclear Materials 43*, 1972, pp. 119-125.

A-9. M. R. Louthan, Jr., J. A. Donovan, and G. R. Caskey, Jr., "Tritium Absorption in Type 304 L Stainless Steel," *Nuclear Technology 26*, 1975, pp. 192-200.

A-10. D. F. Holland and B. J. Merril, "Analysis of Tritium Migration and Deposition in Fusion Reactor Systems," proceedings of *The 9th Sumposium on Engineering Problems of Fusion Research, Chicago, Illinois, October 26-29, 1981*, IEEE Pub. No. 81CH1715-2, pp. 1209-1212.

A-11. W. A. Swansiger and R. Bastasz, "Tritium and Deuterium Permeation in Stainless Steels: Influence of Thin Oxide Films," *Journal of Nuclear Materials 85 and 86*, 1979, pp. 335-339.